GPR Imaging of Prehistoric Animal Bone-beds

by

Blair Benson Schneider
B.S., James Madison University, 2009
M.S., The University of Kansas, 2012

Submitted to the Department of Geology
and the Faculty of the Graduate School of The University of Kansas
in partial fulfillment of the requirements for the degree of
Doctor of Philosophy
2017

Advisory Committee:

_____
Don W. Steeples, Co-Chair

_____
Rolfe D. Mandel, Co-Chair

_____
Georgios P. Tsoflias

_____
Leigh A. Stearns

_____
Jack L. Hofman

Date Defended: July 13, 2017

The Dissertation Committee for Blair Schneider certifies that this is the approved version of the following dissertation:

GPR Imaging of Prehistoric Animal Bone-beds

Advisory Committee:

_____
Don W. Steeples, Co-chair

_____
Rolfe D. Mandel, Co-chair

Date Approved: July 25, 2017

Abstract

This research investigates the detection capabilities of Ground-penetrating radar for imaging prehistoric animal bone-beds. The first step of this investigation was to determine the dielectric properties of modern animal bone as a proxy for applying non-invasive ground-penetrating radar (GPR) for detecting prehistoric animal remains. Over 90 thin section samples were cut from four different modern faunal skeleton remains: bison, cow, deer, and elk. One sample of prehistoric mammoth core was also analyzed. Sample dielectric properties (relative permittivity, loss factor, and loss-tangent values) were measured with an impedance analyzer over frequencies ranging from 10 MHz to 1 GHz. The results reveal statistically significant dielectric-property differences among different animal fauna, as well as variation as a function of frequency. The measured sample permittivity values were then compared to modeled sample permittivity values using common dielectric-mixing models. The dielectric mixing models were used to report out new reported values of dry bone mineral of 3-5 in the frequency range of 10 MHz to 1 GHz.

The second half of this research collected controlled GPR experiments over a sandbox containing buried bison bone elements to evaluate GPR detection capabilities of buried animal bone. The results of the controlled GPR sandbox tests were then compared to numerical models in order to predict the ability of GPR to detect buried animal bone given a variety of different depositional factors, the size and orientation of the bone target and the degree of bone weathering. The radar profiles show that GPR is an effective method for imaging the horizontal and vertical extent of buried animal bone. However, increased bone weathering and increased bone dip were both found to affect GPR reflection signal strength. Finally, the controlled

sandbox experiments were also utilized to investigate the impact of survey design for imaging buried animal bone. In particular, the effects of GPR antenna orientation relative to the survey line (broad-side mode versus end-fire mode) and polarization effects of the buried bone targets were investigated. The results reveal that animal bone does exhibit polarization effects. However, the polarization results are greatly affected by the irregular shape and size of the bone, which ultimately limits the potential usefulness of trying to utilize polarization data to determine the orientation of buried bone targets. In regard to antenna orientation, end-fire mode was found to have little difference in amplitude response as compared to the more commonly used broad-side mode and in fact sometimes outperformed the broad-side mode. Future GPR investigations should consider utilizing multiple antenna orientations during data collection.

Acknowledgements

There are countless individuals whose support and mentorship have helped me achieve the completion of this dissertation work. I am forever grateful to my husband, Nick Schneider, for being there 100% to help me accomplish this goal, including using his own vacation time to go collect field data with me! Thank you to my beautiful daughter Rachael, who motivates me to be the best scientists and role model that I can be. Thank you to my family and friends for their constant support and help. Especially those of you who have listened to me whine, helped me in the field or sweltered in the shop to dig sand with me for countless experiments – Jeff Ross, Brandon Graham, Anthony Hoch, Leila Joyce-Seals, Anna Wieser, Mackenzie Cremeans, Sarah Morton, Amanda Livers, Bevin Clay, Amanda Schneider, Jose Velez, Yao Wang, Alex Nolte, Tyrell Tenpenny. Your generosity will never be forgotten!

A very special thank you to my mentors, Don Steeples and Rolfe Mandel. You both have taught me so much and supported my many endeavors (focus, focus, focus!) throughout this journey and I am forever grateful. Thank you to George Tsoflias, who has been an incredible source of advice and wisdom. You have fostered my passion for geophysics and GPR since I first moved here to Kansas in 2009. Thank you to Jack Hofman for his passion and enthusiasm for this research, which includes sitting on the floor digging through boxes of bone samples over and over again. And thank you to Leigh Stearns, whose mentorship and feedback has helped shape the scientist I am today.

Finally, I wish to acknowledge the many sources of specimens and funding that made this dissertation possible. First and foremost, the professional development program and financial support from the Madison and Lila Self Graduate Fellowship. This program helped shape me

into a leader and I am so incredibly grateful to have had the opportunity to work with such amazing colleagues. In addition, the development program and financial support from the NSF GK-12 fellowship and Dr. Steve Case. This program spurred my passion for science education and the importance of communicating our science to the public, and has ultimately defined the career path I will choose after this. I also thank the University of Kansas Department of Geology, the University of Kansas Doctoral Research Fund, the ODYSSEY Archaeological Research Program, and the Society of Exploration Geophysicists for their financial support of this research. All of these sponsors contributed to the success of this project. Finally, thank you to the individuals who helped contribute specimens for this research: Dr. Mary Adair, Brad Birkelo, and Dr. Robert Feranec.

Table of Contents

List of Figures

List of Tables

CHAPTER 1

Ground-Penetrating Radar for Archaeological Research

1.0 Introduction

Geophysical surveying, and in particular ground-penetrating radar (GPR), has emerged as a tool for archaeological investigations. GPR is capable of non-invasive high-resolution subsurface imaging, fast data collection and can be used to build 3D grids of the very shallow subsurface (<1 m) (Pipan et al., 2012; Wen-ke et al., 2012; Nuzzo et al., 2002). GPR has been used in archaeological research to detect a variety of artifacts and features, including but not limited to graves, remains of structures, and earthworks (Schneider et al., 2016; Bigman, 2014; Urban et al., 2014; Goodman and Piro, 2013; Goodman et al., 2009; Sternberg and McGill, 1995). However, the archeological aspects of bone have not been investigated thoroughly with GPR. This is potentially an important archaeological feature for study, as bone is often found at sites across the world, often times comprising prominent cultural features or even dense bone-beds (Hell Gap, Frison, 1974; Davis, 1978; Hudson-Meng, Agenbroad, 1978; Horner site, Frison & Todd, 1987; Cyprus, Simmons, 1988; Lipscomb, Todd et al., 1992; Cooper Model, Bement, 2003; Winger, Mandel & Hofman, 2003; Campitello Quarry, Mazza et al., 2006; Kostenki, Hoffecker et al., 2010; Beacon Island, Mandel et al., 2014). Bone-beds can provide a wealth of information at archeological sites, including site formation processes, seasonality of the kill, and size of the herd. In addition, researchers have used animal bone at archaeological sites to make interpretations of the paleo-environment (Leyden et al., 2006), provide insights into socio and economic histories of identified sites (Uerpmann, 1973), and provide ages for sites using radiocarbon dating (Hoard et al., 2004; Aitken, 1990).

1.1 History of GPR for Bone Detection

There are reasons why bone has not been fully investigated with GPR methods used in archeology. A thorough examination of the dielectric properties of bone in the frequency ranges commonly used in archaeo-geophysics (100 MHz - 1000 MHz) is lacking from the geophysical literature. Information about how bone permittivity changes with signal frequency, species type, bone water saturation, and decomposition over time, is necessary to model and interpret GPR data.

Regulations also play a key role. Archaeological excavation techniques are seen as destructive to sacred cultural patrimony at Native American burial mounds and ceremonial centers (Whittaker and Storey, 2008). Federal legislation, such as the Archaeological Resources Protection Act of 1979, protect archeological resources on federal lands and Indian lands and require permits for excavation of archeological sites. The 1990 Native American Graves Repatriation Act gives Native American burial sites greater protection and requires that Indian tribes and Native Hawaiian organizations be consulted prior to archaeological investigations, or when cultural items are unexpectedly uncovered. While these laws highlight the increased need for non-destructive techniques to aid in archaeological investigations, geophysical surveys that are conducted in hopes of identifying burial sites containing human remains commonly cannot be compared to intrusive methods to evaluate the effectiveness of geophysical imaging (Bigman, 2012; Doolittle and Bellantoni, 2010; Nobes, 1999).

A common misconception is that bone cannot be detected because of insufficient contrast or the size of the bone is too small (Damiata et al, 2013). However, researchers have had recent success at detecting prehistoric mammoth with GPR in northern latitudes such as Alaska where

the remains are encased in ice (Urban et al, 2016) and in permafrost in Siberia (Makino and Miura, 2004; Grandjean et al., 2002). An argument to insufficient contrast in other environments cannot be made unless the electrical properties of animal bone are known. Prehistoric animal kill sites are sometimes found in soils or sediments that have high concentrations of fine-grained silts or clays such as the Winger site in western Kansas (Mandel and Hofman, 2003). These fine-grained sediments have increased conductivity, which will attenuate the GPR signal more rapidly.

Bone size is another common misconception, as stated above. Singular bones, depending on the size of the animal, are often assumed to be too small for GPR resolution depending on the frequency and corresponding wavelength being used. However, prehistoric archaeological sites often contain remains of large mammals such as mammoths and bison, whose bones can be 0.5 m to 4 m long. In addition, dense bone beds have been recorded at many archaeological sites in the U.S., including Hell Gap (Frison, 1974), Rex Rodgers (Speer, 1978), Hudson-Meng (Agenbroad, 1978), Horner (Frison and Todd, 1987), Lipscomb (Todd et al., 1992), Cooper (Bement, 1999), and Winger (Mandel and Hofman, 2003). These bone-beds are often the remnants of a large animal kill, for example driving a herd of buffalo off of a gully or cliff into an embankment. They vary in size and density depending on the type of kill. For example, the Winger site (Mandel and Hofman, 2003) contains a dense 35 m long bison bone-bed that is approximately 25 cm thick and contained within a silty clay loam pond deposit in western Kansas. The Rex Rodgers site in Texas contains the remains of six or more bison (Speer, 1978). The remains were spread over 3 m^2 grid within an ancient gully. The Cooper site, located in Oklahoma, revealed the remains of three separate bison kills in an ancient arroyo (Bement, 1999). The dense bone-bed covers a 24 m^2 area with 29 total bison contained in sandy alluvium.

GPR detection has a much higher likelihood of success at detecting bone-beds of this size and density.

There have been several attempts in forensic research to locate human skeletal remains using geophysical equipment, in particular magnetic, electrical resistivity, and electromagnetic methods (Pringle, et. al., 2012; Powell, 2004; Davenport, 2001; France, et al., 1992; Bevan, 1991). The bulk of these studies focused on the use of geophysical tools to detect buried cadavers of homicide victims or the locations of gravesites in cemetaries. The majority of this previous research has been successful at detecting grave locations, but few provided a distinction between the contributions of the bone signature versus burial type and the disturbed soil encasing the gravesite. However, Damiata et al. (2013) reported successful detection of skeletal remains in a grave burial at a 1000 year old Viking age churchyard in Iceland. The grave was contained in Andosols, which are derived from Aeolian sediments of volcanic origin, with intermixed layers of tephra above the grave. The remains were in good condition when ground-truthed after the GPR survey, and the authors' show multiple transects that crossed over the grave. The hyperbolic diffractions over the upper half of the remains are actually from an air pocket that was contained in the chest cavity and discovered during excavation, but there are additional diffractions over the lower half of the remains that appear to be from the long bones.

Schultz and Martin (2011) conducted a survey that compared the GPR response of a grave containing a recently deceased pig and a "blank" grave that had disturbed soil but no cadaver. The graves were in Spodosols in Orlando, Florida. The Spodosols are ideal for GPR application because they consist mostly of coarse sands or loamy sands with low clay content. Schultz and Martin (2011) successfully detected both graves with GPR, and demonstrated that there was a difference in GPR signature between the two graves. They also concluded that there

is still potential for a GPR to locate a grave even after a cadaver decayed over time, because of the disturbed soil signature. However, this potential does not necessarily hold true for an archaeological site. Animal remains at sites rarely are intentionally buried. Instead, natural depositional processes bury them over time, leaving no disturbed soil signature. Also, if disturbed soil occurs in the vicinity of the animal remains at an ancient archaeological site, compaction from overlying sediments or the development of a soil profile often erases the disturbed soil signature. Finally, their research does not account for the change in GPR signature due to the biological tissues present from the pig cadaver. Prehistoric animal remains are not often found with any biological tissue remaining, unless they were preserved in a unique environment such as permafrost or an ancient bog environment (Fisher, et al., 2012; García-Alix et al., 2012).

This prior research has highlighted several success stories of using GPR to locate gravesites, but the signature from the disturbed soil is often the primary target used by investigators to locate the cadavers or graves. However, prehistoric animal remains, unlike humans in graves, typically were not buried soon after death, but instead were slowly mantled by sediment. Furthermore, the soil in the vicinity of the animal remains is not drastically disturbed. Therefore, the bone remains can only be detected if there is enough contrast between them and the sediments they are encased in.

1.2 Overview of Ground-Penetrating Radar

GPR transmits electromagnetic (EM) waves into the subsurface in the frequency ranges of 25 MHz-1000 MHz and records changes in the electrical properties (i.e. the electrical

conductivity and relative permittivity) of the subsurface (Davis and Annan, 1989). The electrical properties control the velocity, attenuation (i.e. absorption) and power of the EM waves that are reflected back to the receiving antenna. Table 1.1 lists the relative permittivity, electrical conductivity, velocity, and attenuation of common geologic materials encountered in archaeological surveys at a central frequency of 100 MHz. Low electrical conductivity environments, such as coarse grained sediments like sands, are favorable for GPR imaging. Increased levels of conductivity results in increased attenuation, or absorption of the electro-magnetic waves as they transmit through materials. Finer-grained sediments such as silts and clays have a wide range of recorded electrical conductivity levels, so the chance of success with GPR varies from site to site depending on these properties.

Lower frequency antennas are capable of imaging tens of meters into the subsurface, but with reduced resolution capabilities. Higher frequency antennas are limited to shallower depths of penetration, but have increased resolution capabilities. Archaeological investigations typically employ higher frequencies (400 MHz-1000 MHz) for exploration because they can resolve smaller features buried in the subsurface and at shallower depths (Annan, 2005). GPR resolution is estimated to be one quarter the signal wavelength and is calculated from the velocity of propagation and the signal frequency, shown in Equation 1.

$$\lambda = \frac{v}{f} \tag{1}$$

λ is the signal wavelength measured in meters, v is the velocity of propagation measured in m/ns, and f is the signal frequency measured in MHz. Table 1.2 lists expected resolution capabilities based on signal frequency and sediment type.

1.3 Overview of the Dissertation

This research focuses on the application of GPR for detecting modern animal bone as a proxy for detecting buried prehistoric animal bone. This thesis is presented in 5 chapters. Chapter 2 presents the dielectric measurements of approximately 90 samples of modern animal bone, including bison, cow, deer, and elk, as well as one sample of prehistoric mammoth bone. In addition, each modern bone sample's porosity, bulk density, water saturation, and volumetric water content was measured. The results reveal that bone is a frequency-dependent, low-loss target for GPR detection. The results also show that there are statistically significant differences in dielectric properties between different animal species.

Chapter 3 continues by using the measurements described in chapter 2 and comparing the measured permittivity values with modeled permittivity values using three well-established GPR models: the Topp model, the Complex Refractive Index Model (CRIM), and the Hanai-Bruggeman model. The CRIM and Hanai-Bruggeman models were utilized to estimate the base permittivity values of bone mineral grains to fall in the range of 3-5 within the frequency ranges of 10 MHz to 1000 MHz. Overall, both the CRIM and Topp model are recommended for estimating relative permittivity values of animal bone because of their overall accuracy across the entire frequency sweep and their simplicity to implement.

Chapter 4 presents successful GPR detection of the vertical and horizontal extents of buried bison bone in controlled sandbox experiments. Additional factors of bone size, depth of burial, weathering state, and dip angle were considered in the experiments and compared to predictions from numerical models. The results show that a priori information of the bone size, depth of burial, and depositional settings are important for determining whether or not GPR will

be able to detect buried bone. Increased weathering of the buried bone reduces the relative permittivity of the bone, which can either improve or worsen GPR detection depending on the depositional settings. Finally, increased dip angle of a bone reduces GPR detection capability.

Finally, Chapter 5 highlights the importance of survey design techniques on GPR detection of buried bison bone. In particular, antenna orientation (broad-side mode versus end-fire mode) and polarization effects of the buried bone targets are considered. The results show that animal bone does exhibit polarization effects, but that they are highly dependent on the size and shape of the bone. The results also indicate that there was little difference in amplitude response between the broad-side and end-fire mode, and that in some instances the end-fire mode outperformed the broad-side mode.

References

Agenbroad, L.D., 1978, The Hudson-Meng Site: An Alberta bison kill in the Nebraska High Plains: University Press of America.

Aitken, M.J., 1990, Science-based dating in archaeology: Routledge, New York.

Bement, L.C., 2003, Constructing the cooper model of Folsom bison kills on the Southern Plains: Great Plains Research, v. 13, p. 27-41.

Bevan, B.W., 1991, The Search for Graves: Geophysics, v. 56, no. 9, p. 1310-1319.

Bigman, D.P., 2014, Mapping social relationships: geophysical survey of a nineteenth-century American slave cemetery: Archaeological and Anthropological Sciences, **6**, 17-30.

Bigman, D.P., 2012, The use of electrogmagnetic induction in locating graves and mapping cemeteries: an example from native North America: Archaeological Prospection, v. 19, p. 31-39.

Damiata, B.N., Steinberg, J.M., Bolender, D.J. and Zoega, G., 2013, Imaging skeletal remains with ground-penetrating radar: comparative results over two graves from Viking Age and Medieval churchyards on the Store-Seyla farm, northern Iceland: Journal of Archaeological Science, **40**, 268-278.

Davis, L.B., 1978, Bison procurement and utilization: A symposium: Plains Anthropologist, **23**, 362 p.

Davenport, G.C., 2001, Remote sensing applications in forensic investigations: Historical Archaeology, v. 35, no. 1, p. 87-100.

Doolittle, J.A. and Bellantoni, N.F., 2010, The search for graves with ground-penetrating radar in Connecticut: Journal of Archaeological Science, v. 37, p. 941-949.

France, D.L., Griffin, T.J., Swanburg, J.G., Lindemann, J.W., Davenport, G.C., Trammell, V., Armbrust, C.T., Kondratieff, B., Nelson, A., Castellano, and K., Hopkins, D., 1992, A multidisciplinary approach to the detection of clandestine graves: Journal of Forensic Sciences, v. 37, no. 6, p. 1445-1458.

Frison, G.C., 1974, The Casper Site: A Hell Gap Bison Kill on the High Plains: Academic Press, New York, New York, 266 p.

Frison, G.C. and Todd, L.C., eds., 1987, The Horner Site: The type site of the Cody Cultural Complex: Academic Press Inc., Orlando, Florida, 586 p.

Goodman, D., Hiromichi, H., Higashi, N., Nishimura, Y., Tokuda, M., and dok Oh, H., 2009, The application of GPR overlay analysis in archaeological prospection: Discovery at the Japanese Imperial Family tombs in Miyazaki Prefecture: Archeosciences, **33 (supp)**, 295-297.

Goodman, D. and Piro, S., 2013, GPR remote sensing in archaeology: Springer-Verlag Berlin Heidelberg.

Hoard, R.J., Banks, W.E., Mandel, R.D., Finnegan, M., Epperson, J.E., 2004, A Middle Archaic Burial from East Central Kansas: American Antiquity, **69**, 717-739.

Hoffecker, J.F., Kuz'mina, I.E., Syromyatnikova, E.V., Anikovich, M.V., Sinitsyn, A.A., Popov,

V.V. and Holliday, V.T., 2010, Evidence for kill-butchery events of early Upper Paleolithic age at Kostenki, Russia: Journal of Archaeological Science, **37**, 1073–1089.

Leyden, J.J., Wassenaar, L.I., Hobson, K.A., Walker, E.G., 2006, Stable hydrogen isotopes of bison bone collagen as a proxy for Holocene climate on the Northern Great Plains: Palaeogeography, Palaeoclimatology, Palaeoecology, **239**, 87-99.

Mandel, R.D., Murphy, L.R. and Mitchell, M.D., 2014, Geoarchaeology and paleoenvironmental context of the Beacon Island Site, an Agate Basin (Paleoindian) Bison Kill in northwestern North Dakota, USA: Quaternary International, **342**, 91-113.

Mandel, R.D. and Hofman, J.L., 2003, Geoarchaeological investigations at the Winger Site: A Late Paleoindian bison bonebed in Southwestern Kansas, U.S.A.: Geoarchaeology: An International Journal, v. 18, no. 1, p. 129-144. DOI: 10.1002/gea.10054

Mazza, P.P.A., Martini, F., Sala, B., Magi, M., Colombini, M.P., Giachi, G., Landucci, F., Lemorini, C., Modugno, F. and Ribechini, E., 2006, A new Palaeolithic discovery: tar-hafted stone tools in a European Mid-Pleistocene bone-bearing bed: Journal of Archaeological Science, 33, 1310-1318.

Nobes, D.C., 1999, Geophysical surveys of burial sites: A case study of the Oaro urupa: Geophysics, v. 64, no. 2, p. 357-367.

Nuzzo, L., Leucci, G., Negri, S., Carrozzo, M.T., and Quarta, T., 2002, Application of 3D visualization techniques in the analysis of GPR data for archaeology: Annals of Geophysics, **45**, 321-337.

Pipan, M., Baradello, L., Forte, E., Prizzon, A., and Finetti, I., 1999, 2-D and 3-D processing and interpretation of multi-fold ground penetrating radar data: a case history from an archaeological site: Journal of Applied Geophysics, **41**, 271-292.

Powell, K., 2004, Detecting buried human remains using near-surface geophysical instruments: Exploration Geophysics, v. 35, p. 88-92. DOI: 10.1071/EG04088.

Pringle, J.K., Holland, C., Szkornik, K., and Harrison, M., 2012, Establishing forensic search methodologies and geophysical surveying for the detection of clandestine graves in coastal beach environments: Forensic Science International, v. 219, p. e29-e36. DOI: 10.1016/j.forsciint.2012.01.010

Schneider, B.B., Mandel, R.M., Tsoflias, G.P., De Vore, S.L., and Lynott, M., 2016, Combining ER and GPR surveys for evidence of prehistoric landscape construction: case study at Mound City, Ohio, USA: Journal of Applied Geophysics, v. 129, p. 178-186. doi: 10.1016/j.jappgeo.2016.04.002.

Schultz, J.J. and Martin, M.M., 2011, Controlled GPR grave research: comparison of reflection profiles between 500 and 250 MHz antennae: Forensic Science International, **209**, 64-69.

Simmons, A.H., 1988, Extinct Pygmy Hippopotamus and early man in Cyprus: Nature, **333**, 554-557.

Sternberg, B.K. and McGill, J.W., 1995, Archaeology studies in southern Arizona using ground penetrating radar: Journal of Applied Geophysics, **33**, 209-225.

Todd, L.C., Hofman, J.L., and Schultz, C.B., 1992, Faunal analysis and paleoindian studies: a

reexamination of the Lipscomb Bison Bonebed: Plains Anthropologist, v. 37, no. 139, p. 137-165.

Uerpmann, H., 1973, Animal bone finds and economic archaeology: a critical study of 'osteo-archaeological' method: World Archaeology, **4**, 307-322.

Urban, T.M., Leon, J.F., Manning, S.W., and Fisher, K.D., 2014, High resolution GPR mapping of Late Bronze Age architecture at Kalavasos-*Ayios Dhimitrios*, Cyprus: Journal of Applied Geophysics, **107**, 129-136.

Wen-ke, Z., Gang, T., Bang-Bing, W., Zhan-Jie, S., and Jin-Xin, L., 2012, Application of 3D GPR attribute technology in archaeological investigations: Applied Geophysics, **9**, 261-269.

Whittaker, William E., and Storey, Glenn R., 2008, Ground-Penetrating Radar Survey of the Sny Magill Mound Group, Effigy Mounds National Monument, Iowa: Geoarchaeology: An International Journal, v. 23, no. 4, p. 479-499. DOI: 10.1002/gea.20229.

Material	Relative Permittivity	σ (mS/m)	V (m/ns)	α (dB/m)
Air	1	0	0.30	0
Fresh Water	80	0.5	0.033	0.1
Sea Water	80	30000	0.01	10^3
Dry Sand	3-5	0.01	0.15	0.01
Saturated Sand	20-30	0.1-1.0	0.06	0.03-0.3
Silts	5-30	1-100	0.07	1-100
Clays	5-40	2-1000	0.06	1-300

Table 1.1: Relative permittivity, electrical conductivity, signal velocity, and attenuation values of common geological materials encountered at archaeological sites. These values assume a central frequency of 100 MHz (adapted from Davis and Annan, 1989).

Signal Frequency	Sediment Type	Resolution (m)
100 MHz	Sand	0.375
100 MHz	Silt	0.175
100 MHz	Clay	0.15
500 MHz	Sand	0.075
500 MHz	Silt	0.035
500 MHz	Clay	0.03
1000 MHz	Sand	0.0375
1000 MHz	Silt	0.0175
1000 MHz	Clay	0.015

Table 1.2: Estimated resolution capabilities of GPR at frequencies of 100 MHz, 500 MHz and 1000 MHz for sands, silts, and clays. These estimations are based off of the velocities provided in Table 1.1 for dry sand, silts, and clays.

CHAPTER 2

Bone Permittivity and its Effect on Using GPR to Detect Prehistoric Animal Remains

2.0 Introduction

In order to accurately predict the GPR response of buried bone beds, additional information about the permittivity properties of bone is needed. The objective of this investigation is to measure the permittivity of samples of modern cow, elk, bison, and deer in the frequency range of 10-1000 MHz to examine if different species of bone have different permittivity and to assess the effect of varying frequency. These species were selected because they are closely related to the types of animal bone found at prehistoric archaeological sites and their bone size is large enough to be detected by GPR. This investigation also reports the permittivity measurements of one sample of Pleistocene age mammoth rib bone. Bone sample porosity, bulk density, water saturation and volumetric water content of the modern bone specimens were also accounted for during time of measurement.

Bone is composed primarily of four components: 50-70 % consists of mineral content (mostly hydroxyapatite), 20-40 % organic matrix, 5-10 % water, and less than 3 % lipids (Clarke, 2008). For the purposes of this study, the mineral content will be the main focus because that is usually all that remains of bone at archaeological sites. Hydroxyapatite crystals [$Ca_{10}(PO_4)(OH)_2$] in bone has two major differences compared to geologic hydroxyapatite crystals: they are smaller, measuring approximately 200 x 10^{-10} m in largest dimension, and they are more soluble than geologic hydroxyapatite crystals in order to support mineral metabolism in living organisms (Clarke, 2008).

The electrical properties of bone are of significant interest to the biomedical community. Human and animal bone properties such as the relative permittivity, electrical impedance, electrical resistivity, and conductivity have been investigated because electrical stimulation can be used to treat diseases such as arthritis and osteoporosis. The majority of this research has used frequency ranges lower than GPR applications and the bone samples are measured in various conditions (i.e. saturated in saline solutions in order to mimic fresh *in vivo* bone, exposed to ultraviolet radiation, etc.) which has resulted in a wide range of relative permittivity values. However, all of these investigations have shown that the relative permittivity of bone is frequency dependent, and it decreases with increasing frequency (Singh and Beharl 1984; Reddy and Saha 1984; Behari, 2009). In addition, anisotropy has been observed in the specific resistance of bone (Kosterich et al., 1983). Table 2.1 summarizes the range of relative permittivity values reported out by this research, as well as the source of the bone specimen, frequency ranges used, and the measurement methodology. In addition, Table 1 lists the reported relative permittivity values of minerals that are assumed to be similar or the same as bone mineral (i.e. geological apatite or synthetic hydroxyapatite).

2.1 Methodology

2.1.1 Permittivity Measurements

The complex permittivity of a material determines the displacement current properties at the frequency range (10 MHz – 1000 MHz) typically used in GPR investigations (Davis and Annan, 1989). The complex permittivity (ε^*) is given by equation 1

$$\varepsilon^* = \varepsilon' + i\varepsilon'' \quad (1)$$

where ε' is the real part and ε" is the imaginary or loss factor. ε' measures the capability of storage of electric-field energy, whereas ε" measures the energy loss through conductivity or polarization currents (Sheriff, 2013; von Hippel, 1995). The relative permittivity is defined as $\varepsilon = \varepsilon'/\varepsilon_o$ where ε_o is the permittivity of free space (8.84×10^{-12} F/m) (also known as the dielectric constant). The loss tangent, tanδ, is the ratio of ε"/ε' and is used to measure the energy-loss characteristics of a material. For the remainder of this dissertation, the term dielectric properties will be used when referring to all three properties at once (relative permittivity, loss factor, and loss tangent).

Network analyzers are a popular tool for providing quick, accurate complex permittivity measurements over a wide frequency range. There are a variety of different measurement techniques, including coaxial probes, transmission lines, resonance cavities, and parallel plate capacitors. For this research, the dielectric properties of bone samples were measured using an Agilent E4991A RF Impedance/Material Analyzer with a dielectric material test fixture (Keysight E4991A RF Impedance/Material Analyzer, 2016). This method works best for thin solid sheets of material over a frequency range of 1 MHz to 1 GHz using a parallel plate configuration (Figure 2.1). The parallel plate set-up places a thin sheet of target material between two planar electrodes to form a capacitor. Equation 2 describes the relationship of capacitance to permittivity

$$C = \frac{\varepsilon^* * A}{d} \tag{2}$$

where C is the capacitance (F), ε* is the complex permittivity (F/m), A is the area of the plates (m^2), and d is the separation distance (m) between the two plates which equals the thickness of the sample. Using the measured capacitance, and the known area of the plates and distance

between the plates, the complex permittivity can be calculated. From this, the instrument reports the dielectric properties for each measurement. A total of 701 points were collected over the frequency sweep of 10 MHz to 1 GHz and the measurement time per sample took approximately 1 second. The accuracy of the measurement can vary depending on the thickness of the material used. Lower relative permittivity values typically associated with dielectric materials and their mineral constituents (e.g. relative permittivity values ranging 5-10) have the highest accuracy ranging from 8-15% in the 10 MHz to 1 GHz frequency range (Keysight Technologies E4991B Impedance/Material Analyzer Data Sheet, 2016) (Appendix 1). Error from this method can be introduced if there is a large amount of airgap between the electrode and the surface of the sample being measured (Keysight Technologies Solutions for Measuring Permittivity Application Note, 2017). However, this error is reduced when dealing with samples that have low complex permittivity values. Samples were inserted into the machine at the maximum pressure to ensure the airgap error remained extremely low, if not negligible.

Thin sections of the bone samples were made and their dielectric properties were measured. The bones that met the thin section requirements of 1 mm thickness and greater than 15 mm diameter were typically long bones, such as the humerus, tibia, and femur. However, some thin sections were able to be collected from flat bone (primarily rib bone or pelvis bone) and some irregular bone (such as vertebrate) (Frandson et al., 2009). All samples were cored perpendicular to the long axis of the bone in order to minimize variation which might be due to the orientation. A total of 27 bison, 23 cow, 22 elk, 20 deer, and 1 mammoth thin sections were cut at a thickness of approximately 1 mm (Appendix 2). Instrument calibration and sample permittivity measurements were performed following the protocol described in the instrument manual (Appendix 3). The analyzer was calibrated using an open, short, and load calibration at

the fixture. Calibration and sample measurements were all conducted at a temperature of 20° C and ambient-environment humidity. The ambient environment humidity did not fluctuate during individual measurements, and all samples were kept in sealed bags except during the time of measurement. The test fixture had a 10 mm wide diameter on the upper electrode and a 7 mm diameter on the lower electrode. Three measurements were collected over each modern sample and four measurements were collected over the one mammoth sample in order to account for the electrical properties of the entire sample. The average relative permittivity, loss factor, and loss tangent were then calculated for each (Appendix 4).

2.1.2 Porosity and Bulk Density Measurements

Porosity measurements were made in order to determine how much the void space, and the fluid filling the void space, contributed to the measured sample permittivity values. Porosity measurements were made using the Archimedes method as described by Crain (2015). The pore volume of each thin section is calculated using equation 3 by comparing the dry and saturated weights of a sample,

$$Vp = \frac{W_{sat} - W_{dry}}{\rho_{wtr}} \quad (3)$$

where W_{dry} is the dry weight of the sample (g), W_{sat} is the saturated weight of the sample (g), and ρ_{wtr} is the density of water (g/cm^3). Dry weights were recorded after each sample had been placed in an oven at 105° C for 48 hours and then cooled in a desiccator for an additional 12 hours. Saturated weights were recorded after each sample was placed in a beaker of deionized water and placed in a vacuum for 10 hours, then immediately weighed. The bulk volume of each

thin section is calculated using equation 4

$$Vb = \frac{W_{sat} - W_{wet}}{\rho_{wtr}} \quad (4)$$

where W_{wet} is the weight of the saturated sample immersed in water (g). Subtracting the weight of the saturated sample immersed in water from the weight of the saturated sample yields the weight of the water displaced. Once the bulk volume and pore volume have been determined, sample porosity is calculated using equation 5

$$\emptyset = \frac{Vp}{Vb} \quad (5)$$

where $\emptyset$ is a porosity percentage (Appendix 5).

Bulk density measurements were also made to see if there was a difference in values between different animal types. The bulk density (ρ_B) is measured using the saturated weight of the sample and dividing it by the bulk volume of the sample, as shown in equation 6.

$$\rho_B = \frac{W_{sat}}{V_b} \quad (6)$$

2.1.3 Water Saturation and Volumetric Water Content Measurements

Water saturation (S_w) was recorded for each sample after collecting the permittivity measurements. Water saturation was measured using the difference of the saturated weight of the sample and weight of the sample at time of measurement (W_t) and dividing it by the difference of the saturated and dry weight of the sample, as shown in equation 7.

$$S_w = 1 - \frac{(W_{sat} - W_t)}{(W_{sat} - W_{dry})} \quad (7)$$

With this information, the overall volumetric water content of each individual sample was calculated using equation 8 (Appendix 5).

$$\theta_v = \emptyset * S_w \quad (8)$$

2.2 RESULTS

2.2.1 Permittivity Measurements

Results of the measurements of relative permittivity, loss factor and loss tangent averaged over all samples are shown in Figure 2.2. Over the frequency range 10 MHz -1000 MHz, the five species bone relative permittivity ranged from 10.6 to 7.7, the loss factor 0.23 to 0.77 and the loss tangent 0.025 to 0.092. Relative permittivity values decreased with increasing frequency and loss factor and loss tangent values both increased with increasing frequency for the four modern species. Statistically significant differences in mean values are noted between these different species, with the exception of bison to cow and deer to elk (Table 2.1).

The one mammoth bone sample revealed interesting results. The relative permittivity values fall between the two sets of modern species in the lower frequencies, and converge with the elk and deer species as the frequency increases. This pattern does not repeat when evaluating the loss factor or loss tangent values, instead the mammoth values converge with the bison and cow for the loss factor measurements and are slightly higher than the bison and cow for the loss tangent measurements.

2.2.2 Porosity, Bulk Density, Water Saturation, and Volumetric Water Content

Measurements

Sample porosity, bulk density, water saturation and volumetric water content were compared among the modern species bone samples to determine if any of these parameters could be the cause for the differences in permittivity across the two groups of species. Table 2.2 lists the minimum, maximum and average for these four parameters. Table 2.3 lists the results of the t-test analyses completed to determine if there was statistically significant difference in means between the fauna and these four parameters. No porosity, bulk density, water saturation, or volumetric water content data was collected for the mammoth bone sample in order to avoid any damage to the sample.

Average porosity values for the four modern species ranged from 22% to 25%, with only one combination (cow-elk) demonstrating a statistically significant difference in mean. Average bulk density values ranged from 1.95 to 2.23 g/cm^3. The cow-elk and elk-deer were the only combinations to exhibit a statistically significant difference in mean. Water saturation levels were fairly consistent across samples, with averages ranging from 69% to 74%. No statistically significant differences were found across the four species. Volumetric water content values were also fairly consistent across samples, with averages ranging from 16% to 18%. Similar to the bulk density, the cow-elk and elk-deer were the only combinations to exhibit a statistically significant difference in mean.

Cross plots of all samples measured relative permittivity versus porosity, water saturation, bulk density, and volumetric water content are shown in Figure 2.3. Cross plots of all samples measured relative permittivity versus porosity and water saturation are broken down into animal types in Figures 2.4 and 2.5. The volumetric water content and bulk density parameters

show no correlation with samples measured relative permittivity results. Porosity measurements exhibit a very weak negative correlation with increasing relative permittivity, whereas water saturation measurements exhibit a weak positive correlation with increasing relative permittivity. Results of the correlations support the interpretation that these four parameters do not explain the difference in bone relative permittivity values between species presented in Figure 2.2.

2.3 Discussion

This research reports the electrical properties of bone in the frequency ranges of 10 MHz to 1000 MHz of four modern large-animal fauna and one sample of prehistoric mammoth bone. The loss tangent values indicate that animal bone is a low-loss dielectric, similar to materials such as silicone rubber or concrete. The results also show that the relative permittivity of animal bone decreases as frequency increases, which is in agreement with previously published studies at lower frequencies.

One consideration that generally must be taken into account when estimating permittivity values is water saturation levels (Knight and Endres, 2005). Increasing saturation levels will increase the permittivity of a material, which can also affect initial GPR modelling parameters. Of the four variables measured, water saturation and porosity do exhibit a weak trend with the measured relative permittivity values; an increase in water saturation increases the overall relative permittivity values and an increase in porosity trends with an overall decrease in relative permittivity values. Between the two, water saturation has the highest R^2 value.

It is worth noting that the trends between water saturation and porosity varies significantly by animal type. For example, the bison samples contain two outliers in samples B9

and B22. Sample B9 measured significantly lower relative permittivity values than the other samples. This can be attributed to large open pores that occurred along the surface of the sample (Figure 2.6), which increase the error associated with this samples dielectric properties measurement. Sample B22 does not show any differences in appearance compared to the other samples, but was recorded to have a much higher porosity and water saturation than the corresponding samples with little difference in its relative permittivity measurement value. This may just be an anomalous sample, or there may be some measurement error attributed to this reading. If these two outliers are removed from the sample pool, the R^2 values improve (Figures 2.4 and 2.5). Overall, the bulk density and volumetric water content did not reveal any trends with the relative permittivity values.

The differences observed in the values of the bone permittivity of the five different species is a significant result. As shown in other studies (Kosterich, 1983; Reddy and Saha, 1984; Singh and Beharl, 1984; Behari, 2009), overall sample permittivity decreased with increasing frequency, but two distinct groups of modern species were evident in our data. Therefore, assuming one range of permittivity values at varying frequencies for all bone is not accurate and can affect ground-penetrating radar modelling and interpretations. For example, the mammoth bone relative permittivity measurement falls within the overall relative permittivity value range of the four modern species, but is actually closer to (within one standard deviation) the lower values of the deer and elk species and not the higher values of the cow and bison species. Overall, the results of the porosity, bulk density, and saturation levels of the samples during time of measurement do not explain the differences in relative permittivity measurements between the different groups of modern species. These differences may be attributed instead to the microscopic structure and chemical composition of the bones.

Research has shown that osteons, the structural unit of compact bone that is composed of a central vascular canal (also known as Haversian) and the concentric lamellae surrounding it, tend to align in rows (osteon banding) or form rectanguloid structures (plexiform bone) in animal bone, unlike human bone where the osteons are scattered and evenly spaced (White and Folkens, 2005). Singh and Saha (1984) reviewed different studies of dielectric properties of human and animal bone in lower frequency ranges (1 KHz to 70 MHz) and found that several reports suggest that the dielectric properties of human bone may have significant differences from the dielectric properties of animal bone due to their structural differences. In animals, considerable variety in the microstructure exists between species and between bones of the same animal and must be taken into consideration (Mulhern and Ubelaker, 2012).

Other microscopic structural differences have been noted between rat, cat, dog, hare, badger, and deer due to the differences in the general appearance of cortical bone tissue and the size of the histological microstructures (i.e. Haversian system diameter, canal diameter, and system density) (Hillier and Bell, 2007). These microstructures can also be influenced by biomechanical forces on the bone, such as age, sex, nutritional factors, and disease states of the individuals, which was not accounted for in this study. Differences in the chemical composition of buried animal bone has been also been documented (Locock et al., 1992). Decay factors such as length of burial and soil chemistry can significantly change the chemical composition of buried bone (White and Hannus, 1983; Gordon and Buikstra, 1981), which can affect the electrical properties of the materials. Future work should examine these differences on the permittivity of different species of animal bone, as well as the differences in microstructure in human bone, to see if this is a contributing factor to the results presented here.

2.4 Conclusions

This study provides the electrical properties of bone in the frequency ranges of 10 MHz to 1000 MHz of four modern large fauna and one sample of prehistoric mammoth bone. Our data reveals that the relative permittivity of bone mineral for each animal type decreases with increasing frequency, whereas loss factor and loss tangent increase with frequency. Our data also reveal that there is a statistically significant difference in the relative permittivity values of different species of animal that is not related to the porosity, bulk density, or water saturation levels of the bone. Future research should analyze the effect of differences in bone microstructure of different species. For future research, samples with a greater variability in stages of weathering (which assumes greater variability in porosity levels) should be analyzed at increasing saturation levels to examine a wider range of parameters and validate further the findings of this study.

References

Behari, J., 2009, Biophysical bone behavior principles and applications: Singapore, John Wiley and Sons, 483 p.

Clarke, B., 2008, Normal bone anatomy and physiology: Clinical Journal of the American Society of Nephrology, v. 3, p. S131-S139. DOI: 10.2215/CJN.04151206.

Crain's Petrophysical Handbook, 2015, Coring and core porosity: https://www.spec2000.net/09corepore.htm.

Davis, J.L., and Annan, A.P., 1989, Ground-penetrating radar for high-resolution mapping of soil and rock stratigraphy: Geophysical Prospecting, v. 37, p. 531-551.

Feranec, R.S. and Kozlowski, A.L., 2012, New AMS radiocarbon dates from late Pleistocene mastodons and mammoths in New York state, USA: Radiocarbon, v. 54, n. 2, p. 275-279.

Gordon, C.C. and Buikstra, J.E., 1981, Soil pH, bone preservation, and sampling bias at mortuary sites: American Antiquity, v. 46, no. 3, p. 566-571.

Hillier, M.L. and Bell, L.S., 2007, Differentiating human bone from animal bone: a review of histological methods: Journal of Forensic Science, v. 52, no. 2, p. 249-263. DOI: 10.1111/j.1556-4029.2006.00368.x

"Agilent E4991A RF Impedance/Material Analyzer Data Sheet," *Keysight Technologies.* Last modified October 20, 2016. http://literature.cdn.keysight.com/litweb/pdf/5991-3893EN.pdf?id=2466922

"Solutions for Measuring Permittivity and Permeability with LCR Meters and Impedance Analyzers," *Keysight Technologies*. Last modified June 12, 2016. http://literature.cdn.keysight.com/litweb/pdf/5980-2862EN.pdf?id=1000002028:epsg:apn

Knight, R.J. and Endres, A.L., 2005, An introduction to rock physics principles for near-surface peophysics, in: Butler, D.K. (Ed.), Near-Surface Geophysics. Society of Exploration Geophysicists, Tulsa, Oklahoma, p. 31-70.

Kosterich, J.D., Foster, K.R., and Pollack, S.R., 1983, Dielectric permittivity and electrical conductivity of fluid saturated bone: IEEE Transactions on Biomedical Engineering, v. 30, no. 2, p. 81-86.

Locock, M., Currie, C.K., and Gray, S., 1992, Chemical changes in buried animal bone: data from a post medieval assemblage: International Journal of Osteoarchaeology, v. 2, p. 297-304.

Mulhern, D.M. and Ubelaker, D.H., 2012, Differentiating human from nonhuman bone microstructure *in* Bone Histology: An Anthropological Perspective, edited by C. Crowder and S. Stout, p. 109-131. New York City, CRC Press.

Reddy, G.N. and Saha, S., 1984, Electrical and dielectric properties of wet bone as a function of frequency: IEEE Transactions on Biomedical Engineering, v. BME-31, no. 3, p. 296-303.

Sheriff, R.E., 2002, Encyclopedic dictionary of applied geophysics: Society of Exploration Geophysicists, Tulsa, OK, 429 p.

Singh, S. and Beharl, J., 1984, Frequency dependence of electrical properties of human bone: Journal of Bioelectricity, v. 3, no. 1-2, p. 347-356.

Singh, S. and Saha, S., 1984, Electrical properties of bone: a review: Clinical Orthopedic and Related Research, v. 186, p. 249-271.

von Hippel, A., 1995, Dielectric materials and applications: Library of Congress, Boston, MS, 438 p.

White, T.D. and Folken, P.A., 2005, The human bone manual: Elsevier Academic Press, Burlington, MA, 464 p.

White, E.M. and Hannus, L.A., 1983, Chemical weathering of bone in archaeological soils: American Antiquity, v. 48, no. 2, p. 316-322.

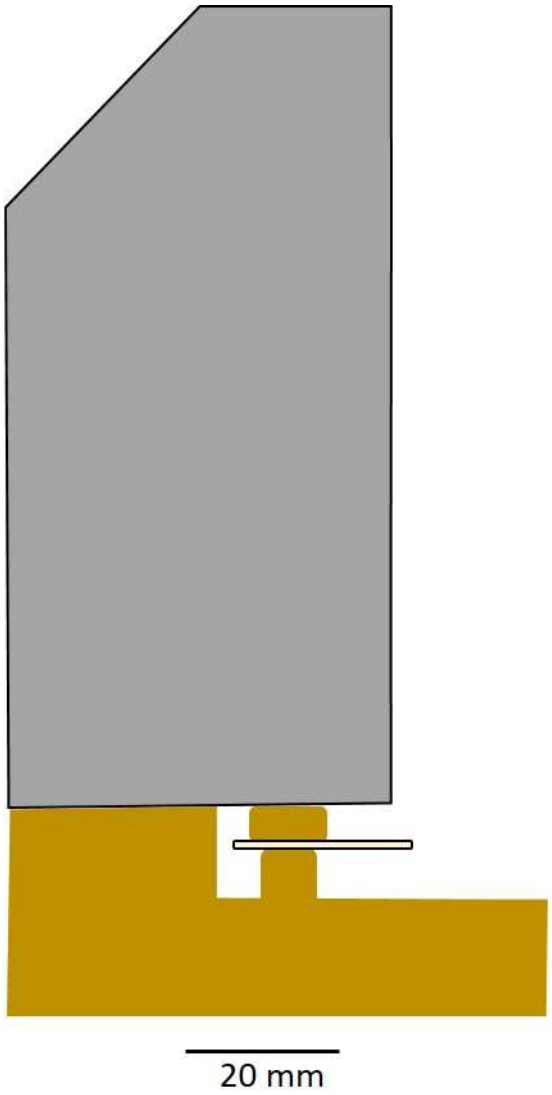

Figure 2.1: Schematic of the parallel plate capacitor used to determine the relative permittivity of a dielectric sample of thickness d placed between two plate electrodes with area A.

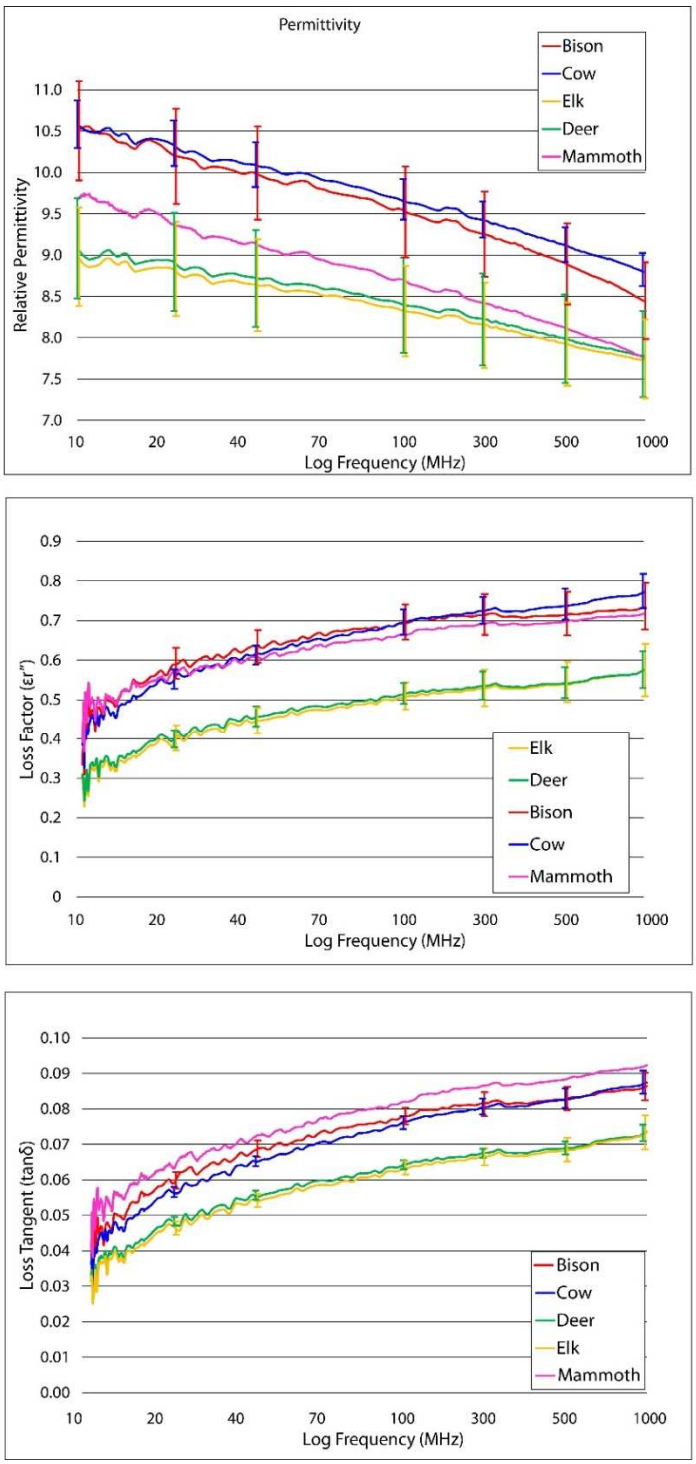

Figure 2.2: Relative permittivity ε_r' (top), loss factor ε_r'' (middle) and Loss Tangent tanδ (bottom) of five species over a frequency sweep of 10 MHz to 1 GHz. Representative error bars are displayed for each plot. Error bars represent one standard deviation.

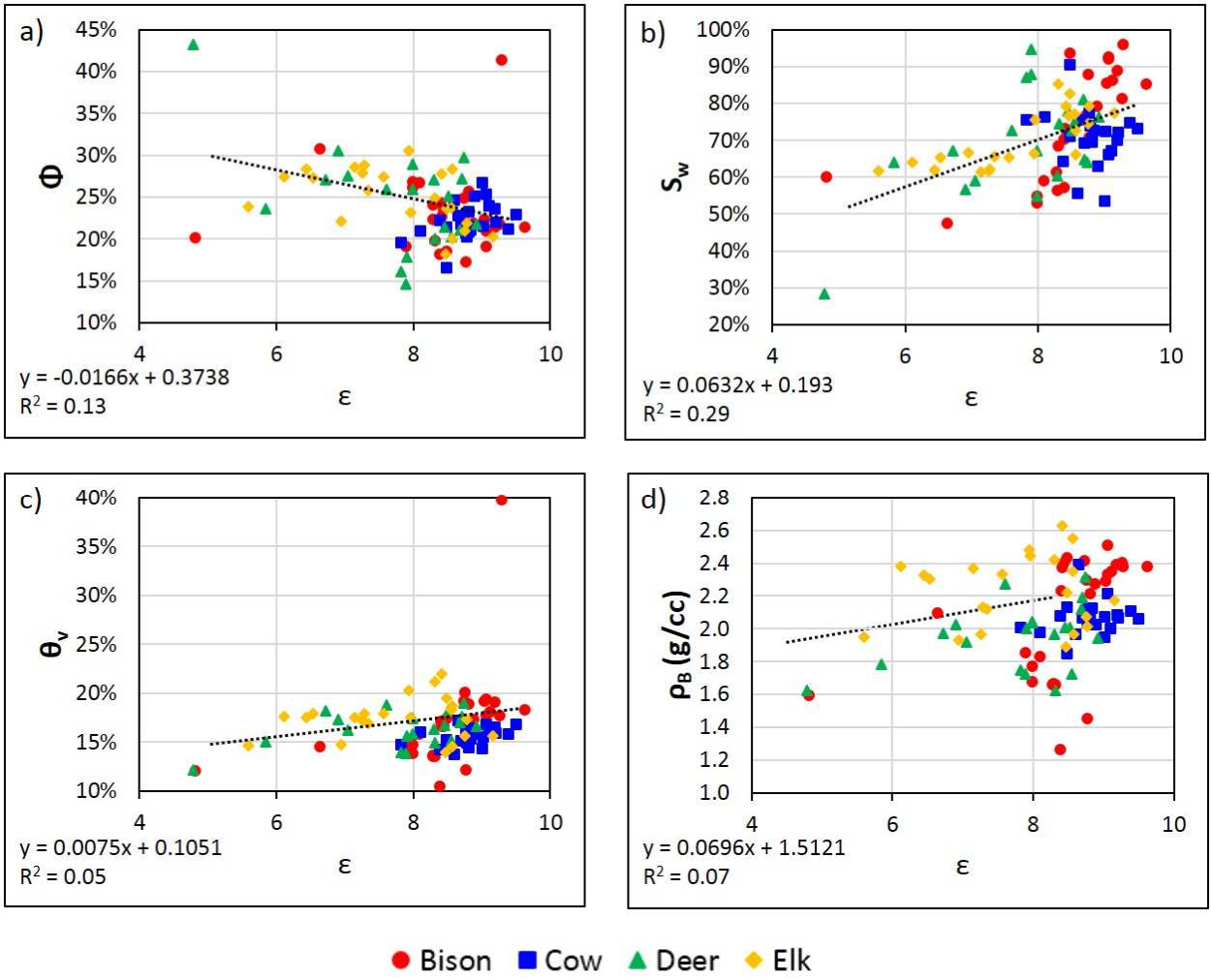

Figure 2.3: Correlation plots comparing recorded relative permittivity values sample porosity (a), water saturation (b), volumetric water content (c) and bulk density (d) at a frequency of 1 GHz with corresponding R^2 values for all of the bone samples.

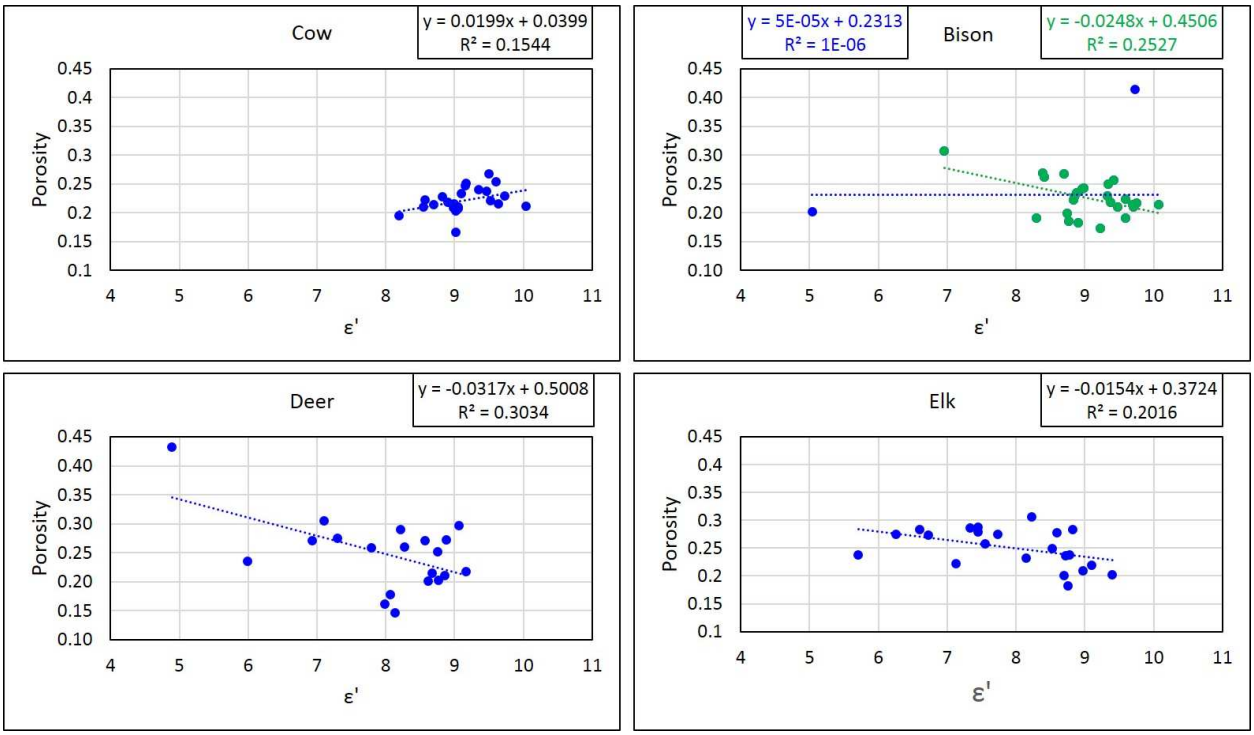

Figure 2.4: Breakdown of the correlation plots of relative permittivity values versus sample porosity at a frequency of 500 MHz for cow (top left), bison (top right), deer (bottom left), and elk (bottom right). For the bison, the green sample pool has eliminated the two outliers from samples B9 and B22.

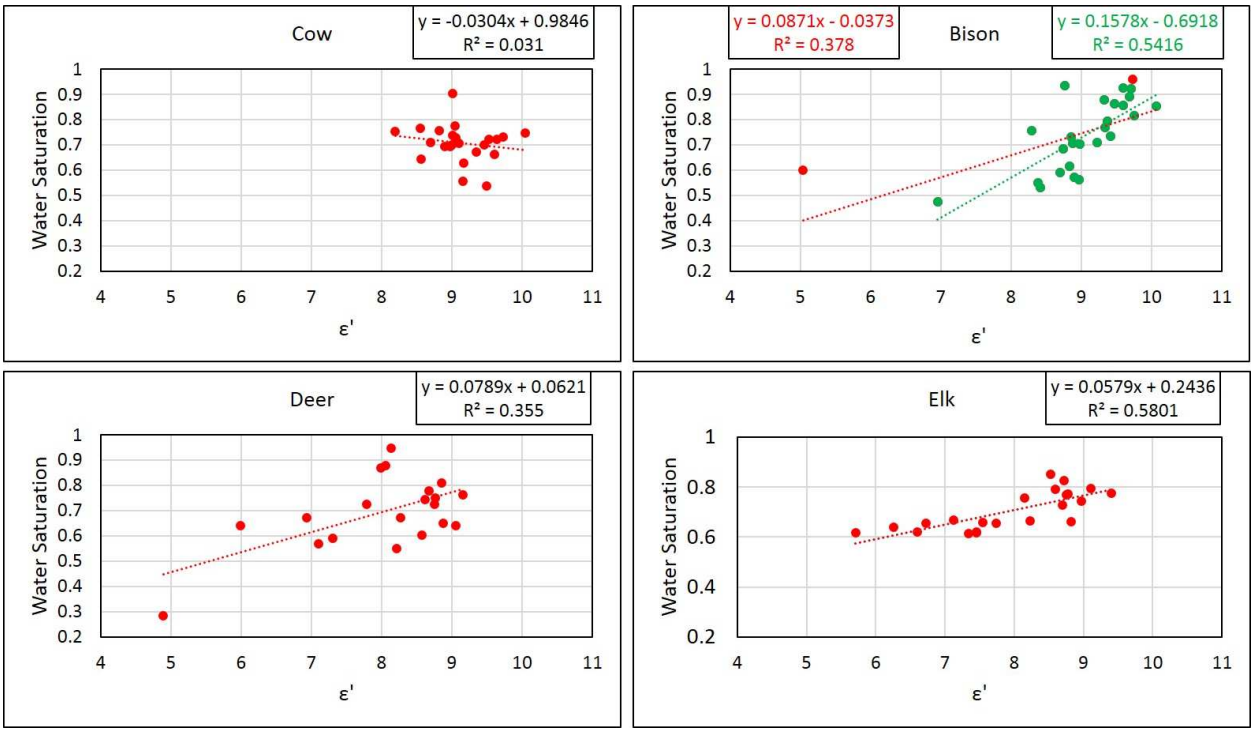

Figure 2.5: Breakdown of the correlation plots of relative permittivity values versus sample water saturation at a frequency of 500 MHz for cow (top left), bison (top right), deer (bottom left), and elk (bottom right). For the bison, the green sample pool has eliminated the two outliers from samples B9 and B22.

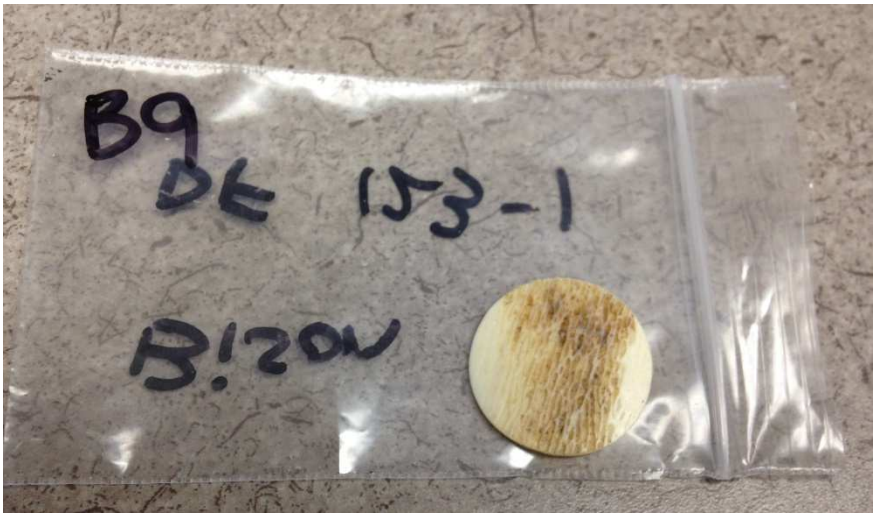

Figure 2.6: Photo of bison thin section sample B9, which had open pores at the surface. These pores resulted in a lower measured relative permittivity value as compared to the other thin section samples due to the contribution of air at electrode interface during measurement.

Source	Bone Description	Electrical Properties Reported	Frequencies	Measurement Method
Singh and Behari (1984)	Human Femur at Room Temperature (70° F, 50% Humidity)	ε_r'= 24 - 5 ER = 15 - 0	1 MHz – 70 MHz	Q Meter (HP Model 4342a)
Reddy and Saha (1984)	Fluid Saturated Bovine femurs	ε_r' = 1000 - 50 ER (axial) = 18 - 12 ER (radial) = 55 - 33 ER (circum.) = 37 – 2	1 KHz – 1 MHz	Electrical Equivalent Circuit
Kosterich et al (1983)	Fluid Saturated Rat Femur	ε_r' = 8500 – 20 EC = 10 - 60	10 Hz – 100 MHz	Impedance Analyzer
Behari (2009)	Goat Femur (Wet, Dry, and UV-Radiated)	ε_r' (wet) = 23 - 19 ε_r' (dry) = 25 - 23 ε_r' (UV) = 21 - 15	400 MHz – 1300 MHz	Reflection Transmission Test
Church et al (1988)	Geologic apatite at Room Temperature	ε_r' (300 MHz) = 9.65 ε_r' (400 MHz) = 8.97 ε_r' (500 MHz) = 9.21 ε_r' (600 MHz) = 9.64 ε_r' (700 MHz) = 9.14 ε_r' (800 MHz) = 8.85 ε_r' (900 MHz) = 9.39 ε_r' (1000 MHz) = 9.43	300 MHz – 1000 MHz	Impedance Analyzer
Hoepfner and Case (2002)	Sintered Hydroxylapate	ε_r' = 12.79 – 14.26 (approximate)	45 KHz – 7.3 MHz	Variable Impedance Bridge

Table 2.1: Reported electrical properties for bone, apatite, and sintered hydroxylapatite. ε_r' represents relative permittivity, ER is electrical resistivity (in kΩ/cm), and EC is electrical conductivity (in mS/m).

Sample Type	T.test	Degrees of Freedom	P-value	99% confidence interval	Accept or Reject Null Hypothesis that means are equal
Bison-Cow	-0.77	46	0.45	2.69	Accept
Bison-Elk	3.45	45	1.24e-03	2.69	Reject
Bison-Deer	3.15	43	2.95e-03	2.70	Reject
Cow-Deer	4.68	39	3.41e-05	2.71	Reject
Cow-Elk	5.11	41	7.95e-06	2.70	Reject
Elk-Deer	-0.11	38	0.91	2.71	Accept

Table 2.2: Results of a two-tailed t.test comparing the permittivity measurements of the different modern species. All combinations, with the exception of bison-cow and elk-deer, were found to have a statistically significant difference in means.

Sample Name	Min Φ (%)	Mean Φ (%)	Max Φ (%)	S.D. (%)	Sample Name	Min S_w (%)	Mean S_w (%)	Max S_w (%)	S.D. (%)
Bison	17.24	23.18	41.45	4.78	**Bison**	47.41	74	96.01	14.16
Cow	16.58	22.19	26.71	2.18	**Cow**	53.62	70.65	90.5	7.44
Elk	18.2	25.05	30.59	3.46	**Elk**	61.28	70.36	85.2	7.7
Deer	14.64	24.75	43.23	6.27	**Deer**	28.26	69.3	94.6	14.44
Sample Name	**Min ρ_B (g/cm^3)**	**Mean ρ_B (g/cm^3)**	**Max ρ_B (g/cm^3)**	**S.D.**	**Sample Name**	**Min θ_v (%)**	**Mean θ_v (%)**	**Max θ_v (%)**	**S.D. (%)**
Bison	1.26	2.08	2.51	0.37	**Bison**	10.45	17.1	39.79	5.22
Cow	1.85	2.07	2.39	0.10	**Cow**	13.73	15.54	17.25	0.91
Elk	1.89	2.23	2.63	0.22	**Elk**	13.97	17.48	21.99	2.09
Deer	1.62	1.95	2.31	0.198	**Deer**	12.22	16.32	19.04	1.77

Table 2.3: Porosity, Bulk Density, Water Saturation, and Volumetric Water Content (VWC) min, mean, and max of the four modern species.

Porosity comparisons assuming a null hypothesis that the means are equal					Water Saturation comparisons assuming a null hypothesis that the means are equal				
Sample Type	**T.test**	**P-value**	**95% C.I.**	**Accept or Reject**	**Sample Type**	**T.test**	**P-value**	**95% C.I.**	**Accept or Reject**
B/C	0.9	0.37	2.01	Accept	B/C	1.11	0.27	2.01	Accept
B/E	-1.81	7.64e-02	2.01	Accept	B/E	1.26	0.22	2.01	Accept
B/D	-1.12	0.27	2.02	Accept	B/D	1.3	0.2	2.02	Accept
C/D	-1.98	5.52e-02	2.02	Accept	C/D	0.54	0.6	2.02	Accept
C/E	-3.81	4.56e-04	2.02	Reject	C/E	0.26	0.8	2.02	Accept
E/D	-0.24	0.81	2.02	Accept	E/D	-0.36	0.72	2.02	Accept
Bulk Density comparisons assuming a null hypothesis that the means are equal					**Volumetric Water Content comparisons assuming a null hypothesis that the means are equal**				
Sample Type	**T.test**	**P-value**	**95% C.I.**	**Accept or Reject**	**Sample Type**	**T.test**	**P-value**	**95% C.I.**	**Accept or Reject**
B/C	1.45	0.16	2.01	Accept	B/C	0.4	0.69	2.01	Accept
B/E	-0.38	0.7	2.01	Accept	B/E	-1.63	0.11	2.01	Accept
B/D	0.66	0.51	2.02	Accept	B/D	1.47	0.15	2.02	Accept
C/D	-1.88	6.75e-02	2.02	Accept	C/D	2.16	3.72e-02	2.02	Reject
C/E	-4.48	5.84e-05	2.02	Reject	C/E	-3.58	9.12e-04	2.02	Reject
E/D	2.14	3.9e-02	2.02	Reject	E/D	4.32	1.07e-04	2.02	Reject

Table 2.4: Results of a two-tailed t.test comparing the porosity, water saturation, volumetric water content, and bulk density measurements of the different modern species. The same degrees of freedom apply as seen in Table 2.2.

CHAPTER 3

Modeling Bone Permittivity for GPR Application

3.0 Introduction

Several different dielectric mixing models have been proposed in order to predict the permittivity values of multi-component geological materials. These models fall into four broad categories: empirical, volumetric, effective medium, and phenomenological (Table 3.1) (Knight and Endres, 2005; Remke et al., 2005; Martinez and Byrnes, 2001). Empirical models are mathematical descriptions that compare permittivity and other characteristics such as volumetric water content or texture of a multi-component system. Volumetric models assume that the permittivity of a multi-component system is the sum of the fractional volumes of individual components. Effective-medium models take an additional step beyond the volumetric mixing models by incorporating the geometry of the multi-component system. Finally, phenomological models compare the permittivity of a material as a function of frequency due to polarization effects.

These models have been successful at predicting the permittivity values of multi-component geological materials, in particular heterogeneous rocks and soils (Johnson and Poeter, 2005; Rust et al, 1999; Powers, 1997; Knight and Endres, 1990; Taherian et al, 1990; Dobson et al., 1985; Shen et al, 1985; Sen et al., 1981; Wang and Schmugge, 1980; Olhoeft and Strangway, 1975). For this research, measured permittivity values were compared to modeled permittivity values using three common dielectric mixing models, Hanai-Bruggeman (Greaves, 1996; Sen et al, 1981), Topp (Topp et al., 1980), and the Complex Refractive Index Model (CRIM) (Knight and Endres, 2005; Greaves et al., 1996). These three models were chosen because they each

account for variables measured in this study, i.e. porosity and water saturation. In addition, the CRIM and Hanai-Bruggeman models were specifically chosen to determine if the reported values of similar minerals such as apatite are sufficient to use when estimating bone mineral permittivity values. Finally, the CRIM and Hanai-Bruggeman mixing models were used to report out new permittivity values for dry bone mineral grains in the frequency range of 100-1000 MHz that should be used for future research. This chapter concludes with recommendations for which model best represents the measured bone permittivity results for future modelling applications.

3.1 Methodology

The CRIM is a volumetric mixing formula which weighs the relative permittivity based on the sum of the square root of the volume fraction of the individual component permittivity values (Knight and Endres, 2005; Greaves et al., 1996). The CRIM equation has been shown to be particularly effective for medium-to-coarse grained multi-phase mixtures involving simple granular materials at frequencies above ~100 MHz. Any number of phases can be included, but in most cases a three-phase model is appropriate to represent the permittivity of the water, gas (air), and matrix (Greaves et al., 1996). The three-phase CRIM formula is calculated using Equation 2

$$\varepsilon_s = [(\emptyset S_w\sqrt{\varepsilon_w}) + \left((1-\emptyset)\sqrt{\varepsilon_m}\right) + (\emptyset(1-S_w)\sqrt{\varepsilon_g})]^2 \quad (2)$$

where ε_s, ε_w, ε_a and ε_m are the relative permittivity of the sample, water, air, and mineral grain respectively, $\emptyset$ is the porosity, and *Sw* is the water saturation. For this research, the mineral grain permittivity was set to reported values by Church et al (1988) for apatite in the frequency ranges

of 300-1000 MHz. These values are 9.65, 8.97, 9.21, 9.64, 9.14, 8.85, 9.39, and 9.43. Water and air permittivity values were set to 79 and 1 (Maryott and Smith, 1951).

Hanai-Bruggeman is an effective medium model similar to the CRIM mixing model, but in addition to porosity and water saturation it also accounts for an additional cementation index, *m*. This ranges from a value of 1.5 for unconsolidated, well rounded grains to 2.0 for well-cemented, oblate grains (Greaves, 1996; Sen et al, 1981). In order to estimate a partially saturated sample, the equation is employed twice. The first equation (3a) solves for ε_{pore} which accounts for the water and air mixture that fills the pore space. The second equation (3b) solves for the total sample and accounts for the mineral grains in association with the pore space mixture.

$$\varepsilon_{pore} = \varepsilon_w {S_w}^m \left(\frac{1-\frac{\varepsilon_a}{\varepsilon_w}}{1-\frac{\varepsilon_a}{\varepsilon_{pore}}} \right)^m \tag{3a}$$

$$\varepsilon_s = \varepsilon_{pore} \emptyset^m \left(\frac{1-\frac{\varepsilon_g}{\varepsilon_{pore}}}{1-\frac{\varepsilon_g}{\varepsilon_s}} \right)^m \tag{3b}$$

In equation 3a, *m* is related to the shape of the air bubbles, whereas in equation 3b *m* is related to the shape of the mineral grains. For this research, each sample was evaluated twice using *m* values of 1. 5 and 2 to see if this geometrical factor contributed significantly to the different values reported between the cow/bison and deer/elk samples (see Appendix 6 for MATLAB code). Water and air permittivity values were once again set at 79 and 1, respectively. Mineral grain relative permittivity values used were the same values reported by Church et al (1988) for the CRIM model above.

The Topp equation (4) is an empirical model that predicts the relative permittivity of

materials using a third-order polynomial based on their volumetric water-content fraction and is most applicable in the 50 MHz - 1000 MHz frequency range (Annan, 2005; Topp et al., 1980).

$$\varepsilon = 3.03 + 9.3\theta_v + 146.0{\theta_v}^2 - 76.7{\theta_v}^3 \quad (4)$$

For each model, the error was calculated using equation 5.

$$Relative\ Error = \left|\frac{Measured\ Value - Predicted\ Value}{Measured\ Value}\right| \quad (5)$$

3.2 Results

Figure 3.1 shows individual species plots of the measured permittivity values with the predicted permittivity values based on the three models (CRIM, Hanai-Bruggeman, and Topp) using previously reported relative permittivity values of apatite in the frequency range of 300-1000 MHz (Church et al, 1988). The measured values shown are at a frequency of 1 GHz, because this frequency is commonly used for high-resolution geoarchaeological investigations. The Topp model shows better agreement with the measured values for each animal type, with an averaged error of 0.16 for all samples. The CRIM and Hanai-Bruggeman models both greatly overestimate the relative permittivity of the bone mineral samples. The averaged error for CRIM was 0.81 for all samples. The averaged error for the Hanai-Bruggeman model using a cementation index of 1.5 and 2 was 0.87 and 0.63, respectively. Model accuracy for all three types was evaluated using the average of the error of the samples, shown in equation 5, across the frequency spectrum of 300-1000 MHz. Figure 3.2 shows a comparative plot of the average relative error for each model across the entire frequency sweep. The good agreement using the Topp model is evidence that volumetric water content plays an important role in predicting

animal bone permittivity values, which was expected. However, both the CRIM and Hanai-Bruggeman models incorporate water saturation and porosity, which are the two main components of volumetric water content. One possible explanation for the misfit from these models would be that the relative permittivity values of geologic apatite or synthetic hydroxyapatite are not the same as the hydroxyapatite mineral that constitutes bone.

Based on these results, both the CRIM and Hanai-Bruggeman models were used to estimate relative permittivity values of dry bone mineral grain that match measured sample relative permittivity values across the frequency sweep of 100-1000 MHz. For both models, the best fit values ranged from 3-5 across the frequency sweep for the four animal types. Overall, the best fit bison and cow mineral grain relative permittivity values were higher than the elk and deer mineral grain relative permittivity values. This was expected based on the difference seen between these species in the measured permittivity values. Figure 3.3 shows a comparative plot of the best fit error for each model across this frequency sweep using the 3-5 value range.

3.3 Discussion

For modeling purposes, the Topp model matched the measured values well. These results indicate that volumetric water content plays a role in predicting relative permittivity values of modern bone samples for GPR modeling. The large misfit from both the CRIM and Hanai-Bruggeman models can be explained with two hypotheses. The first hypothesis is that the models are not appropriate for predicting the relative permittivity values of animal bone. The second hypothesis is that using the reported relative permittivity values of similar minerals, as shown in Table 1, are not suitable for predicting animal bone relative permittivity because they are higher

than the relative permittivity values of dry animal bone. All of the thin section samples measured for this research had high water saturation levels (over 50%), which means that the relative permittivity values measured are higher than they would be if the bone was dry. This is supporting evidence for the second hypothesis. The good fit of the Topp model, which accounts for volumetric water content, provides supporting evidence for the second hypothesis and suggests that both the CRIM and Hanai-Bruggeman mixing models, which account for porosity and water saturation, can be used. Based on this evidence, the two models were used to estimate the relative permittivity of dry bone mineral grains. Both models reveal a lower range of 3-5 as compared to the published values for apatite or hydroxyapatite (9-12). These values can be used for future research to help predict the detection capabilities of GPR for bone in varying depositional settings.

3.4 Conclusions

This research compared the measured sample-permittivity values to modeled sample-permittivity values using common dielectric mixing models in order to determine which parameters control the best-fit predictions of permittivity of animal bone. The Topp model fit the measured data well, indicating that volumetric water content plays a role in the relative permittivity values of animal bone. Both the CRIM and Hanai-Bruggeman models were then utilized to estimate the dry permittivity values of bone mineral grains. Both models revealed the best fit relative permittivity measurements for dry animal bone to fall in the range of 3-5 within the frequency ranges of 10 MHz to 1000 MHz. For future research, the models tested here are recommended for estimating relative permittivity values of animal bone.

References

Annan, A.P., 2005, Ground-penetrating radar, in: Butler, D.K. (Ed.), Near-Surface Geophysics. Society of Exploration Geophysicists, Tulsa, Oklahoma, p. 357-434.

Church, R.H., Webb, W.E., and Salsman, J.B., 1988, Dielectric properties of low-loss minerals: Report of Investigations 9194 Bureau of Mines, United States Department of the Interior, 14 p.

Debye, P., 1929, Polar molecules: Chemical Catalog Company, Inc., New York, 172 p.

De Loor, G.P., 1983, The dielectric properties of wet materials: IEEE Transactions on Geoscience and Remote Sensing, v. GE-21, no. 3, p. 364-369.

Dobson, M.C., Ulaby, F.T., Hallikainen, M.T. and El-Rayes, M.A., 1985, Microwave dielectric behavior of wet soil-part II: dielectric mixing models: IEEE Transactions on Geoscience and Remote Sensing, v. GE-23, no. 1, p. 35-46.

Endres, A.L. and Knight, R., 1992, A theoretical treatment of the effect of microscopic fluid distribution on the dielectric properties of partially saturated rocks: Geophysical Prospecting, v. 40, p. 307-324.

Greaves, R.J., Lesmes, D.P., Lee, J.M. and Toksoz, M.N., 1996, Velocity variations and water content estimated from multi-offset, ground-penetrating radar: Geophysics, v. 61, no. 3, p. 683-695.

Hilhorst, M.A., Dirksen, C., Kampers, F.W.H. and Feddes, R.A., 2000, New dielectric mixture equation for porous materials based on depolarization factors: Soil Science Society of America Journal, v. 64, p. 1581-1587.

Johnson, R.H. and Poeter, E.P., 2005, Iterative use of the Bruggeman-Hanai-Sen mixing model to determine water saturations in sand: Geophysics, v. 70, no. 5, p. K33-K38. doi: 10.1190/1.2049348

Knight, R.J. and Endres, A.L., 2005, An introduction to rock physics principles for near-surface geophysics, in: Butler, D.K. (Ed.), Near-Surface Geophysics. Society of Exploration Geophysicists, Tulsa, Oklahoma, p. 31-70.4

Knight, R. and Endres, A.L., 1990, A new concept in modeling the dielectric response of sandstones: defining a wetted rock and bulk water system: Geophysics, v. 55, no. 5, p. 586-594.

Martinez, A. and Brynes, A.P., 2001, Modeling dielectric-constant values of geologic materials: an aid to ground-penetrating radar data collection and interpretation: Current Research in Earth Sciences, Kansas Geological Survey, Bulletin 247, part 1: http://www.kgs.ku.edu/Current/2001/martinez/martinez1.html

Maryott, A.A. and Smith, E.R., 1951, Table of dielectric constants of pure liquids: National Bureau of Standards Circular 514, United States Department of Commerce.

Norris, A.N., Callegar, A.J. and Sheng, P., 1985, A generalized differential effective medium theory: Journal of the Mechanics and Physics of Solids, v. 33, no. 6, p. 525-543.

Olhoeft, G.R. and Strangway, D.W., 1975, Dielectric properties of the first 100 meters of the moon: Earth and Planetary Science Letters, v. 24, p. 394-404.

Powers, M.H., 1997, Modeling frequency-dependent GPR: The Leading Edge, v. 16, no. 11, p. 1657-1662.

Roth, K., Schulin, R., Fluhler, H. and Attinger, W., 1990, Calibration of time domain reflectometry for water content measurement using a composite dielectric approach: Water Resources Research, v. 26, no. 10, p. 2267-2273.

Rust, A.C., Russell, J.K. and Knight, R.J., 1999, Dielectric constant as a predictor of porosity in dry volcanic rocks: Journal of Volcanology and Geothermal Research, v. 91, p. 79-96.

Salat, C. and Junge, A., 2010, Dielectric permittivity of fine-grained fractions of soil samples from Eastern Spain at 200 MHz: Geophysics, v. 75, no. 1, p. J1-J9. doi: 10.1190/1.3294859

Sen, P.N., Scala, C. and Cohen, M.H., 1981, A self-similar model for sedimentary rocks with application to the dielectric constant of fused glass beads: Geophysics, v. 46, no. 5, p. 781-795.

Shen, L.C., Savre, W.C., Price, J.M. and Athavale, K., 1985, Dielectric properties of reservoir rocks at ultra-high frequencies: Geophysics, v. 50, no. 4, p. 692-704.

Taherian, M.R., Kenyon, W.E. and Safinya, K.A., 1990, Measurement of dielectric response of water-saturated rocks: Geophysics, v. 55, no. 12, p. 1530-1541.

Topp, G.C., Davis, J.L., and Annan, A.P., 1980, Electromagnetic determination of soil water content and electrical conductivity measurement using time domain reflectometry: Water Resources Research, v. 16, p. 574-582.

Tran, A.P., Ardekani, M.R.M., and Lambot, S., 2012, Coupling of dielectric mixing models with full-wave ground-penetrating radar signal inversion for sandy-soil-moisture estimation: Geophysics, v. 77, no. 3, p. H33-H44. doi: 10.1190/GEO2011-0100.1

Ulaby, F.T., Benga, T.H., Dobson, M.C., East, J.R., Garvin, J.B. and Evans, D.L., 1986, Microwave Dielectric Properties of Dry Rocks: IEEE Transactions on Geoscience and Remote Sensing, v. 28, no. 3, p. 325-336.

Van Dam, R. L., Borchers, B., & Hendrickx, J. M. H., 2005, Methods for prediction of soil dielectric properties: a review, in: Harmon, R.S., Broach, T., & Holloway, Jr., J.H., (Eds.), Proceedings of SPIE - The International Society for Optical Engineering, v. 5794, p. 188-197. doi: 10.1117/12.602868

Wang, J.R. and Schmugge, T.J., 1980, An empirical model for the complex dielectric permittivity of soils as a function of water content: IEEE Transactions on Geoscience

and Remote Sensing, v. GE-18, no. 4, p. 288-295.

Wharton, R. P., Hazen, G. A., Rau, R. N. and Best, D. L., 1980, Electromagnetic propagation logging—advances in technique and interpretation: Society of Petroleum Engineers, Paper 9267, 12 p.

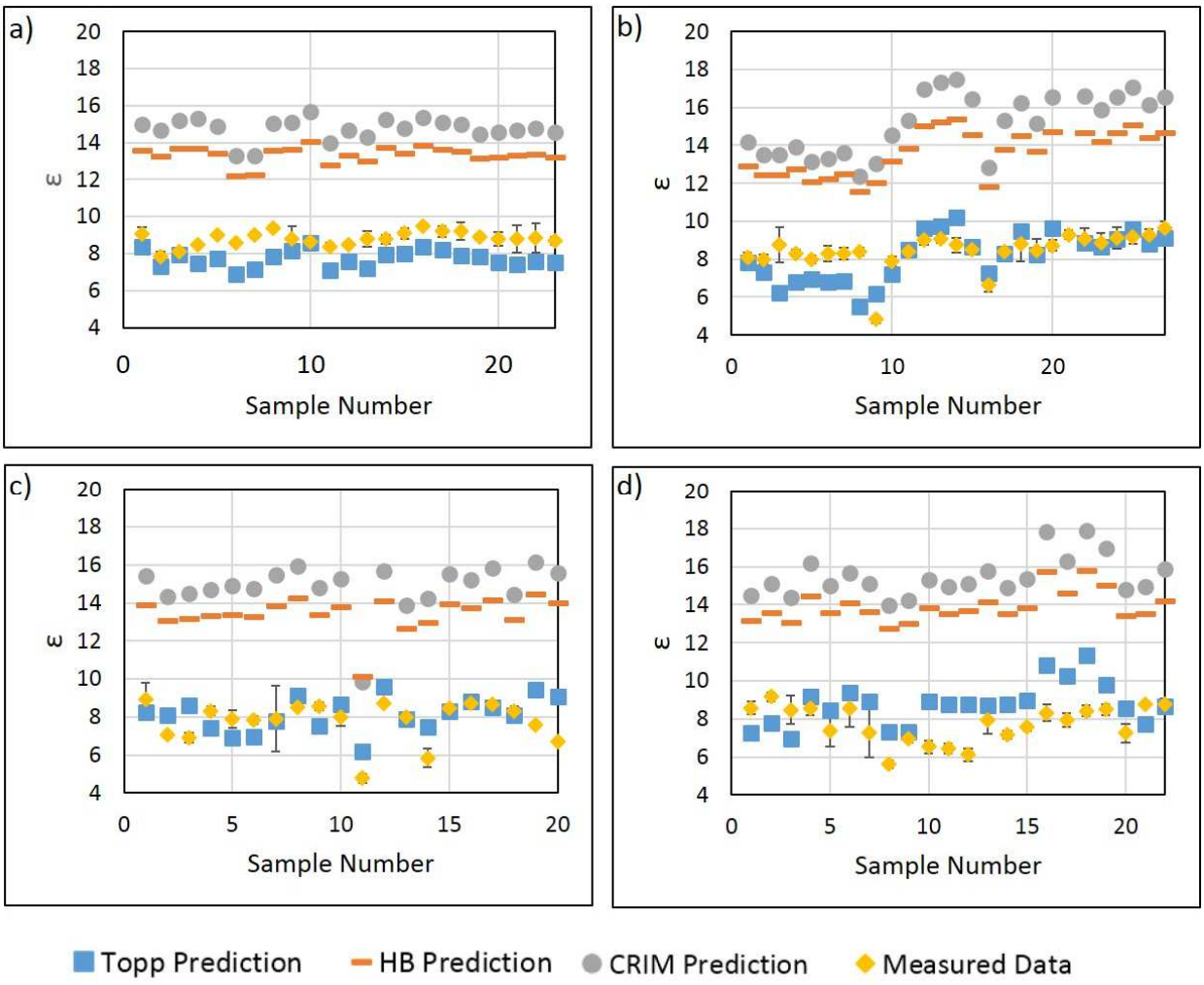

Figure 3.1: Comparison of the measured relative permittivity values for a) cow, b) bison, c) deer and d) elk compared to the three model predictions at a frequency of 1 GHz using apatite values reported by Church et al (1988). For the Hanai-Bruggeman model, values shown represent a cementation index, *m*, of 2. Ranges in the measured data represent two standard deviations. The model predictions for bison sample 22 are not shown. The predicted relative permittivity values of bison sample 22 for CRIM and Hanai-Bruggeman are 28.64 and 24.78, respectively.

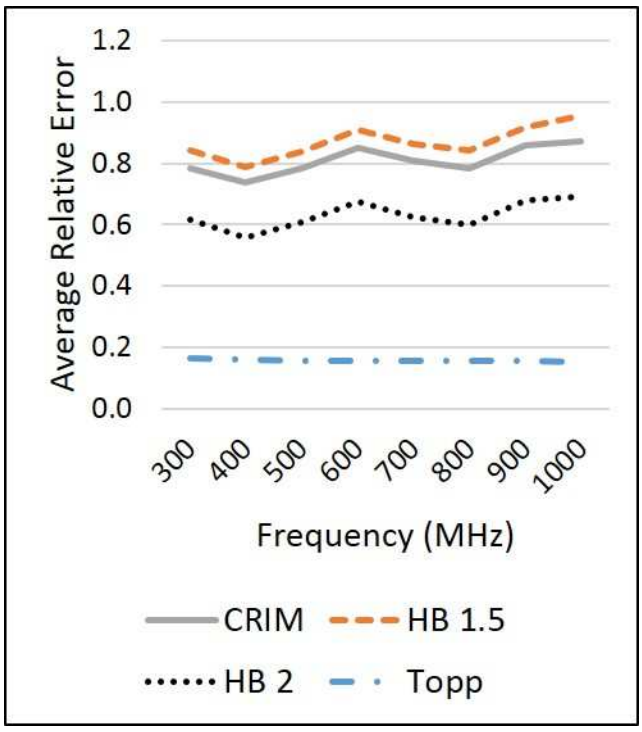

Figure 3.2: Average relative error of the three models for all samples across the frequency sweep of 300-1000 MHz. The Hanai-Bruggeman model is shown using two different cementation indexes of 1.5 and 2.

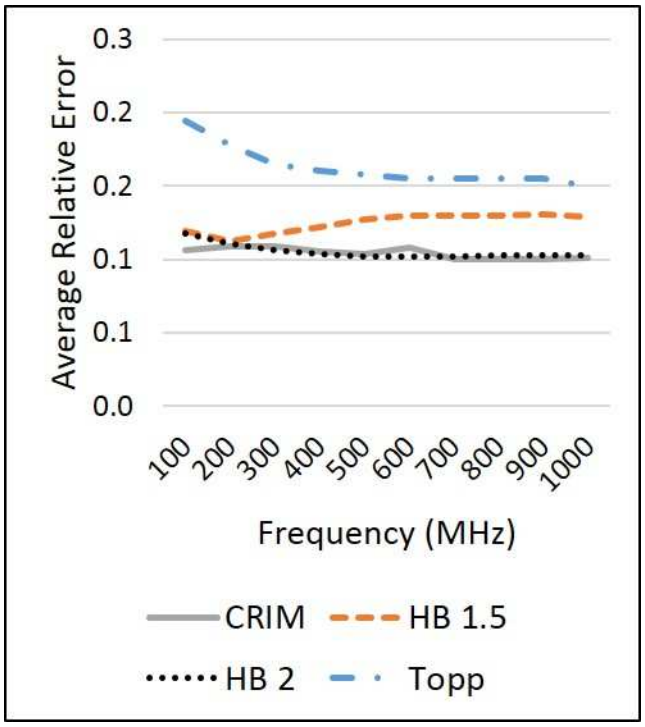

Figure 3.3: Average relative error of the three models for all samples across the frequency sweep of 100-1000 MHz using the new bone mineral relative permittivity value range of 3-5. The Hanai-Bruggeman model is shown using two different cementation indexes of 1.5 and 2.

	Effective Medium	Empirical	Phenomenological	Volumetric
Method	Computes permittivity by successive substitutions. Most commonly done using a heterogeneous medium that is represented in terms of a background phase and embedded inclusions.	Mathematical descriptions of the relationship between permittivity and other measurable properties of a medium, such as water content or porosity.	Relates frequency dependent behavior of a material to characteristic relaxation times.	Computes the permittivity of a material as a volumetric weighted average of the individual permittivity values of its principal constituents.
Types	Differential Effective Medium (DEM), Lorentz approximation, Variable Background approximation, etc.	Logarithmic, Polynomial	Cole-Cole, Cole-Davidson, Debye	Complex Refractive Index (CRIM), Arithmetic Average, Time-Propogation (TP), Harmonic Average
Advantages	Accounts for the geometry of the inclusions	Include information of physical background of dielectric behavior, easy to develop quantitative relationships	Does not require specific information on material properties	Simple to apply, different volumetric approaches can account for variables such as depolarization and inclusion distribution and orientation
Dis-advantages	Can be difficult to implement, often several unknown factors to choose from including number of components, shape of grains/inclusions, and initial material properties.	Usually only applicable to the datasets they were developed for, may be no physical justification for the relationship developed	Requires recalibration for each specific material, literature only applies to water-saturated materials and not partially-saturated materials	Does not account for the geometry of the components
References	Endres and Knight, 1992; Norris et al, 1985; de Loor, 1983; Sen et al, 1981	Roth et al., 1990; Dobson et al., 1985; Topp et al., 1980; Wang and Schmugge, 1980	Powers, 1997; Taherian et al., 1990; Ulaby et al., 1986; Debye, 1929	Hilhorst, et al., 2000; Knight and Endres, 1990; Roth et al., 1990; Wharton et al., 1980

Table 3.1: Summary of the different categories of dielectric mixing models (adapted from Knight and Endres, 2005; Remke, et al., 2005 and Martinez and Brynes, 2001).

Chapter 4

Burial conditions that affect the detection of prehistoric animal bone using ground-penetrating radar

4.0 Introduction

This study uses controlled sandbox experiments and numerical modeling to determine the effectiveness of GPR to detect the vertical and horizontal extents of buried bison bone deposits. Modern bison bone samples were used as a proxy for prehistoric bison bone, and a variety of variables were considered, including antenna frequency, size and orientation of the bone target, and the degree of bone weathering. Antenna frequency and target size are an important consideration for survey design because decreasing the frequency will allow for deeper exploration depth, but will also decrease the resolution capabilities. This trade-off could be an issue when trying to detect a single bone target. Orientation of the bone target also is a factor because increasing the dip angle of a buried target will usually reduce the amplitude as compared to a horizontal target. Finally, bone weathering is an especially important factor to consider. Prehistoric bone in archaeological contexts is often fragmented, or in such fragile condition that it must be encased in plaster in order to be removed from the ground. As bone weathers, it becomes more porous (Hedges and Millard, 1995). Porosity affects the relative permittivity of a target, and relative permittivity is one of the dominant parameters that determine electrical contrasts between subsurface targets (Annan, 2005).

Numerical modeling is useful for gaining insights on the imaging capabilities of GPR. There are a variety of numerical modeling applications that can be used for GPR studies, including but not limited to finite-difference time domain (FDTD), ray-based methods,

frequency-domain methods, and pseudospectral methods (Irving and Knight, 2006). Our study used split-step 2-D frequency-wavenumber modeling (Bitri and Grandjean, 1998), which can be conveniently accessed through the MatGPR graphic user interface (Tzanis, 2010). This model accounts for the frequency dependence of physical parameters used in Maxwell's equations. It is only applicable for 2-dimensional GPR data, but is a fast algorithm that accounts for both attenuation and dispersion in heterogeneous media. Model simulations were compared to the GPR data collected over the controlled sandbox experiments in order to test the accuracy of the numerical modeling. Based on these results, numerical models were then used to predict the detectability of buried bison bone at different stages of weathering and in different depositional settings.

4.1 Methodology

4.1.1 Ground-penetrating Radar Survey Parameters

GPR data were collected using a Sensors and Software PulseEkko system with a 1 GHz frequency antenna. For the single bone burial experiment, the 500 MHz frequency antenna was also used to evaluate detection capabilities with decreased resolution. For each experiment, a total of five lines was collected over the box at a 15 cm line spacing. Additional data collection parameters include a 2 cm trace spacing and a sampling interval of 0.1 ns.

4.1.2 Sandbox Experiments

A wooden sandbox was constructed that measured 2 m in length, 1 m in width, and 1 m

in depth, and was placed on a concrete floor. Because data were collected periodically throughout the year, the sandbox was kept indoors so that extreme changes in humidity and temperature were avoided. The sandbox was filled to the top with clean, dry, fine-grained play sand (predominantly quartz sand) (Figure 4.1). Modern bison bone samples were buried in the sand, with the orientation of the bones varying among the tests. A 2 mm thick plastic sheet was placed atop the sand during the collection of GPR data in order to ensure a flat, smooth surface. Table 4.1 describes the different experimental designs presented in this paper.

A sand matrix was chosen for several reasons. First, sand does not attenuate GPR signal as much as finer-grained silts or clays do. Also, sand allows for more rapid excavation and re-burial of bones compared to fine-grained sediment. Finally, sand does not leave a sizable disturbed soil signature that would mask the bone target, allowing us to avoid the problem encountered at graveyard and recent burial sites. Figure 4.2 shows an averaged amplitude plot of the last ten traces for each of the experiments presented here. The direct arrival and the reflection from the bottom of the box are labeled and overlap in all four experiments. No significant effects from removing and re-burying the sand are apparent.

4.1.3 Numerical Models

Numerical models were constructed that simulated the settings of the controlled sandbox experiments #1 and #2 in order to assess the accuracy of the models. In addition, two more numerical models were constructed that demonstrate the effects on GPR detection of buried bone based on changing dip angle of the buried bone and increasing weathering effects on the buried bone. Models were run in MATLAB using MatGPR (Tzanis, 2010). MatGPR offers both FDTD

and split-step modeling options. The split-step modeling was used for this research, which utilizes a frequency-wavenumber modeling approach developed by Bitri and Grandjean (1998). This model was selected because it is user-friendly, provides accurate results, and requires less computing time. Model parameters accounted for relative permittivity, electrical resistivity, and magnetic permeability. Table 4.2 lists the parameters used for each experiment. The electrical properties of bone samples that are in good condition were estimated based on previous work discussed in Chapters 2 and 3. The electrical properties for sand and concrete were estimated based on reported values from Davis and Annan (1989) and Robert (1998).

4.2. Results

4.2.1 Experiment 1: Bison Bone Layer

The results of the GPR data collected over the modern bison bone layer can be seen in Figure 4.3a. The bone layer was composed of several bison bone elements, including humeri, radials, tibia, metatarsals, mandibles, and rib (see corresponding photo in Table 4.1). Processing for all GPR data was completed in MatGPR (Tzanis, 2010). The processing steps included trimming the time window to 15 ns, bandpass frequency filtering of 500 MHz to 2 GHz, muting the direct arrival energy, and applying an F-K migration using a velocity of 0.16 m/ns. The velocity was estimated using a hyperbola fit over the bone diffraction. Migration is a valuable processing method because it collapses the diffractions back to their correct position below the surface (Yilmaz and Doherty, 2001). This is an important consideration if using GPR to locate buried features or artifacts prior to excavating. GPR image vertical axes were converted from time to depth using a velocity of 0.16 m/ns.

The bone layer is well defined between 60 and 80 cm below the surface, which is consistent with the experiment's design. The horizontal extent of the bone layer is also similar to the experiment's design. The GPR data indicate a total length of approximately 40 cm for the bone layer, which is fairly close to the actual length of the bone bed of 50 cm. The amplitude strength of the GPR reflection weakens at the edges of the bone layer, particularly on the right side. This weakened amplitude effect on the edges may be attributed to the density of the bone layer. Finally, the RMS (root mean square) amplitude is used as a measure of the energy reflected from a target and it was calculated across the bone bed (refer to Figure 4.3 for the RMS window outline). The RMS amplitude over the bone layer is 392 mV.

4.2.2 Experiment 2: Single bison bone

The single bison bone burial experiment is shown in Figures 4.3b and 4.3c. Figure 4.3b shows GPR data collected using the 1 GHz frequency and figure 4.3c shows GPR data collected using the 500 MHz frequency. Processing steps for the 1 GHz frequency data are the same as described in experiment 1. Processing steps for the 500 MHz frequency data included trimming the time window to 15 ns, setting a bandpass filter range of 250 MHz to 1 GHz, muting the direct arrival energy, and applying an F-K migration with a velocity of 0.16 m/ns.

The 1 GHz frequency successfully imaged the single buried bison bone. The top of the bone begins at 60 cm below the surface, which is consistent with the experiment design. The RMS amplitude over the 1 GHz data was 294. The 500 MHz frequency was also able to image the single buried bone. However, there are at least two other locations in the line that exhibit similar patterns as the buried bone (marked X and X' on figure 3c). This suggests that the 500

MHz antennas may not be able to adequately resolve single bone elements from surrounding heterogeneities in a field setting. Lastly, as part of this experiment, we also collected data using the 500 MHz antennas using a sampling interval of 0.2 ns and a 5 cm trace spacing. These settings are typical default parameters for acquisition of 500 MHz frequency data, but we found that they were not sufficient to image the buried bone. Dense sampling intervals are required if bone targets in the field are deeper and a lower frequency antenna is needed.

4.2.3 Experiment 3: Bone dip angle on GPR detection

The results of the tilted bison bone are shown in Figure 4.3d. GPR data were collected using a frequency of 1 GHz. Processing steps are the same as applied to the 1 GHz data from experiments 1 and 2. The 1 GHz antenna was able to detect the single bone, but there is a significant decrease in amplitude as compared to the flat-lying bone from experiment 2 (figure 4.3b). The RMS amplitude of the tilted bison bone is 139. This is a 53% decrease in amplitude as compared to the flat-lying bone and illustrates a unique consideration when interpreting GPR data. It is not uncommon for animal bone to be found buried at an angle. This is usually a result of surface topography at the time of burial or the effect of bioturbation after burial (see Balek, 2002).

4.2.4 Experiment 4: Weathering effects on GPR detection

Figure 4.4 shows the GPR results of the buried modern bison bone in good condition compared to the buried modern bison bone that exhibited higher degrees of weathering (see Figure 4.5 for a photo comparison of the two bone samples). The two samples were similar in

overall size and dimensions. The modern bone in good condition is 35 cm long with a 16 cm circumference in the middle of the bone. The modern weathered bone is 28 cm long with an 18.5 cm circumference in the middle of the bone. The degree of weathering would be classified as a stage 2 degree of weathering, with both linear and mosaic patterns of cracking at the bone surface (Behrensmeyer, 1978; Hill, 1980). The modern weathered sample also had a 25% decrease in weight in comparison and crumbled when handled. GPR data were collected using a frequency of 1 GHz. Processing steps are the same as applied to the 1 GHz data from experiments 2 and 3. Pre-migrated results are shown (figure 4a) for additional comparisons to numerical models in the next section.

The GPR data reveal that the increased weathering adversely affects the GPR amplitude response. For comparison, the RMS amplitude of the bone sample in good condition is 309 and 194 for the weathered bone sample. This difference represents a 37% decrease in amplitude. The modern bone sample in good condition also exhibits strong reverberations beneath it in the unmigrated data, whereas any reverberations beneath the weathered sample were diminished.

Figure 4.6 shows the numerical models that simulated experiments 1 and 2. The unmigrated data are shown for each comparison. The minor time differences between the numerical model and the GPR data are due to the signal adjustment in the processing steps. Overall, the 1 GHz numerical models are consistent with the GPR data for both experiments. The bison-bone layer does show additional reverberations between the top and bottom of the bone layer, whereas the model only shows the reflection between the top and bottom of the layer.

The 500 MHz frequency model predicts a stronger reflection event than what is recorded by the GPR in the sandbox, but both do detect the bone target. The decreased resolution between

the 1 GHz frequency and 500 MHz frequency is also apparent. An important consideration when comparing modeled results to actual GPR data is the influence of heterogeneities that are introduced during data collection. Model simulations assume a homogenous depositional setting and therefore show the best possible solution, whereas the actual sandbox data shows more clutter across the line. This clutter is introduced by background heterogeneities that scatter the GPR signal.

Based on these results, two additional models were run to predict the detection capabilities of GPR in different depositional settings (see Table 4.2 for model settings). The first model evaluated GPR detection capabilities based on increasing weathering stages of dry buried bison bone (Figure 4.7). This model incorporated the percentage of change observed in the amplitudes in the GPR data from experiment 4 to predict expected relative permittivity values of dry bison bone at different stages of weathering.

The second model evaluated GPR detection capabilities based on increasing dip angle of the buried bone (Figure 4.8). This model changes the bone dip angle degree from 0° - 60° in both a sandy sediment and a clay-rich sediment. For both sediment types, there is an overall decrease in peak amplitude as the dip angle increases, but at different rates. The clay-rich sediment shows a doubling in percentage of decrease from 0° - 45°, but then a slight gain in amplitude of 10% from the 45° - 60° dip angle. At a 15° dip in the sandy sediment, the model predicts only a 4% decrease in peak amplitude of the bone reflection signal strength. However, the amplitude does begin to decrease at a faster rate at higher angles in the sandy sediment. The model predicts a 42% decrease in peak amplitude for a 30° dip, a 63% decrease in peak amplitude for a 45° dip, and a 72% decrease in peak amplitude for a 60° dip.

4.3 Discussion

Overall, GPR worked well at imaging the buried bison bone layer and single bison bone burial at the frequency of 1 GHz. For the bison bone layer, there are weaker amplitudes along the edges of the bone layer. This may be attributed to the density of the bone layer and could be a useful analysis tool for finding the edges of a bone bed. Both the bone layer and single bone were detected at the correct depths, and it accurately resolved their dimensions. However, the limited depth penetration of this high frequency must be considered when evaluating these results. The results presented here were all less than a meter in depth, and in an ideal sediment for GPR investigations. Site depth of burial can be highly variable depending on age of the site and depositional settings. The 1 GHz frequency loses signal strength at depth because the electromagnetic energy dissipates into heat as it travels (Annan, 2005). Attenuation of the signal also increases if the sediments that contain the buried bone have higher conductivities, which is typical of finer-grained sediments such as silts or clays.

The 500 MHz frequency was also able to detect the single buried bone, but there was also other clutter present in the data that appeared similar to the bone reflection. The location of the bone is typically unknown in a field setting and it would be fairly difficult to distinguish which signature came from the buried bone and which was just clutter. The work presented here uses only one depositional setting and therefore is not representative of the many heterogeneities that can be introduced in the field. However, the size of the bone target is also an important factor. The 500 MHz frequency has longer wavelengths than the 1 GHz frequency, which decreases its resolution capabilities. If the bone target were larger (i.e. a mammoth or mastodon skull) or consisted of a layer of bones, then the 500 MHz antenna should be able to image it more distinctly from surrounding heterogeneities.

The numerical models were consistent with both of these experiments and can provide useful information for future investigations with GPR. In particular, they can help researchers establish if GPR is a suitable method for detecting buried bone based on parameters such as sediment grain size, size of target, moisture levels, and depth of burial. The models can also help predict which frequencies will be sufficient for a survey. Knowing this information in advance can help significantly when planning budgets for geophysical surveys and excavations.

The reflection amplitudes observed in the weathering model that are over 60% weathered are greatly reduced. Based on these results, it is unlikely that a buried bone that has experienced such a high degree of weathering will be detected by GPR in a sandy environment. However, the depositional environment is an important factor to consider in this situation. GPR reflection signal strength is dependent on the relative permittivity contrast between the bone and the sediment that encases it. As dry bone weathers and becomes more porous, its relative permittivity decreases. In the case of the sandbox, the weathered bone's relative permittivity had less of a contrast with the surrounding sand, resulting in decreased amplitudes. Finer-grained sediments such as silts or clays typically have higher relative permittivity values that range from 5-15 to 5-30, respectively (Davis and Annan, 1989). If weathered animal bone were encased in these sediments, a reduced relative permittivity value could actually increase the contrast between the bone and surrounding sediment, which will increase the reflection signal strength, as demonstrated in Figure 4.7. However, finer-grained sediments like silts and clays generally have higher electrical conductivity, which attenuates GPR signal. The models presented here assume low electrical conductivity values. GPR will not be able to detect bone encased in finer-grained sediments if the electrical conductivity is too high.

The increasing dip angle of the buried bone produces similar results. As seen in the GPR

data from experiment 3 above, there was a decrease in reflection amplitude of 53% at a dip angle of 30°. The numerical models are consistent with those results for both depositional settings and show that a further increase in dip angle continues to substantially weaken the reflection amplitude. Even in ideal depositional settings, a buried bone that is dipping more than 30° may not be possible to image with GPR.

4.4 Conclusions

Overall, GPR has proven to be an effective method for imaging buried animal bones. There are a variety of depositional settings that can affect the detection capability of GPR for imaging buried animal remains though, including size and shape, depth of burial, weathering state, and dip angle of the buried bone. Bone size and depth of burial are the most important factors to consider when using GPR. GPR will probably not succeed in imaging bones that are fragmented into small pieces or buried at great depths (>2 meters), except in very unique settings. Depositional setting is also an equally important factor to consider. Bone that is buried in finer-grained sediments such clays may actually have a greater contrast in electrical properties, but may not be detected by GPR due to an increase in attenuation of the radar signal. Finally, increased weathering of the buried bone and/or an increase in dip angle will also affect the detection capability of GPR.

References

Annan, A.P., 2005, Ground-penetrating radar, *in* Butler, D. K. ed., Near-Surface Geophysics: Society of Exploration Geophysicists, 357-434.

Balek, C., 2002, Buried artifacts in stable upland sites and the role of bioturbation: a review: Geoarchaeology: An International Journal, v. 17, 41-51.

Behrensmeyer, A.K., 1978, Taphonomic and ecologic information from bone weathering: Paleobiology, v. 4**,** 150-162.

Bitri, A. and Grandjean, G., 1998, Frequency-wavenumber modelling and migration of 2D GPR data in moderately heterogeneous dispersive media: Geophysical Prospecting, v. 46, 287-301.

Davis, J.L., and Annan, A. P., 1989, Ground-penetrating radar for high-resolution mapping of soil and rock stratigraphy: Geophysical Prospecting, v. 37, 531-551.

Hedges, R.E.M. and Millard, A.R., 1995, Measurements and relationships of diagenetic alteration of bone from three archaeological sites: Journal of Archaeological Science, v. 22, 201-209.

Hill, A.P., 1980, Early postmortem damage to the remains of some contemporary east African mammals *in* Behrensmeyer, A.K. and Hill, A.P. eds., Fossils in the Making: Vertebrate Taphonomy and Paleoecology: University of Chicago Press, 131-152.

Irving, J. and Knight, R., 2006, Numerical modeling of ground-penetrating radar in 2-D using MATLAB: Computers and Geosciences, v. 32, 1247-1258.

Tzanis, A., 2010, MATGPR Release 2: A freeware MATLAB® package for the analysis & interpretation of common & single offset GPR data: FastTIMES, v. 15, 17-43.

Yilmaz, O., 2001, Migration, *in* Doherty, S.M. Ed., Seismic data analysis: processing, inversion, and interpretation of seismic data: Society of Exploration Geophysicists, p. 463-654.

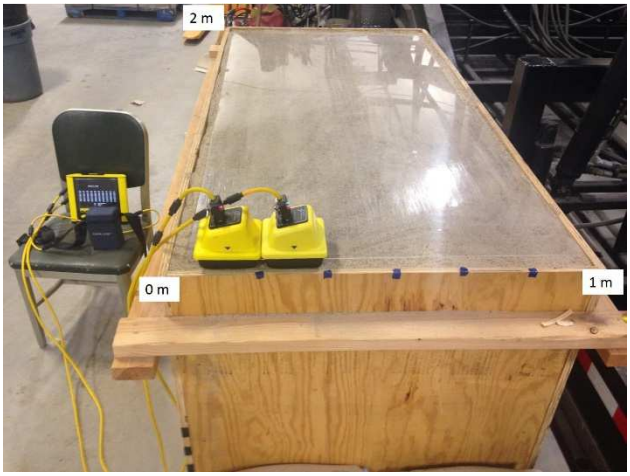

Figure 4.1: Photo of the sandbox used for the controlled GPR experiments. GPR lines were run parallel to the long axis of the box.

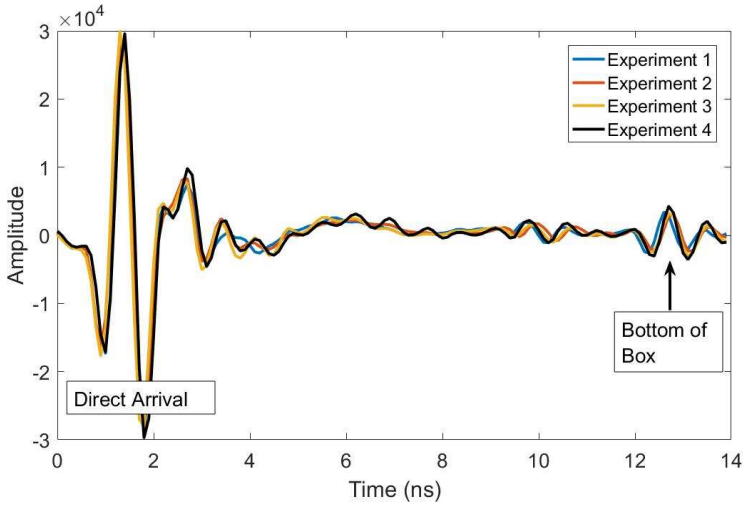

Figure 4.2: GPR waveform comparisons between the four experiments. All four experiments are at a signal frequency of 1 GHz.

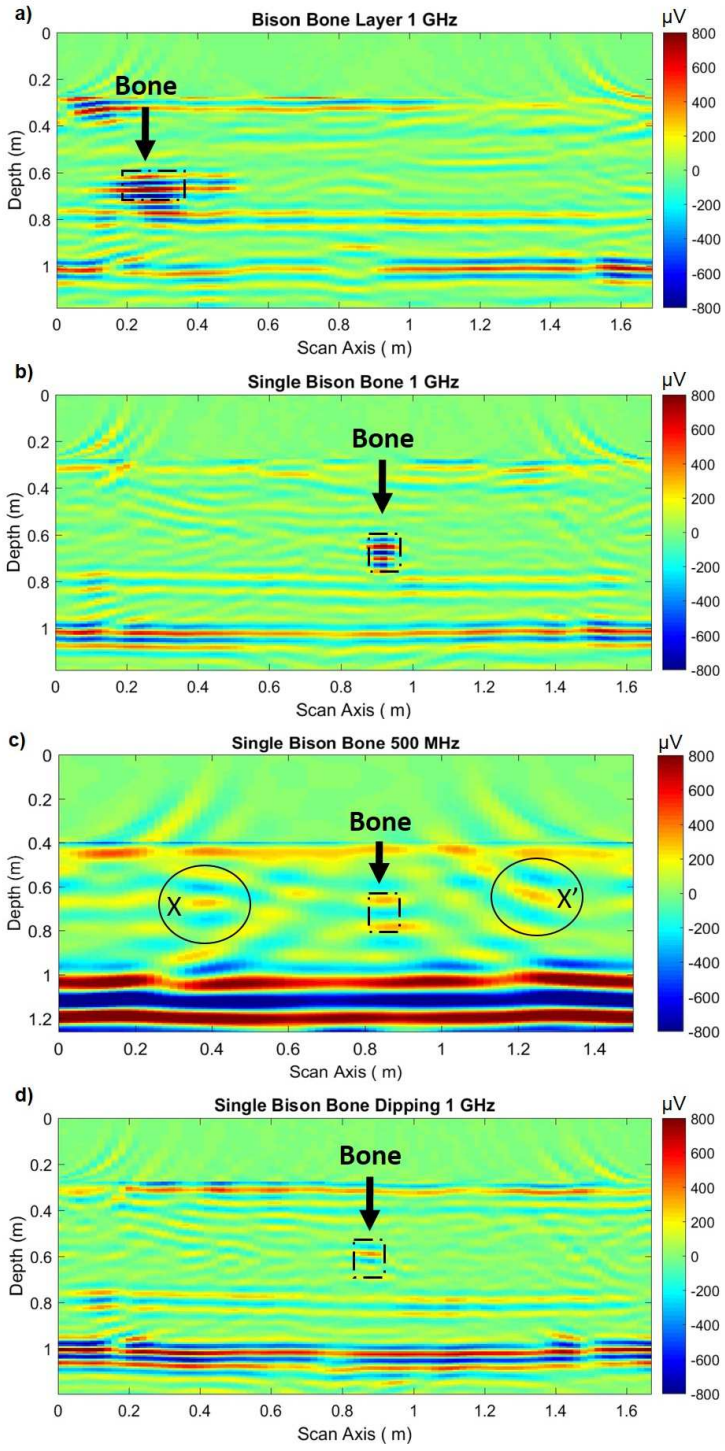

Figure 4.3: GPR sandbox profiles for the a) bison bone layer, b) single bison bone at a frequency of 1 GHz, c) single bison at a frequency of 500 MHz, and d) single bison bone inclined at a 30 degree angle. Each line shown was collected at the 45 cm mark across the Y-axis of the box. The black boxes represent the boundaries used for the RMS amplitude extraction.

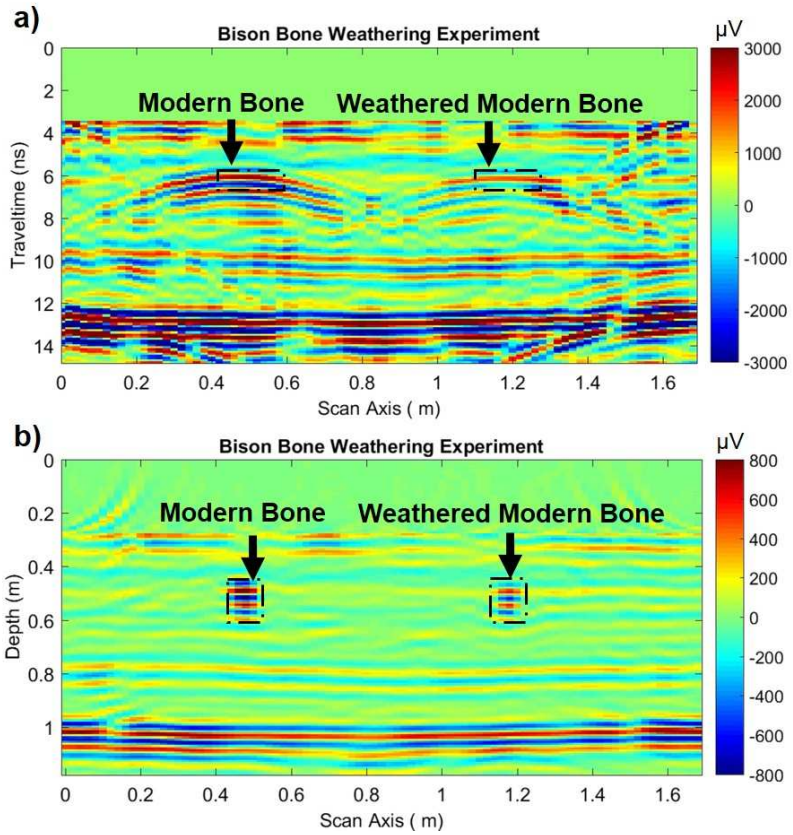

Figure 4.4: GPR results for experiment 4 comparing the effects of weathering on modern bison bone samples. Each line shown was collected at the 45 cm mark across the Y-axis of the box. The pre-migrated data is shown in (a), and the post-migrated data is shown in (b). The black boxes represent the boundaries used for the RMS amplitude extraction.

Figure 4.5: Photo comparison of the two bison bone samples used for experiment 4. The top bone sample was in good condition, whereas the bottom bone sample exhibited higher degrees of weathering. The degree of weathering would be classified as a stage 2 degree of weathering, with both linear and mosaic patterns of cracking (Behrensmeyer, 1978; Hill, 1980).

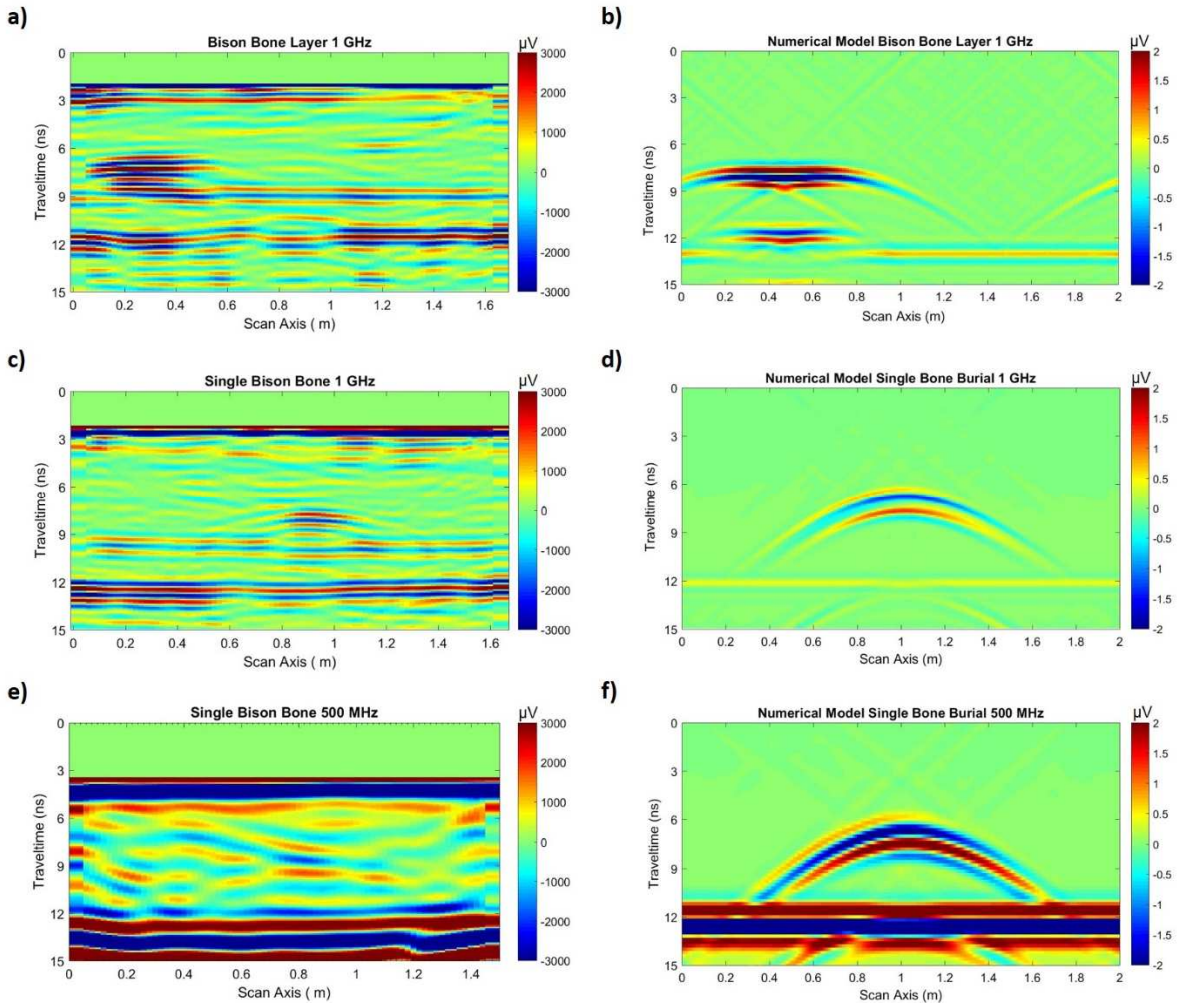

Figure 4.6: Unmigrated GPR data of the (a) bison bone layer at 1 GHz, (c) single bison bone at 1 GHz, and (e) single bison bone at 500 MHz. Corresponding numerical models are shown in (b), (d), and (f).

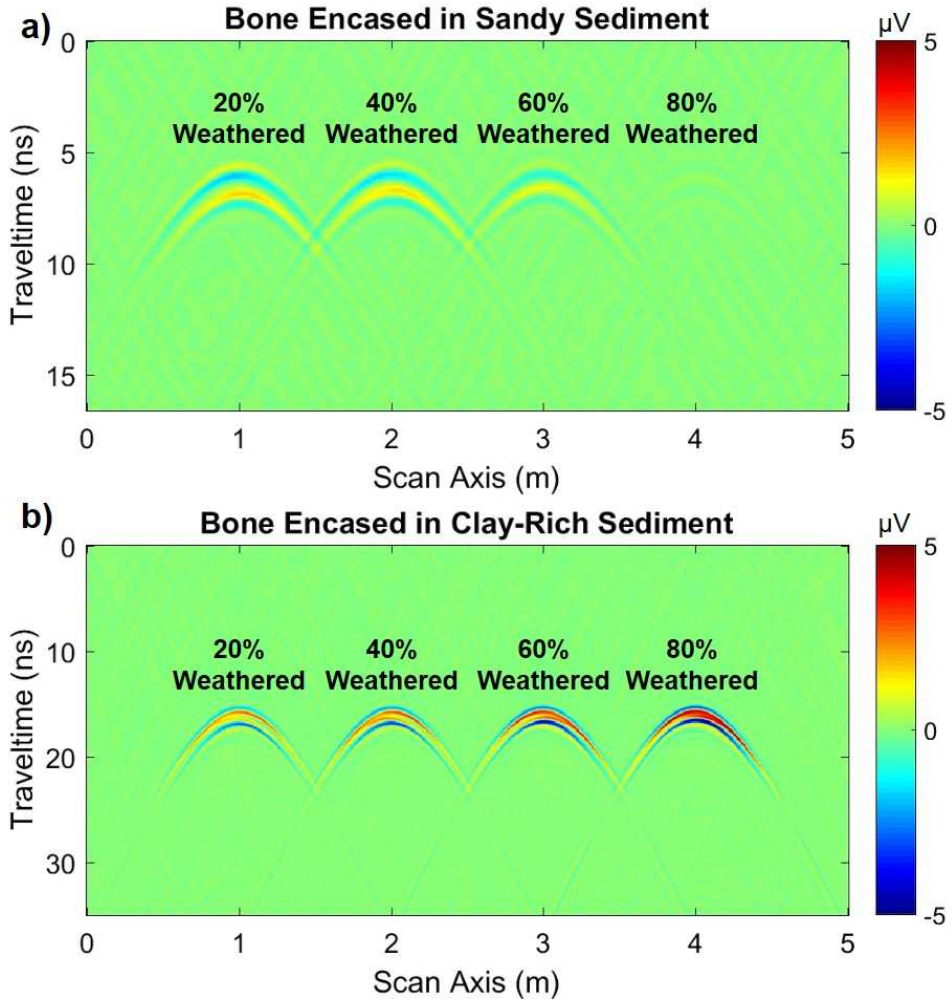

Figure 4.7: Numerical models of GPR data collected over dry buried bison bone encased in a) sandy sediment and b) clay-rich sediment at increasing levels of weathering at 1 GHz frequency.

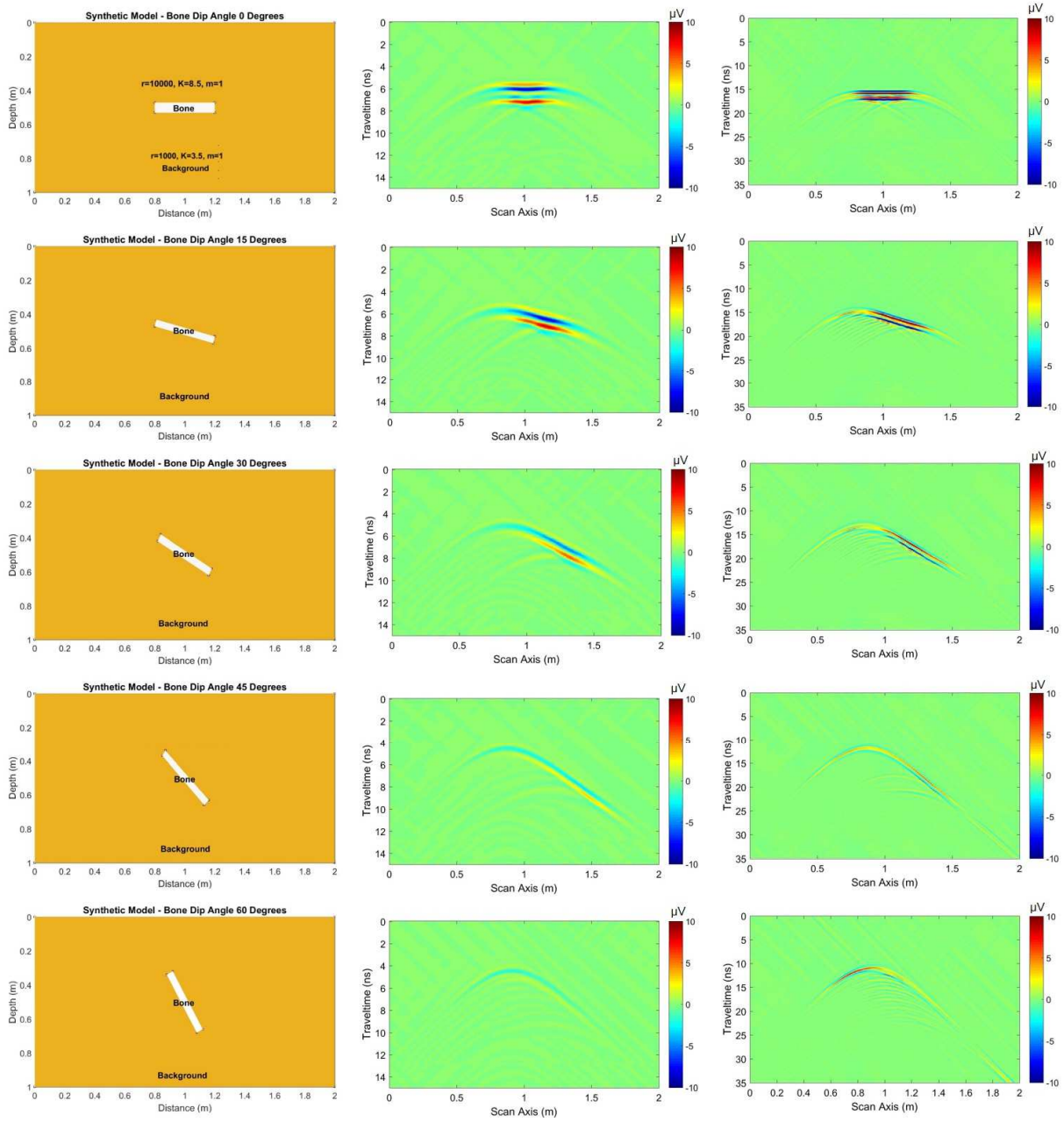

Figure 4.8: Numerical models of 1 GHz GPR data collected over a bone with increasing dip angle. The model design is on the left with corresponding data from the sandy depositional setting in the middle and the clay-rich depositional setting on the right.

Experiment 1	A bison bone layer was placed in the box at a depth of 0.6-0.8 m at 0.3-0.7 m across the x-axis. Bones were all oriented with their long axis running parallel to the long axis of the box.	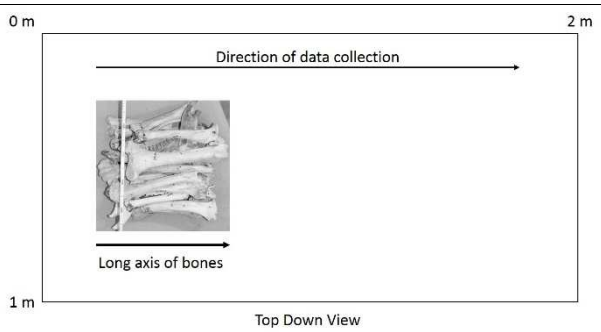
Experiment 2	A single modern bison humerus was placed flat-lying in the box at a depth of 0.6 m at 1 m across the x-axis. The long axis of the bone was oriented perpendicular to the long axis of the box. Bone is 0.41 m long with a 17-cm circumference in the middle.	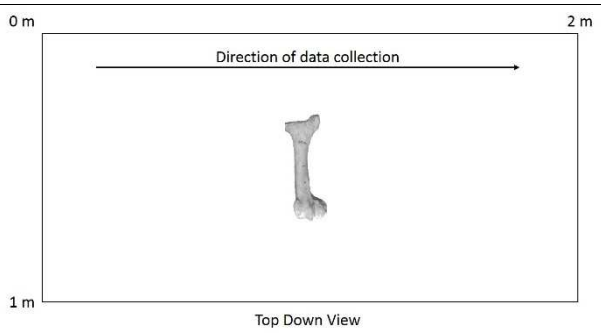
Experiment 3	A single modern bison humerus was placed at an angle of 30° in the box at a depth of 0.6 m at 1 m across the x-axis. The long axis of the bone was oriented perpendicular to the long axis of the box. Bone is 0.41 m long with a 17-cm circumference in the center.	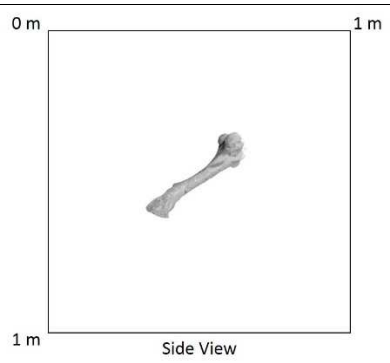
Experiment 4	A single modern bison humerus in good condition was placed flat-lying at a depth of 0.6 m at 0.6 m across the x-axis. A second modern bison humerus that exhibits significant weathering was placed flat-lying at a depth of 0.6 m at 1.4 m across the x-axis. The long axis of the bones was oriented perpendicular to the long axis of the box.	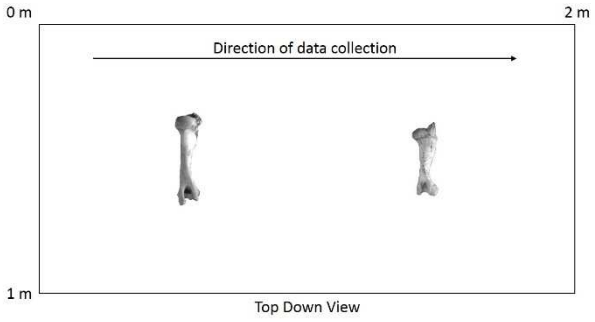

Table 4.1: Experiment design descriptions and corresponding diagrams.

Experiment	Dimensions	Location/ Depth	Frequency	Electrical Properties	Magnetic Properties
Experiment 1: Modern Bison Bone Bed	2 m long box, 1 m deep Bone layer: 0.5 m long 0.2 m thick	0.2-0.7 m along the scan axis, 0.6-0.8 m in depth	1 GHz	Sand ε_r' = 3.5 Ω•m = 1000 Bone ε_r' = 8.5 Ω•m = 10000 Concrete ε_r' = 10 Ω•m = 10000	Sand μ_r' = 1 Bone μ_r' = 1 Concrete μ_r' = 1
Experiment 2: Single Bison Bone	2 m long box, 1 m deep Single bone: 0.06 m diameter	0.5 m along the scan axis, 0.6 m in depth	500 MHz and 1 GHz	Sand ε_r' = 3.5 Ω•m = 1000 Bone ε_r'(1 GHz) = 8.5 ε_r'(500 MHz) = 9 Ω•m = 10000 Concrete ε_r' = 10 Ω•m = 10000	Sand μ_r' = 1 Bone μ_r' = 1 Concrete μ_r' = 1
Experiment 3: Increased Weathering in Bone Samples	5 m long box, 1 m deep 4 bones: 0.06 m diameter for each	1 m, 2 m, 3 m, and 4 m along the scan axis, all 0.5 m in depth	500 MHz and 1 GHz	Sand ε_r' = 3.5 Ω•m = 1000 Clay ε_r' = 25 Ω•m = 200 Bone Ω•m = 10000 ε_r'(20%) = 7.75 ε_r'(40%) = 6.5 ε_r'(60%) = 5 ε_r'(80%) = 3.35	Sand μ_r' = 1 Clay μ_r' = 1 Bone μ_r' = 1
Experiment 4: Increased dip angle of buried bone	2 m long box, 1 m deep Single bone: 0.4 m long and 0.06 m thick	1 m along the scan axis, 0.5 m in depth Dip angle ranged from 0° to 60°	1 GHz	Sand ε_r' = 3.5 Ω•m= 1000 Clay ε_r' = 25 Ω•m = 200 Bone ε_r' = 8.5 Ω•m = 10000	Sand μ_r' = 1 Clay μ_r' = 1 Bone μ_r' = 1

Table 4.2: Modeling parameters for the four experiments. ε_r' represents the relative permittivity value, Ω•m represents the electrical resistivity value, and μ_r' represents the magnetic permeability value.

Chapter 5

GPR Survey Design Effects for Imaging Buried Bone

5.0 Introduction

Survey design plays an important role in the success or failure of a GPR investigation because GPR antennas can be deployed in different orientations to optimize target detection. There are two primary considerations when designing a GPR survey: polarization and the orientation of the antenna relative to the survey line. The GPR system deployed for this research uses dipole antennas. A dipole antenna preferentially radiates linearly polarized energy in the same orientation as its long axis. Polarization effects impact the amplitude response and have been used to determine the orientation of buried objects in the subsurface. Most of this prior research has focused on buried cylinders that are assumed to be infinitely long to avoid edge effects. Animal bone, however, is not infinitely long, nor is it a perfect cylinder across the entire length of a bone.

This research investigates whether polarization can be used as a tool to interpret the orientation of buried animal bones when factors such as edge effects, irregular shape, bone weathering, and bone type are introduced. In addition, this research evaluates the difference in data quality when different antenna orientations are deployed for detecting buried animal bone. This chapter will first provide a background on GPR survey design and how different antenna orientations can affect the detection capabilities of common GPR targets. These survey design considerations are then tested and evaluated regarding the detection of buried animal bone.

5.0.1 Antenna Orientation Relative to the Survey Line

GPR antenna orientation relative to the survey line can affect data quality. There are two primary designs that the antennas can be set in for data collection: broad-side mode and end-fire mode (Figure 5.1). Both modes can be run with the antennas parallel or perpendicular relative to the survey line. GPR surveys are typically collected using the broad-side antenna orientations because they have been shown to have a higher signal-to-noise ratio than end-fire antenna orientation. This is partially attributed to the fact that data collected with antennas in end-fire mode are more susceptible to noise from buried off-survey line features (Baker and Jol, 2007).

Lutz et al. (2003) collected GPR data using 100 MHz frequency antennae over alluvial deposits at a previously investigated site in southern France to estimate the effects of antenna orientation relative to the reflectors. They show that the data collected in broad-side mode has higher amplitudes for the first 75 ns, which corresponds with the direct arrival, whereas the amplitudes are the same as the end-fire mode amplitudes afterwards. They also show that the broad-side mode reaches a higher peak frequency of 82 MHz, whereas the end-fire mode peak frequency is lower at 52 MHz. These results highlight the impact that broad-side mode versus end-fire mode can have in the field.

5.0.2 Polarization

Many commercially available GPR systems employ dipole antennas which generate linearly polarized electromagnetic waves. These electromagnetic waves have both a magnitude and direction and are described using vectors (Balanis, 1989). The direction and magnitude of these vectors will change as the electromagnetic wave propagates as a function of time (Radzevicius and Daniels, 2000). Polarization is used to describe the direction and magnitude of

these vectors at any given time and space. For GPR, the polarization of the signal measured by the receiver antenna is a function of the polarization of the signal from the transmitting antenna and scattering properties of the subsurface targets, as demonstrated in Figure 5.2 (Radzevicius and Daniels, 2000). The transmitting antenna emits an electromagnetic wave with the electric field vector parallel to its long axis. The electromagnetic wave propagates through the subsurface and a portion of the wave reflects at boundaries where there are contrasts in electrical properties. The example in figure 5.2 shows the waves reflecting off of a buried cylindrical target. Depending on the type of boundary encountered, the reflected waves can scatter, or propagate back in different directions and magnitudes, as shown. This is also known as depolarization. The change in direction or magnitude will affect the signal received by the receiving antenna because it is most sensitive to waves that are parallel to its long axis.

Previous studies have shown that GPR polarization can be utilized to help define the orientation, size, shape, and electrical properties of buried targets. Roberts and Daniels (1996) investigated GPR polarization effects created by modeling GPR polarization effects of planar interfaces and cylinders. They found that horizontal boundaries and metallic cylinders are best imaged when the buried targets are oriented parallel to the long axis of the antenna dipole, and therefore are not significant depolarizers. However, long high-EM wave cylinders (such as plastic) are significant depolarizers and are best imaged when the long axis of the cylinders are oriented perpendicular to the long axis of the antenna dipole. Finally, dipping layers are best imaged when the antennas are oriented parallel to the strike of the layer.

Radzevicius and Daniels (2000) furthered this research by modeling the polarization effects from varying cylinder diameter, composition, and the central frequency of the antennas. Their research supported the conclusions of Roberts and Daniels that metallic pipes are best

imaged when the long axis of the pipe is oriented parallel to the long axis of the antennas whereas high impedance dielectric pipes (such as plastic) are best imaged when the long axis of the pipe is oriented perpendicular to the long axis of the antennas. Results with low impedance pipes, however, are more highly dependent on their diameter and the frequency of the antenna being used. Low impedance pipes with small diameters (<1/10 the wavelength) are best imaged with the long axis of the pipe oriented parallel to the long axis of the antennas, but the polarization effect fluctuates as the ratio of pipe diameter with respect to the GPR wavelength increases. Based on these results, Radzevicius and Daniels (2000) ran additional tests that oriented the GPR transmitter and receiver perpendicular to one another (cross-polarization). They show that cross-pole antennas are highly effective at detecting pipes or other depolarizing targets of interest.

These results are further supported by van der Kruk et al. (2010) who simulated metallic and dielectric pipes using antennas that were oriented parallel and perpendicular to the long axis of the pipes. Each of the pipes had diameters of 0.2 m embedded in a homogenous sand. The dielectric pipes were evaluated at both lower and higher relative permittivity values as compared to the surrounding sand. Their results are consistent with previous research. They found that the low-permittivity pipe, at this diameter, was best imaged when the antennas were perpendicular to the long axis of the pipe. Metallic pipe and the high-permittivity pipe were best imaged when the antennas were parallel to the long axis of the pipe. The results of these previous numerical models are summarized in Table 1.

The results of these numerical models have also been tested in the field. Tsoflias et al. (2015) collected three-dimensional multipolarization time-lapse GPR data over a fluid-filled fracture at the Altona flat rock site in New York. Their results reveal that the co-polarized data is

an efficient method for fracture detection, as well as monitoring tracer flow through the fractured rock. However, the reflected signal amplitude from the fracture exhibits strong dependence on the antenna orientation, which limits additional characterizations such as how the fracture aperture changes in thickness across the site. They then show additional results that demonstrate how incorporating cross-polarized GPR data can enhance the imaging of fracture channels by capturing the preferentially scattered energy that is undetected by the co-polarized antennas. They conclude that using multi-polarization antenna orientations can greatly aid in fracture characterization and identification of flow channels in fractured rock.

Villela and Romo (2013) collected multipolarization data over a water-filled steel aqueduct pipe and an air-filled plastic barrel. Their results reveal that the steel pipe was best imaged when the antennas were oriented parallel to the strike of the pipe. The cross-polarized antennas capture some of the preferentially scattered energy when the antennas were oriented 45° to the strike of the steel pipe, but are significantly reduced when the antennas were oriented at an orthogonal angle to the strike of the pipe. The plastic air-filled barrel was imaged similarly by both the co-pole orientations, and there was a recognizable, although small, response in the cross-polarized datasets which indicates that some of the target response was depolarized.

Jol et al. (1994) collected GPR data over a modern barrier spit in Washington. Their initial results revealed an accretionary deposit of beach and upper shore-face reflections that dip towards the ocean at about 1 degree. They expanded on this work and collected additional data using various polarization designs: two varieties of cross-pole antennas and antennas parallel to one another (co-pole) in broad-side parallel and broad-side perpendicular. Their results show that the GPR data was best when the antennas were run using co-pole versus cross-pole, although the dipping reflectors were still apparent in the cross-pole data. They also reveal that, surprisingly,

the parallel broad-side outperformed the more commonly used perpendicular broad-side orientation for depth penetration and reflection continuity at deeper depths.

Lastly, Lehman et al. (2000) collected multicomponent GPR data in two field settings. The first field setting was a glaciofluvial deposit within a gravel quarry. GPR data was collected in both co-pole and cross-pole orientations to assess if reflection events that were out of the plane of the survey line could be determined. Their results show that comparing the correlation of reflection signal strength between the two cross sections can allow researchers to determine reflection events that are out of the plane of the survey line and highlights the importance of recording dual-component georadar data along isolated profiles. The second field setting was collected across a second glaciofluvial deposit and a single co-pole orientation was collected with the antennas oriented north and east across the grid. The two datasets were then summed together to remove the effects of antenna orientation dependence. Their results show that combining the two datasets allows for greater confidence in interpreting reflections.

5.1 Methodology

Similar to the setup for the experiments conducted in chapter 4, GPR data was collected over a wooden sandbox that measured 2 m long by 1 m wide and 1 m tall. The box was filled with dry, fine play sand and different targets were placed atop the surface at a depth of 0.5 m from the top of the box. The remainder of the box was then filled with more fine sand and a 2 mm thick Plexiglass sheet was placed atop to ensure a smooth surface for GPR data collection. The box sits over smooth concrete floor, which provides an additional reflector for comparison.

GPR data was collected using a Sensors and Software Pulse EKKO PRO system with 1 GHz frequency antennas. The sampling interval was set at 0.1 ns with a total time window of 25

ns and a trace spacing of 0.02 m. A total of six different antenna orientations was deployed over the course of the four experiments, including co-pole antenna pairs in both the broad-side and end-fire orientations, as well as cross-pole antenna pairs (Figure 5.3). Polarization data was collected sequentially, with all six lines completed in approximately 10 minutes, to minimize instrument drift and changes in environmental conditions. Minimal processing was completed in an effort to preserve signal amplitudes for comparison. Processing steps included time-zero adjustment, trimming the time window, and applying a bandpass filter from 500 MHz to 2 GHz for each dataset. The four experiments designs are further described in Table 5.2, and a detailed description of the individual bone measurements is described in Table 5.3.

5.2 Results

5.2.1 Experiment 1

The results of the co-pole antenna orientations are shown in Figures 5.4 and 5.5. Figure 5.4 shows the GPR inline for each orientation in the center of box, which corresponds to the center of the bone and pipe. The location of the buried bone versus buried pipe is marked and is seen at approximately 7 ns. For reference, the concrete floor reflection is located 1 m below the top at approximately 12 ns. As shown in previous studies, the pipe is clearly imaged best when the antennas are oriented parallel to the long axis of the pipe in both the broad-side and end-fire orientation. The bone specimen, however, is best imaged when the antennas are aligned perpendicular to the long axis of the bone for both broad-side and end-fire orientations. This matches the results of Radzevicius and Daniels (2000) numerical models when the diameter of the bone specimen is normalized to the wavelength.

Figure 5.5 compares the corresponding traces over the center of the bone at the four co-pole

orientations. For each corresponding trace, the RMS amplitude was calculated over one period of the bone and pipe reflection (these results are summarized in Table 5.4). The RMS amplitude of the aluminum pipe with the antennas end-fire and parallel to the long axis is 65% greater than the amplitude of the pipe with the antennas perpendicular to the long axis. The RMS amplitude of the aluminum pipe with the antennas broad-side and parallel to the long axis is 54% greater than the amplitude of the pipe with the antennas perpendicular to the long axis. The RMS amplitude of the bison bone with the antennas broad-side and perpendicular to the long axis of the bone is 46% greater than the amplitude of the bone reflection with the antennas parallel to the long axis. The RMS amplitude of the bison bone with the antennas end-fire and perpendicular to the long axis of the bone is 36% greater than the amplitude of the bone with the antennas parallel to the long axis.

To examine the possible effects of changing shape and edge effects, the GPR inlines over the ends of the bone and pipe (at 30 cm across the scan axis and 60 cm across the scan axis) were also evaluated (Figure 5.6). The predictions from previous studies indicate that antennas perpendicular to the long axis of the bones at this diameter and wavelength would best image the bone at the 30 cm inline. The predictions were correct, but surprisingly the differences in the broad-side mode were very low in comparison to the differences seen in the end-fire mode. The RMS amplitude of bison humerus in broad-side mode was only 10% greater with the antennas oriented perpendicular, whereas in end-fire mode the RMS amplitude was 24% greater. At the 60 cm inline, predictions from previous studies indicated that antennas parallel to the long axis of the bones at this diameter and wavelength would best image the bone. The predictions were once again correct for the end-fire mode, which had a RMS amplitude that was 28% higher when the antennas were parallel to the bone long axis. The RMS amplitude in broad-side mode however

were almost identical, with less than a 0.2% increase with the antennas parallel to the long axis of the bone.

As expected the pipe was best imaged with the antennas parallel to its long axis for both inlines. At 30 cm across the scan axis, the RMS amplitude of the aluminum pipe with the antennas end-fire and parallel to the long axis is 47% greater than the amplitude of the pipe with the antennas perpendicular to the long axis. The RMS amplitude of the aluminum pipe with the antennas broad-side and parallel to the long axis is 64% greater than the amplitude of the pipe with the antennas perpendicular to the long axis.

The overall amplitude scale of the entire trace was twice as high when collecting in broad-side orientation versus end-fire orientation, but this increased amplitude is concentrated in the direct arrival as the amplitude values over the bone target were similar. There was less than 10% change in the RMS amplitudes between broad-side and end-fire orientations when comparing the three inlines over the bone, with the exception of the 60 cm inline in which end-fire was 27% higher than broad-side when the antennas were parallel to the bone long axis. It can also be seen in Figure 5.5, as well as Figure 5.4b and 5.4d, that there is a longer reverberation below the bone target when the antennas are oriented parallel to the bone long axis than when they are perpendicular to the bone long axis, regardless of orientation.

Figure 5.7 shows the GPR lines for the two cross-pole antenna orientations at the 45 cm inline. As expected, the amplitude range was greatly reduced as compared to the co-pole antenna orientations. The diffraction from the buried bone target is almost undetectable next to the diffraction from the buried pipe target, but appears slightly stronger when the transmitter is oriented parallel to the orientation of the bone's long axis and the receiver is oriented perpendicular to the bone's long axis. The same RMS amplitude analysis was completed over

both subsurface targets. The aluminum pipe was consistent across both antenna orientations, with only a 5% increase in amplitude when the transmitter was oriented perpendicular to the long axis and the receiver was oriented parallel to the long axis. There is also a phase shift noted between the two antenna orientations over the pipe. The RMS amplitude analysis over the bone target showed a 58% increase in amplitude when imaged using the transmitter parallel to the bone's long axis and the receiver antenna oriented perpendicular to the bone's long axis. The bone diffraction could not be detected in either the 30 cm or the 60 cm inline when cross-pole orientations were used.

5.2.2 Experiment 2

The second experiment expands upon the results from the previous experiment by comparing broad-side and end-fire mode differences as well as polarization differences between a modern bison humerus bone in good condition versus a modern bison bone that exhibits a high degree of weathering. Figures 5.8 through 5.10 show the GPR in-line for each orientation at the 30 cm, 45 cm, and 60 cm scan line, respectively. Similar to experiment 1, the locations of the buried bones are marked and are seen at approximately 7 ns. For reference, the concrete floor reflection is located 1 m below the top at approximately 12 ns.

Less than half of the results match the polarization predictions from the numerical models presented in Radzevicius and Daniels (2000) (see Table 5.4). In general, the difference in amplitudes when comparing broad-side versus end-fire mode was on average 11%. At the 30 cm inline (Figure 5.8), the RMS amplitudes show an 18% and 30% increase respectively when the antennas are oriented perpendicular to the long axis of the modern and weathered humerus in broad-side mode. In end-fire mode, there is also a 24% increase for the weathered humerus when

the antennas are oriented perpendicular to the long axis of the bone. However, for the modern humerus there is an 18% increase in the RMS amplitude when the antennas are oriented parallel to the long axis of the bone in end-fire mode.

At the 45 cm inline (Figure 5.9), the RMS amplitudes show a 6% and 29% increase respectively when the antennas are oriented perpendicular to the long axis of the modern and weathered humerus in broad-side mode. Similarly, in end-fire mode there is also a 21% and 32% increase respectively for the modern and weathered humerus when the antennas are oriented perpendicular to the long axis of the bone. These results match the predicted numerical models for the modern humerus, but do not match the predicted results for the weathered humerus. Finally, at the 60 cm inline (Figure 5.10) the results were best when the antennas were oriented perpendicular to the long axis of both bones for both broad-side and end-fire mode, but are considerably weaker in comparison to the other lines. Surprisingly, the bones are not detected at the 60 cm inline when the antennas are oriented perpendicular to the bones long axis, regardless of broad-side or end-fire mode.

5.2.3 Experiment 3

The third experiment was completed to compare the polarization results of different types of bison bone. For this experiment, a bison rib bone in good condition and a bison metatarsal in good condition were buried in the same locations as the previous targets. These bone types are not as irregular in shape as compared to the humerus samples (Table 5.3). In fact, the rib bone is cylindrical in shape with a constant diameter across the length of the bone and the metatarsal is similar in shape to a brick. Figures 5.11 through 5.12 show the GPR inline for each orientation at the 30 cm and 45 cm scan line, respectively. The 60 cm scan line is not shown because the rib

bone was not detected, regardless of antenna mode or orientation. Similar to experiment 1 and 2, the locations of the buried bones are marked and are seen at approximately 7 ns. For reference, the concrete floor reflection is located 1 m below the top at approximately 12 ns.

The results for both the rib and metatarsal bones match the polarization predictions from the numerical models presented in Radzevicius and Daniels (2000), with the exception of the metatarsal at the 45 cm inline (see Table 5.4). In general, the difference in amplitudes when comparing broad-side versus end-fire mode was on average 12%, which is consistent with experiment 2. The rib bone was only detected by the GPR at the 45 cm inline, regardless of orientation. The RMS amplitudes over the rib bone were 32% and 31% higher when the antennas were parallel to the long axis of the bone in both broad-side and end-fire mode, respectively. Broad-side mode had higher amplitudes than end-fire mode for both antenna orientations, but by less than 10% for each.

At the 30 cm inline, the RMS amplitudes show an 55% increase in broad-side mode and a 61% increase in end-fire mode when the antennas are oriented parallel to the long axis of the metatarsal bone. Similar to the rib bone, both co-pole orientations had higher amplitudes in the broad-side mode. At the 45 cm inline, the RMS amplitudes show an 41% increase in broad-side mode and a 21% increase in end-fire mode when the antennas are oriented parallel to the long axis of the metatarsal bone. Broad-side mode had greater amplitudes than end-fire when the antennas were oriented parallel to the metatarsal long axis at the 45 cm inline. End-fire mode had greater amplitudes than broad-side when the antennas were oriented perpendicular to the metatarsal long axis at the 45 cm inline.

5.3 Discussion

Overall, this research has demonstrated that animal bone does exhibit polarization effects, regardless of bone type. Some interesting observations that arose out of this research were the complete lack of detection by the GPR, regardless of antenna orientation or mode, for certain bone types. For example, the rib bone was only detected at the very center of the bone. The slightly curved edges along the 30 cm and 60 cm inline were not detected. Both the humerus samples in experiment 2 were barely detectable or not detectable at the 60 cm inline. These bones were not as long lengthwise as the humerus used in experiment 1, and so this is most likely attributed to edge effects scattering the signal away from the receiver. Some of the bones exhibited stronger polarization effects than others as well, such as the metatarsal. This may be related to the density of the bone. The metatarsal, or foot bone, is the densest bone in the bison skeleton. Finally, the modern humerus from experiment 2 had contradicting preferred polarizations based on the antenna mode, which was not expected.

It is important to note however that these experiments only highlight the particular scenario of buried animal bone that is encased in a sediment with a lower relative permittivity values. Previous research by Radzevicius and Daniels (2000) has already demonstrated that polarization effects in this scenario are strongly dependent on the diameter of the target normalized to the dominant wavelength. The bones used here were all different sizes and this information was utilized to predict the preferred polarization based on the numerical modeling results they report. Overall, there were several inconsistencies with the preferred polarization results reported here versus these predicted preferred polarizations. This suggests that while bone diameter does play a role in the scattering properties of animal bone, the irregular shape of the bone targets is also believed to be a contributing factor. Because of this, polarization effects

would not be an effective tool, in this scenario, to try to determine the orientation of buried bone deposits prior to excavation. Conversely, numerical modeling results show that there is less dependency on the target diameter when the relative permittivity of the surrounding matrix is higher than the relative permittivity of the target. In this case, targets generally exhibit higher amplitudes when imaged with the antennas oriented perpendicular to their long axis. Future research should test animal bone buried in matrixes with higher relative permittivity values such as clays to test the polarization response.

End-fire orientations are not used as frequently in GPR studies because broad-side orientations offer better coupling when collecting data. It is still important to investigate GPR data in this orientation though, because some sites may require an end-fire orientation acquisition. This could be due to space limitations when setting up the grid, or if single borehole GPR data is being collected. For this research, we note that overall there is not a huge difference in the RMS amplitude strengths of the buried targets for both the end-fire and broad-side mode. There were several instances even where the end-fire mode exhibited higher RMS amplitude strengths than the broad-side mode. It was also observed that the higher amplitudes associated with broad-side orientation appear to be contained within the direct arrival energy only, and afterwards the amplitude levels were fairly similar. Because of this, end-fire mode may actually prove to be more beneficial in the future for archaeological investigations, as the sites are often very shallow (<1 meter below the subsurface) and the direct-arrival energy of the GPR waves can often mask shallow features.

5.4 Conclusions

Multi-polarization GPR data is an important design tool that can be used to identify the

size, shape and orientation of buried archaeological features and artifacts. Previous research has investigated how cylindrical targets like metallic and dielectric pipes are best imaged based on their diameter normalized to the wavelength and relative permittivity ratio with their surrounding medium. However, this previous research has focused primarily on numerical modelling and synthetic data with infinitely long cylinders in a homogenous background. This investigation expands on that research by investigating whether multi-polarization GPR data can be used to detect animal bone, which is a new target with added obstacles of edge effects and irregularity in the target shape. Our results show that animal bone does exhibit polarization effects. Yet, in depositional settings where the relative permittivity of the animal bone is higher than the surrounding matrix as shown here, these polarization effects are strongly dependent on the size and shape of the bone. This research shows that the irregular shape of animal bone segments does contribute to the polarization effects, which ultimately limits the potential usefulness of trying to utilize polarization effects to determine the orientation of buried animal bone for excavation planning purposes.

In addition to analyzing polarization effects, this research also compared the difference in results between broad-side and end-fire antenna modes. There was only a minor difference in the amplitudes of the buried targets between the two antenna modes. In fact, the end-fire mode had higher amplitudes than the broad-side mode for a total of 35% of the recorded surveys discussed. Future archaeological investigations, particularly for ultra-shallow sites, should consider testing the end-fire mode to see if additional information can be gained for ultra-shallow sites. The direct arrival energy is often responsible for masking shallowly buried targets, but the direct arrival energy collected in end-fire mode is significantly reduced as compared to data collected in the broad-side mode.

References

Baker, G.S., Jordan, T.E. and Pardy, J., 2007, An introduction to ground penetrating radar, in: Baker, G.S. and Jol, H.M. (Eds.), Stratigraphic analysis using GPR. The Geological Society of America Special Paper 432, p. 1-18.

Balanis, C.A., 1989, Advanced engineering electromagnetics. John Wiley and Sons, New York, NY, 981 p.

Jol, H.M., Meyers, R.A., Lawton, D.C., and Smith, D.G., 1994, A detailed ground penetrating radar investigation of a coastal barrier spit, Long Beach, Washington, U.S.A.: Proceedings of the Symposium on the Application of Geophysics to Engineering and Environmental Problems, v. 1, 107-127.

Lehman, F., Boerner, D.E., Holliger, K. and Green, A.G., 2000, Multicomponent georadar data: some important implications for data acquisition and processing: Geophysics, v. 65, 1542-1552.

Lutz, P., Garambois, S., and Perroud, H., 2003, Influence of antenna configurations for GPR survey: information from polarization and amplitude versus offset measurements, *in* Bristow, C.S. and Jol, H.M., (eds.), Ground Penetrating Radar in Sediments: The Geological Society of London Special Publications, v. 211, 299-313.

Radzevicious, S.J. and Daniels, J.J., 2000, Ground penetrating radar polarization and scattering from cylinders: Journal of Applied Geophysics, v. 45, 111-125.

Roberts, R.L. and Daniels, J.J., 1996, Analysis of GPR polarization phenomena: Journal of Environmental and Engineering Geophysics, v. 1, 139-157.

Tsoflias, G.P., Perll, C., Baker, M. and Becker, M.W., 2015, Cross-polarized GPR imaging of fracture flow channeling: Journal of Earth Science, v. 26, 776-784.

van der Kruk, J., Streich, R., Grasmueck, M., 2010, Toward true-amplitude vector migration of GPR data using exact radiation patterns, *in* Miller, R.D, Bradford, J.H., Holliger, K., eds., Advances in near-surface seismology and ground-penetrating radar: Society of Exploration Geophysicists, 97-116.

Villela, A. and Romo, J.M., 2013, Invariant properties and rotation transformations of the GPR scattering matrix: Journal of Applied Geophysics, v. 90, 71-81.

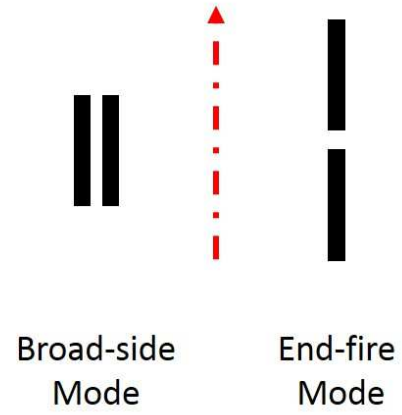

Figure 5.1: Antennas configured in broad-side mode versus end-fire mode. The red arrow represents the survey direction.

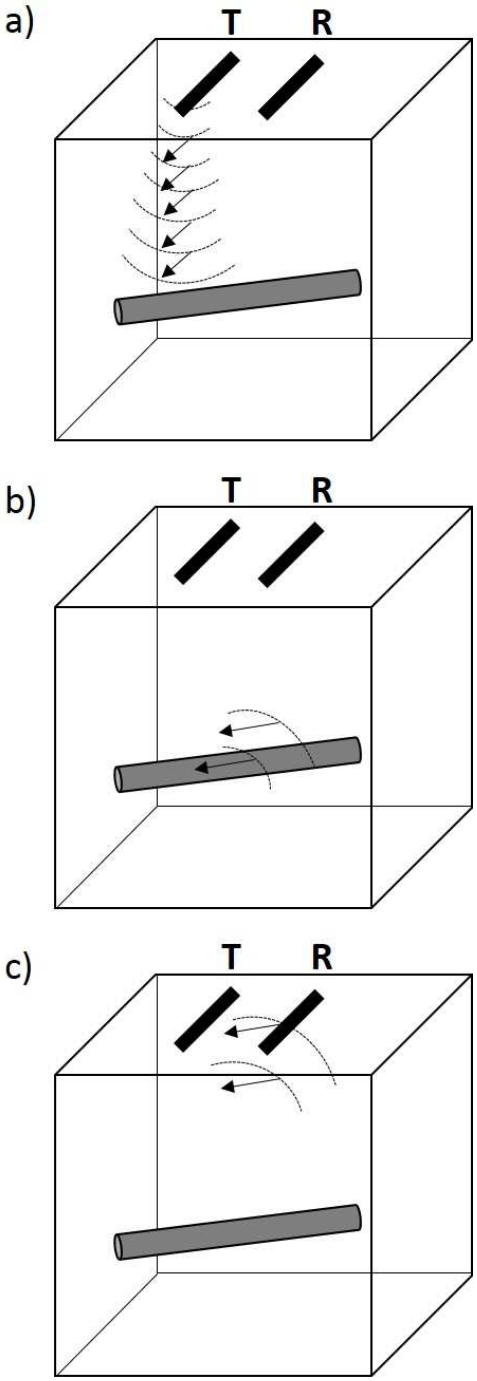

Figure 5.2: Example of a linearly polarized antenna transmitting an electromagnetic wave (a). The transmitted wave is scattered by the buried cylinder (b) and returns back to the receiving antenna in a different orientation (c). This impacts the amplitude of the received signal because the receiving antenna is most sensitive to waves that are parallel to its long axis. Figure is modified from Roberts and Daniels (1996).

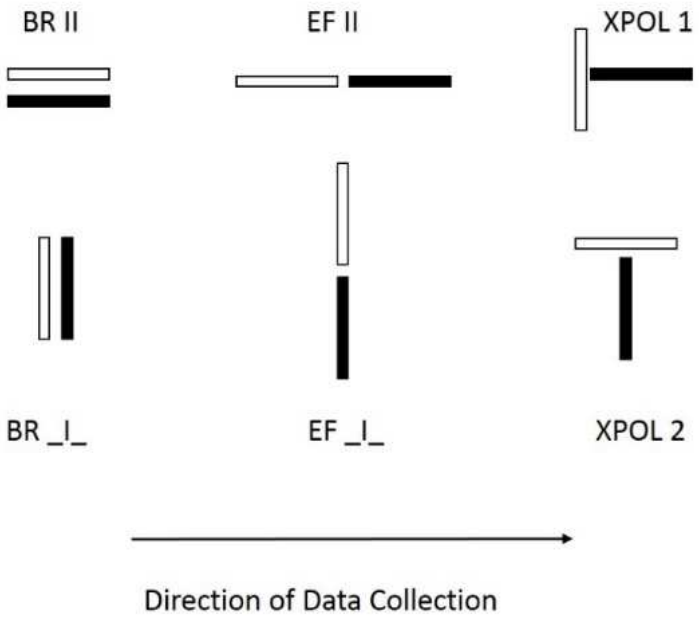

Figure 5.3: The six antenna orientations used for this experiment. BR:broad-side co-pole antenna orientation, EF:end-fire co-pole antenna orientation, and XPOL:cross-pole antenna orientation. Antennas were oriented parallel and perpendicular to the acquisition line. Transmitters are indicated by white boxes, receivers by black boxes.

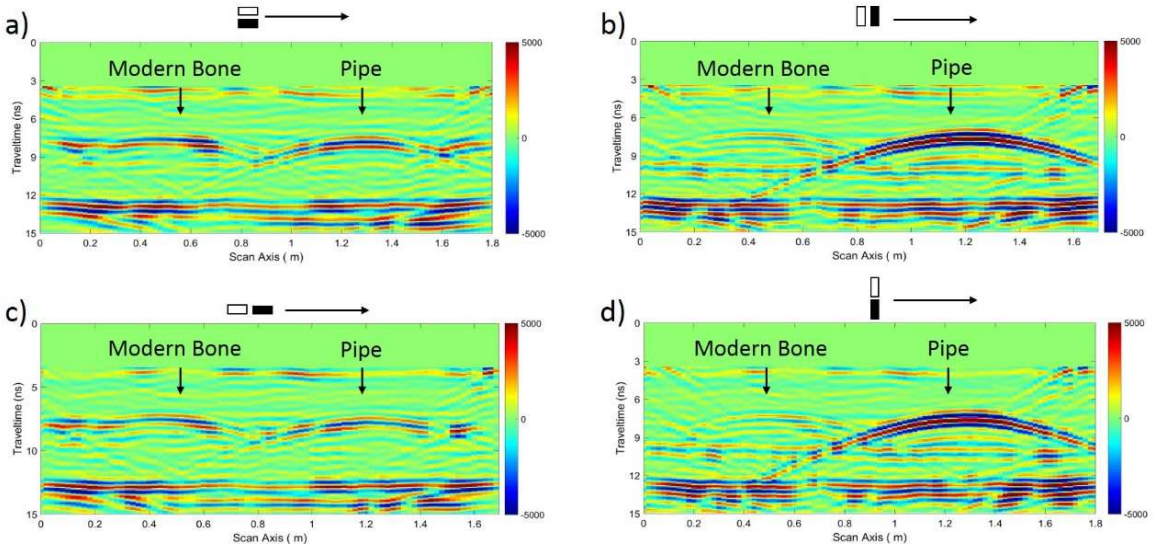

Figure 5.4: GPR inlines at 45 cm across the scan axis for the a) broad-side antennas perpendicular to the long axis of the pipe and bone, b) broad-side antennas parallel to the long axis of the pipe and bone, c) end-fire antennas perpendicular to the long axis of the pipe and bone, and d) end-fire antennas parallel to the long axis of the pipe and bone.

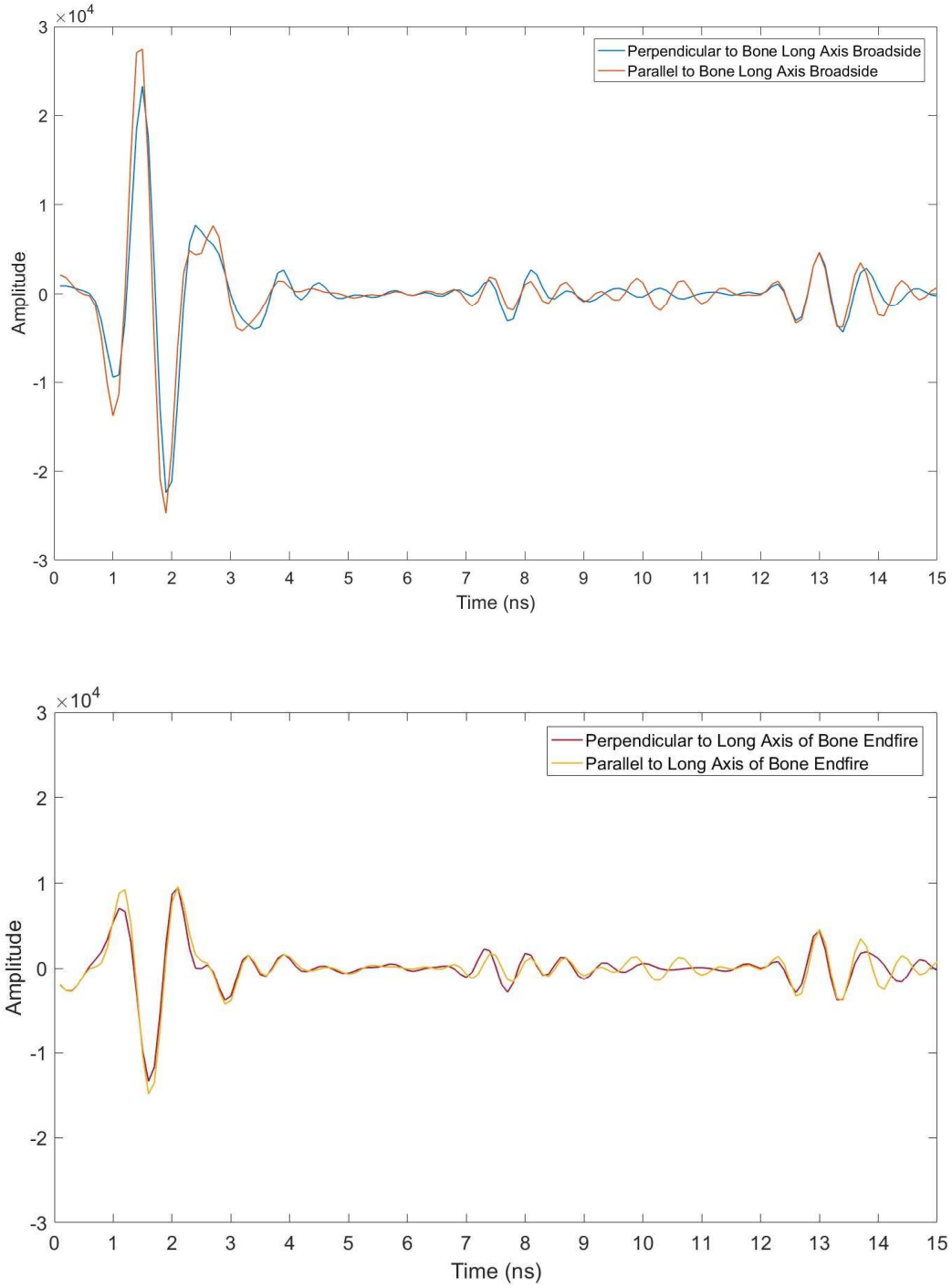

Figure 5.5: Corresponding traces over the bone target for the four co-pole antenna orientations. Broad-side co-pole orientations are on the top and end-fire co-pole orientations are on the bottom. The bone reflection is at approximately 7 ns and the concrete floor at 12 ns.

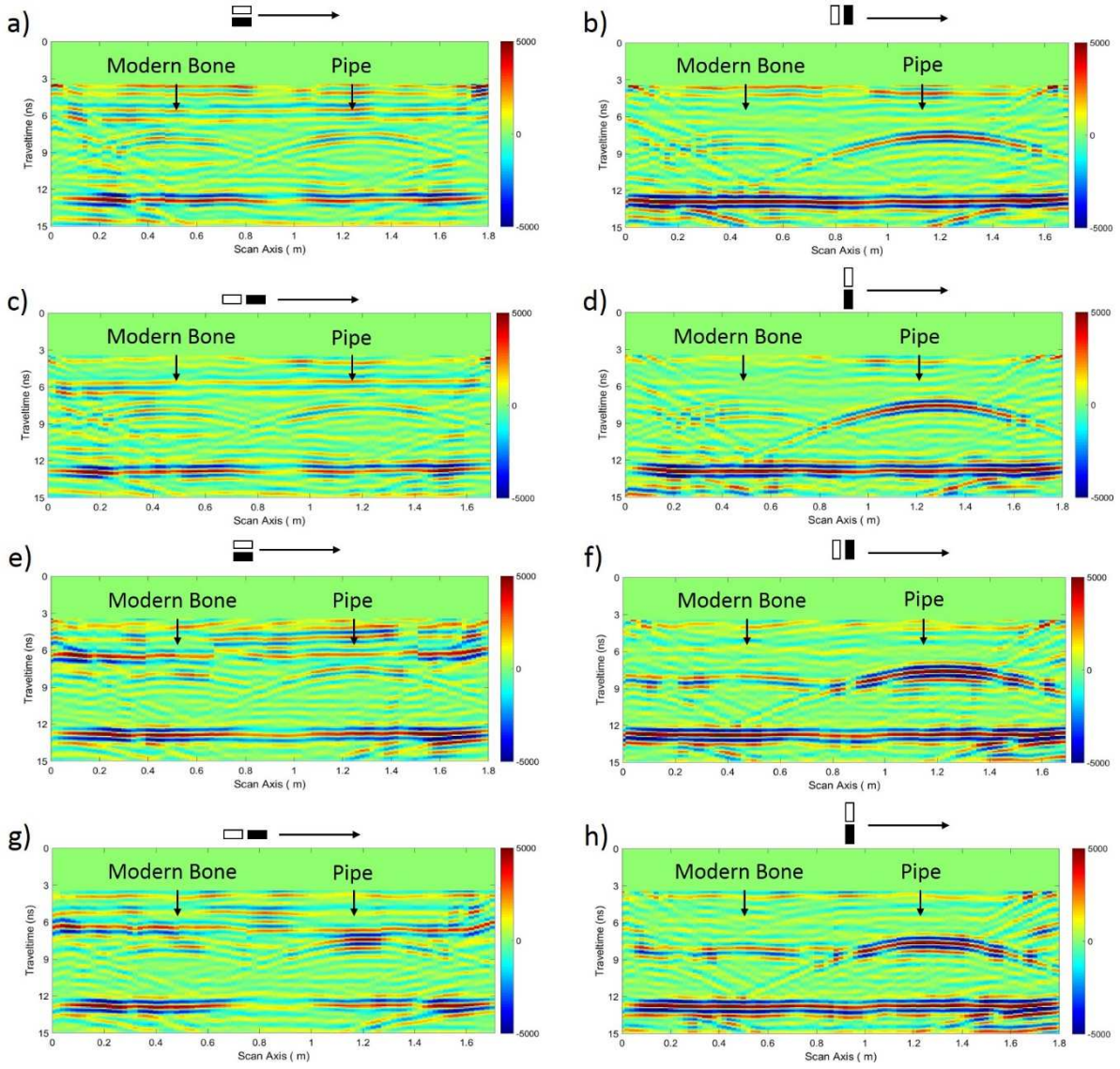

Figure 5.6: GPR inlines at 30 cm across the scan axis for the a) broad-side antennas perpendicular to the long axis of the pipe and bone, b) broad-side antennas parallel to the long axis of the pipe and bone, c) end-fire antennas perpendicular to the long axis of the pipe and bone, and d) end-fire antennas parallel to the long axis of the pipe and bone. GPR inlines at 60 cm across the scan axis for the e) broad-side antennas perpendicular to the long axis of the pipe and bone, f) broad-side antennas parallel to the long axis of the pipe and bone, g) end-fire antennas perpendicular to the long axis of the pipe and bone, and h) end-fire antennas parallel to the long axis of the pipe and bone.

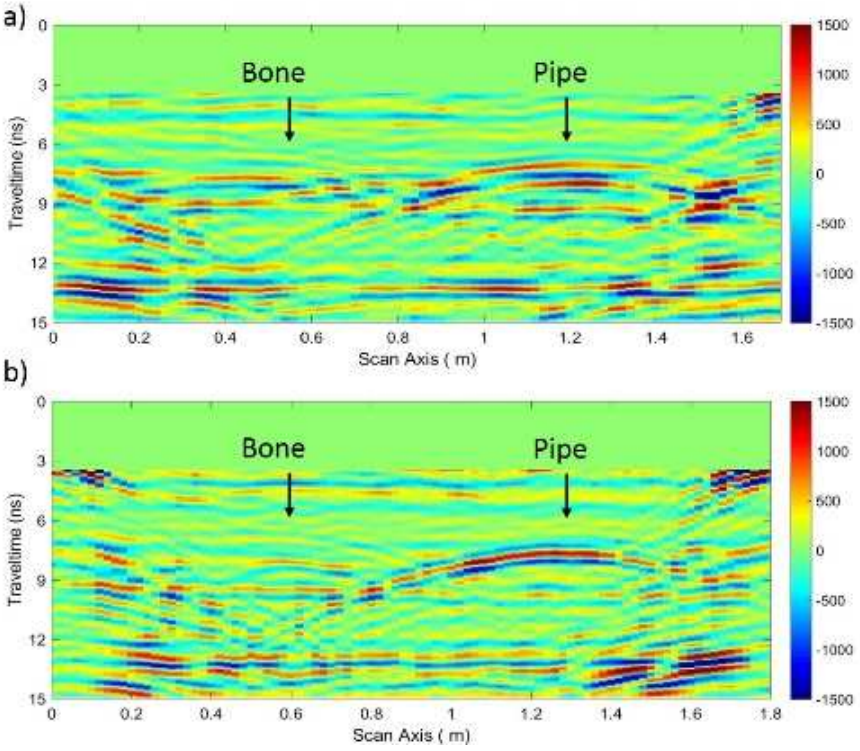

Figure 5.7: GPR inlines for the a) cross polarized antennas with transmitter parallel to the long axis of the pipe and bone and b) cross polarized antennas with transmitter perpendicular to the long axis of the bone and pipe.

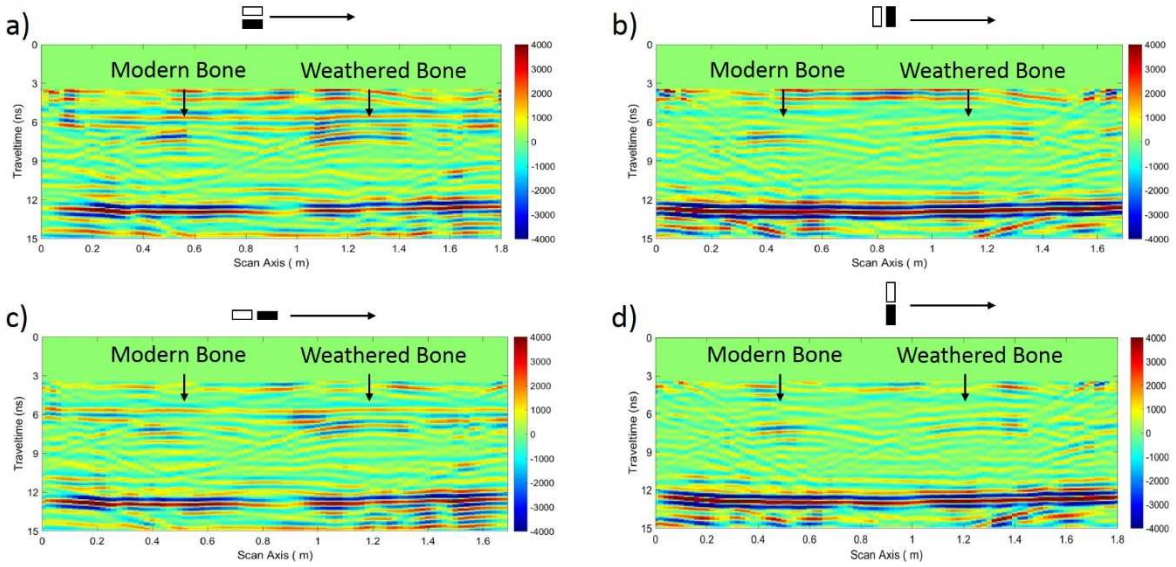

Figure 5.8: GPR inlines at 30 cm along the scan axis for the a) broad-side antennas perpendicular to the long axis of the bones b) broad-side antennas parallel to the long axis of the bones, c) end-fire antennas perpendicular to the long axis of the bones, and d) end-fire antennas parallel to the long axis of the bones.

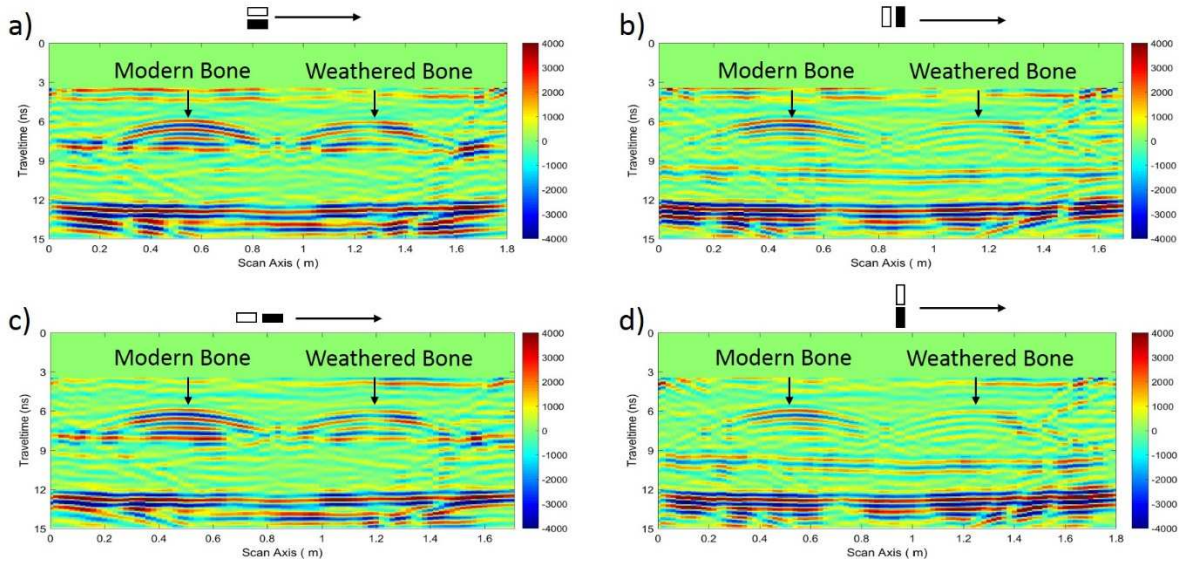

Figure 5.9: GPR inlines at 45 cm along the scan axis for the a) broad-side antennas perpendicular to the long axis of the bones b) broad-side antennas parallel to the long axis of the bones, c) end-fire antennas perpendicular to the long axis of the bones, and d) end-fire antennas parallel to the long axis of the bones.

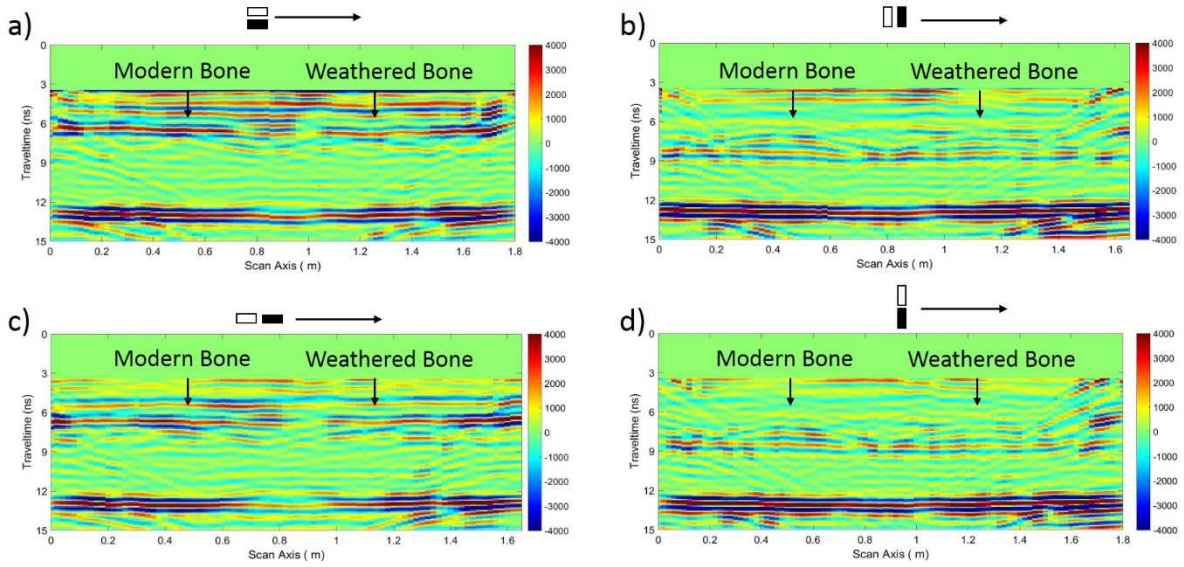

Figure 5.10: GPR inlines at 60 cm along the scan axis for the a) broad-side antennas perpendicular to the long axis of the bones b) broad-side antennas parallel to the long axis of the bones, c) end-fire antennas perpendicular to the long axis of the bones, and d) end-fire antennas parallel to the long axis of the bones. The bones were not detected when the antennas were oriented perpendicular to the long axis of the bones (a and c).

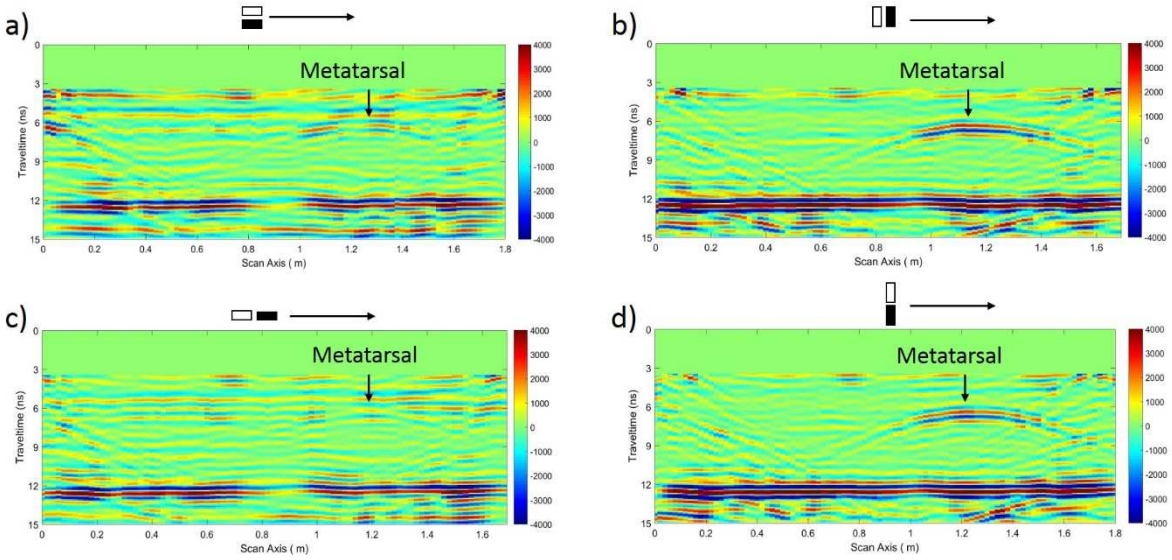

Figure 5.11: GPR inlines at 30 cm along the scan axis for the a) broad-side antennas perpendicular to the long axis of the bones b) broad-side antennas parallel to the long axis of the bones, c) end-fire antennas perpendicular to the long axis of the bones, and d) end-fire antennas parallel to the long axis of the bones. The rib bones were not detected in this inline. The metatarsal bone exhibits strong polarization effects with a clear preference for the antennas to be oriented parallel to the long axis of the bone.

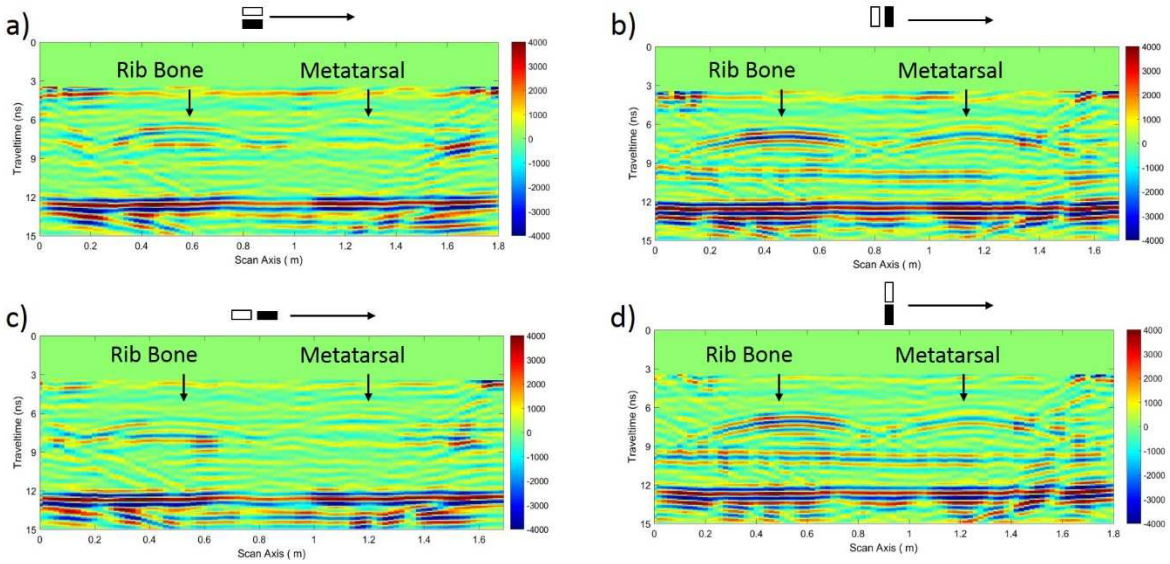

Figure 5.12: GPR inlines at 45 cm along the scan axis for the a) broad-side antennas perpendicular to the long axis of the bones b) broad-side antennas parallel to the long axis of the bones, c) end-fire antennas perpendicular to the long axis of the bones, and d) end-fire antennas parallel to the long axis of the bones. Both the rib bone and metatarsal show a clear preference for antennas parallel to the long axis of the bones.

Subsurface Target	Description
Horizontal interface	Best imaged with the T and R antennas oriented parallel to each other.
Dipping interface	Best imaged when the strike of the layer is parallel to the T and R antenna orientation.
Metallic cylinders	Best imaged when the T and R antennas are orientated parallel to the long axis of the pipe.
Small diameter (<1/10λ), dielectric pipes with permittivity higher than surrounding medium	Best imaged with the T and R antennas oriented perpendicular to the long axis of the pipe.
Dielectric pipes (diameter >1/10λ) with permittivity higher than surrounding medium	Varies depending on the diameter of the pipe and the central frequency
Dielectric pipes with permittivity lower than surrounding medium	Best imaged with the T and R antennas oriented perpendicular to the long axis of the pipe.

Table 5.2: A summary of the polarization results for various subsurface targets obtained from van der Kruk et al. (2010), Radzevicious and Daniels (2000), Roberts and Daniels (1996). T and R indicate transmitting and receiving antennas respectively.

Experiment 1	A modern bison bone humerus in good condition and an aluminum pipe were buried at a depth of 0.5 m from the top of the box. The bison bone was approximately 0.45 m long and was placed 0.6 m from the south end of the box. The aluminum pipe was 0.45 m long with a 1.8 cm diameter and was placed 0.6 m from the north end of the box.	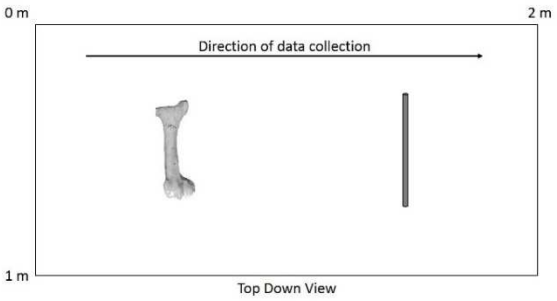
Experiment 2	A single modern bison humerus in good condition was placed flat-lying at a depth of 0.6 m at 0.6 m across the x-axis. A second modern bison humerus that exhibits significant weathering was placed flat-lying at a depth of 0.6 m at 1.4 m across the x-axis. The long axis of the bones was oriented perpendicular to the long axis of the box.	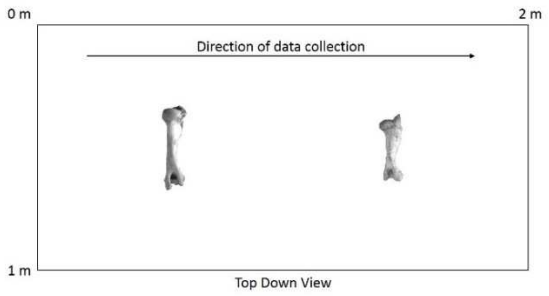
Experiment 3	A single modern bison rib bone in good condition was placed flat-lying at a depth of 0.6 m at 0.6 m across the x-axis. A second modern bison metatarsal in good condition was placed flat-lying at a depth of 0.6 m at 1.4 m across the x-axis. The long axis of the bones was oriented perpendicular to the long axis of the box.	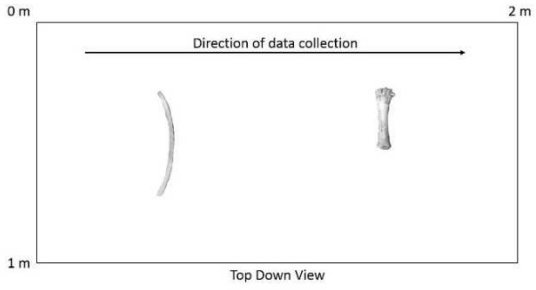

Table 5.2: Description and corresponding diagram of the three experiment designs.

	Modern Bison Humerus bone used in Experiment 1. Bone is 41 cm long with a center circumference of 17 cm. Left end of the bone has a circumference of 37 cm and the right end of the bone has a circumference of 40 cm.
	Modern Bison Humerus bone used in Experiment 2. Bone is 35 cm long with a center circumference of 16 cm. Left end of the bone has a circumference of 26.5 cm and the right end of the bone has a circumference of 34 cm.
	Modern Bison Humerus bone used in Experiment 2. Bone is 28 cm long with a center circumference of 18.5 cm. Left end of the bone has a circumference of 27.5 cm and the right end of the bone has a circumference of 29.5 cm.
	Modern Bison Rib bone used in Experiment 3. Bone is 44.5 cm long along the curve with a center circumference of 7 cm circumference across the entire length of the bone.
	Modern Bison Metatarsal bone used in Experiment 3. Bone is 25 cm long with a center circumference of 12 cm. Left end of the bone has a circumference of 17 cm and the right end of the bone has a circumference of 20 cm.

Table 5.3: Description of the length and circumference of the five bison bones used for experiments 1-3.

Type of Bone	Inline	Predicted Preferred Polarization	Preferred Polarization in Broad-side	Preferred Polarization in End-fire	End-fire vs Broad-side $A_{\parallel}$	End-fire vs Broad-side $A_{=}$
Modern Humerus from Experiment 1	30 cm	$A_{=}$	$A_{=}$ by 10%	$A_{=}$ by 24%	BS > by 3%	EF > by 10%
	45 cm	$A_{=}$	$A_{=}$ by 46%	$A_{=}$ by 36%	EF > by 7%	BS > by 9%
	60 cm	$A_{\parallel}$	$A_{\parallel}$ by <0.2%	$A_{\parallel}$ by 28%	EF > by 27%	BS > by 1%
Pipe from Experiment 1	30 cm	$A_{\parallel}$	$A_{\parallel}$ by 64%	$A_{\parallel}$ by 47%	BS > by 20%	EF > by 16%
	45 cm	$A_{\parallel}$	$A_{\parallel}$ by 54%	$A_{\parallel}$ by 65%	BS > by 5%	BS > by 28%
	60 cm	$A_{\parallel}$	$A_{\parallel}$ by 70%	$A_{\parallel}$ by 32%	BS > by 6%	EF > by 53%
Modern Humerus from Experiment 2	30 cm	$A_{\parallel}$	$A_{=}$ by 18%	$A_{\parallel}$ by 18%	EF > by 6%	BS > by 29%
	45 cm	$A_{=}$	$A_{=}$ by 6%	$A_{=}$ by 21%	BS > by 12%	EF > by 6%
	60 cm	$A_{=}$	$A_{\parallel}$	$A_{\parallel}$	EF > by 21%	No detect in $A_{=}$
Weathered Humerus from Experiment 2	30 cm	$A_{=}$	$A_{=}$ by 30%	$A_{=}$ by 24%	EF > by 1%	BS > by 7%
	45 cm	$A_{\parallel}$	$A_{=}$ by 29%	$A_{=}$ by 32%	BS > by 13%	BS > by 9%
	60 cm	$A_{=}$	$A_{\parallel}$	$A_{\parallel}$	BS > by 8%	No detect in $A_{=}$
Rib Bone from Experiment 3	45 cm	$A_{\parallel}$	$A_{\parallel}$ by 32%	$A_{\parallel}$ by 31%	BS > by 9%	BS > by 8%
Metatarsal from Experiment 3	30 cm	$A_{\parallel}$	$A_{\parallel}$ by 55%	$A_{\parallel}$ by 61%	BS > by 9%	BS > by 22%
	45 cm	$A_{=}$	$A_{\parallel}$ by 41%	$A_{\parallel}$ by 21%	BS > by 10%	EF > by 16%

Table 5.4: Summarized results of the RMS amplitude comparisons between the four co-pole antenna orientations. The symbol $A_{=}$ stands for antennas perpendicular to the long axis of the target and the symbol $A_{\parallel}$ stands for antennas parallel to the long axis of the target. Discrepancies between predicted and actual are highlighted in red.

Chapter 6
Summary and Conclusions

This research investigates the detection capabilities of ground-penetrating radar for imaging prehistoric animal bone-beds. Several topics were discussed, beginning with an in-depth analysis into the electrical properties of modern animal bone as a proxy for prehistoric animal bones. Next, numerical models and controlled sandbox GPR experiments were utilized to determine the effects of a variety of depositional settings on GPR detection capabilities of buried modern bison bone. Finally, GPR antenna survey design considerations were explored. A summary of these results is presented here.

The first half of this study reports out the electrical properties of bone (relative permittivity, loss factor, and loss tangent) in the frequency ranges of 10 MHz to 1000 MHz of four modern large fauna and one sample of prehistoric mammoth bone. The data reveal that the electrical properties are frequency-dependent, specifically the relative permittivity of bone mineral for each animal type decreases with increasing frequency, whereas loss factor and loss tangent increase with frequency. The results also show that there is a statistically significant difference in the relative permittivity values of different species of animal that is not related to the porosity, bulk density, or water saturation levels of the bone.

In addition to this analysis, three common dielectric mixing models were utilized to 1) determine what properties control the best-fit parameters of animal bone relative permittivity as well as 2) determine the relative permittivity values of dry bone mineral grain. These three models included the Topp model, the CRIM model, and the Hanai-Bruggeman model. The Topp model uses volumetric water content to predict relative permittivity values, and was matched the

measured values well. This indicates that water saturation and porosity play a role in predicting the permittivity values of animal bone. In addition, this study utilized the CRIM and Hanai-Bruggeman models to estimate the base permittivity values of bone mineral grains to fall in the range of 3-5 within the frequency ranges of 10 MHz to 1000 MHz. Overall, all three models are recommended for estimating relative permittivity values of animal bone in the future because of their overall accuracy across the entire frequency sweep and simplicity to implement.

The results of the controlled sandbox experiments, in addition to the numerical models, were very successful and prove that GPR is an effective method for imaging buried animal bones. The sandbox tests in particular reveal that there are a variety of depositional settings that can affect the detection capability of GPR for imaging buried animal remains, including size and shape, depth of burial, weathering state, and dip angle of the buried bone. When planning for an excavation, bone size and depth of burial will most likely be the most important factors to consider when using GPR. GPR will probably not succeed in imaging bones that are fragmented into small pieces or buried at great depths (>2 meters), except in unique settings. If known in advance from cores or nearby excavations, depositional setting is also an equally important factor to consider. Bone that is buried in finer-grained sediments such clays may actually have a greater contrast in electrical properties, but may not be detected by GPR due to an increase in attenuation of the radar signal. Finally, increased weathering of the buried bone and/or an increase in dip angle will also affect the detection capability of GPR. Increasing dip angle will reduce the amplitude of the bone reflection, regardless of the sediment it is buried in. Increased weathering will ultimately lower the overall permittivity of dry bone, and therefore can affect the amount of contrast between the bone and surrounding sediment.

Finally, this research investigated the effects of survey design for GPR imaging of buried

animal bone. Both antenna orientations (end-fire mode versus broad-side mode) and polarization effects were considered. Previous researchers have shown that there is a difference in the size and shape of the radiation patterns from linearly dipole antennas when they are in end-fire mode versus broad-side mode. Because of this, the assumption when designing a GPR survey has been that broad-side mode will always yield better results because it should offer better coupling when collecting data. The results from this study show that this assumption is not always true and could actually be a preventative factor when trying to image a target such as animal bone. There were several instances where the end-fire mode exhibited higher RMS amplitude values over the bone target than the broad-side mode. The results also reveal that the difference in the RMS amplitude strengths of the buried targets between the two modes was 10% or less over 60% of the time. For future investigations, it was also observed that the higher amplitudes associated with broad-side orientation appear to be contained within the direct arrival energy only, and afterwards the amplitude levels were fairly similar. Because of this, end-fire mode may prove to be more beneficial in the future for archaeological investigations, as the sites are often very shallow (<1 meter below the subsurface) and the direct-arrival energy of the GPR waves can often mask shallow features.

The polarization results show that animal bone does exhibit polarization effects. Polarization effects have been shown to be a useful tool for determining the orientation of a buried target, and could aid in the planning of an excavation. Previous researchers have demonstrated through numerical modeling that the size of the diameter of a pipe relative to the GPR wavelength and the permittivity ratio of the target relative to its surrounding matrix determine the polarization effects of the target. The results of this study show that in addition to these three factors, the irregular shape of bone targets as well as additional edge effects

contributed by their length are also contributors to the polarization effects of a buried target. Ultimately, these factors make it very difficult to use polarization effects to determine buried bone orientation prior to an excavation.

The overall results from this research demonstrate that GPR is capable of detecting prehistoric animal bone. Future research should further investigate the differences found in animal types by examining microstructure of the bones to see if that is a contributing factor. Electrical properties of human bone versus animal bone should also be investigated, as the results of this research indicate that GPR could be a promising tool for forensic investigations. In conclusion, GPR has already been highlighted in the literature as a promising tool for the archaeological community, and this research has demonstrated a new expansion for GPR's ability to assist in future investigations of archaeological sites that contain prehistoric animal bone.

Appendices

APPENDIX 1: KEYSIGHT MANUAL DATA SHEETS

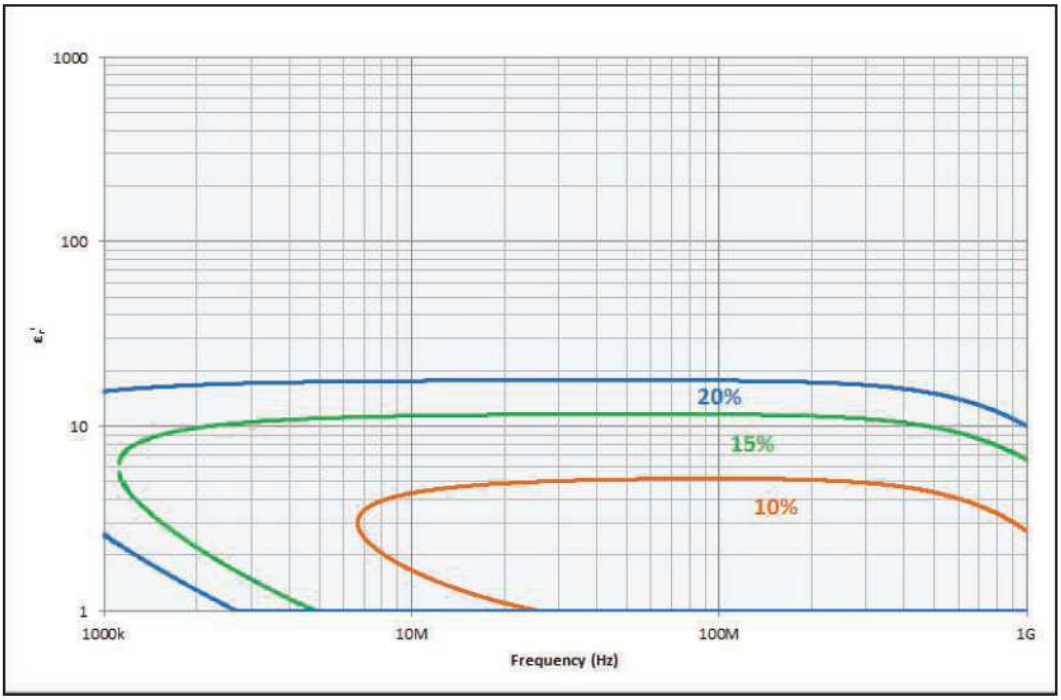

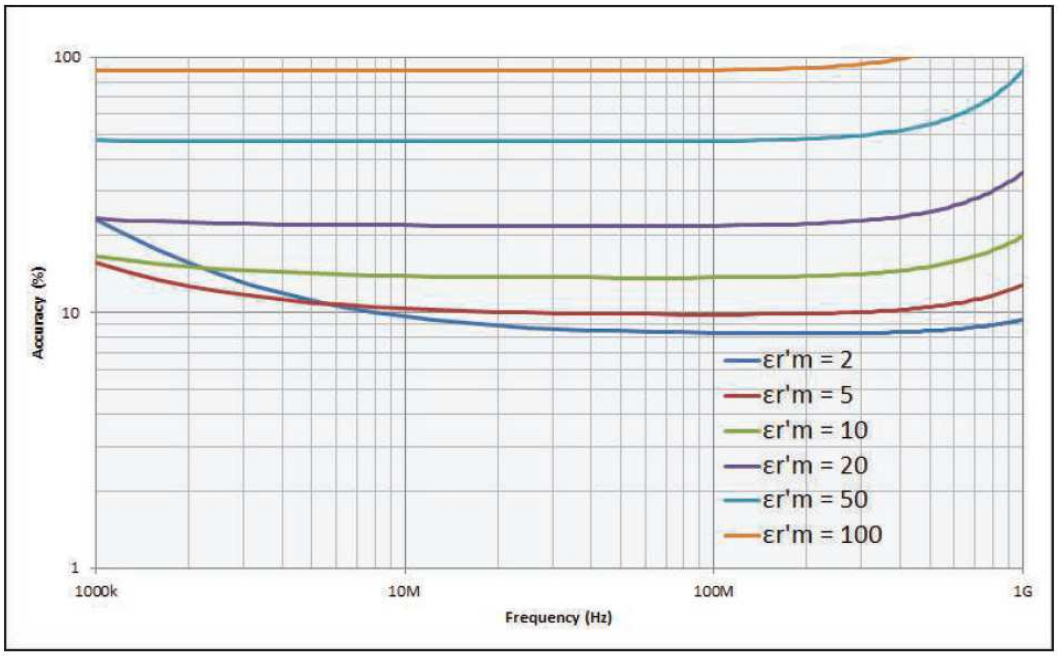

Figure A1.1: Permittivity accuracy ($\frac{\Delta\varepsilon' r}{\varepsilon' r}$) vs. frequency at t = 0.3 mm (from Keysight Technologies E4991B Impedance Analyzer Data Sheet).

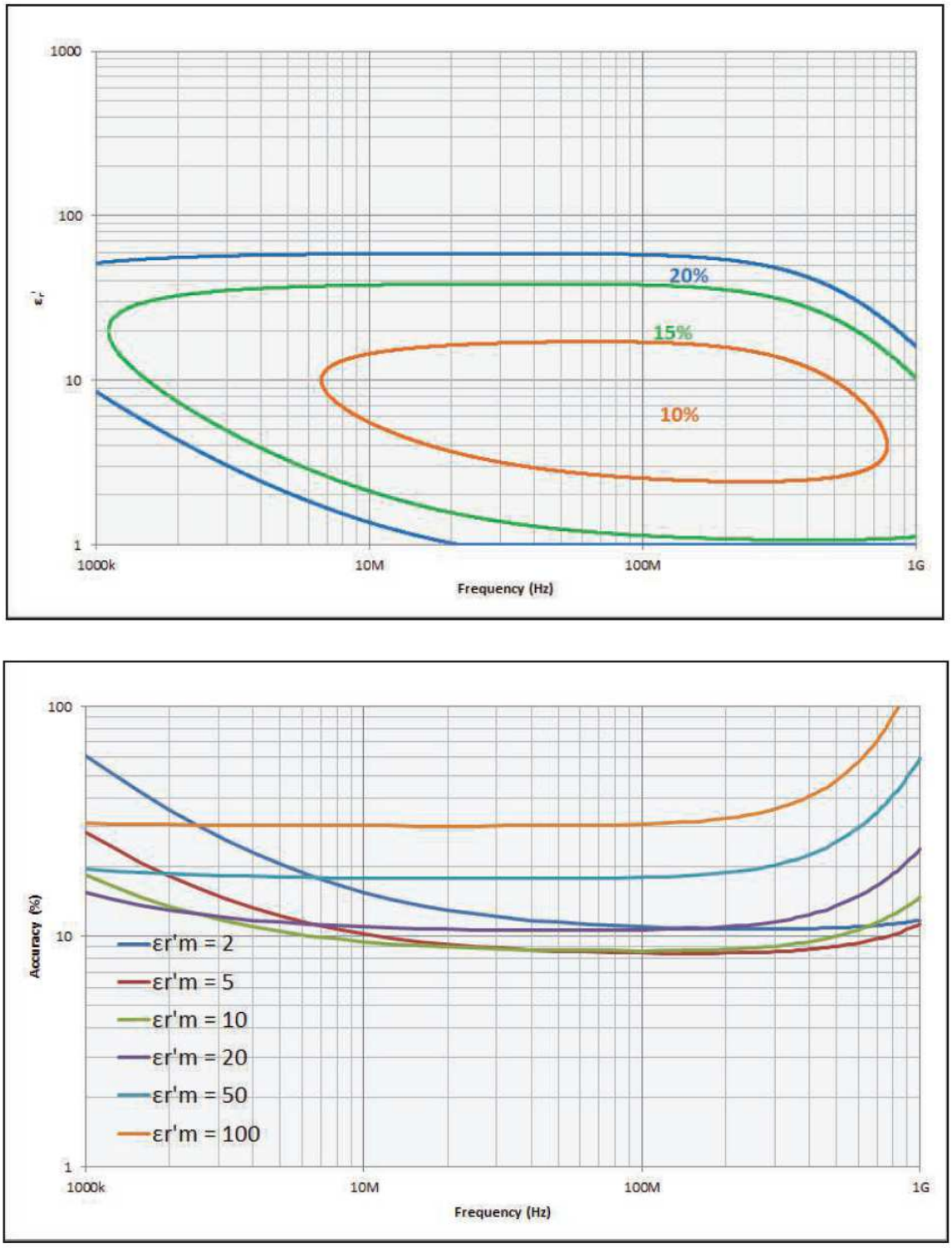

Figure A1.2: Permittivity accuracy ($\frac{\Delta\varepsilon' r}{\varepsilon' r}$) vs. frequency at t = 1 mm (from Keysight Technologies E4991B Impedance Analyzer Data Sheet).

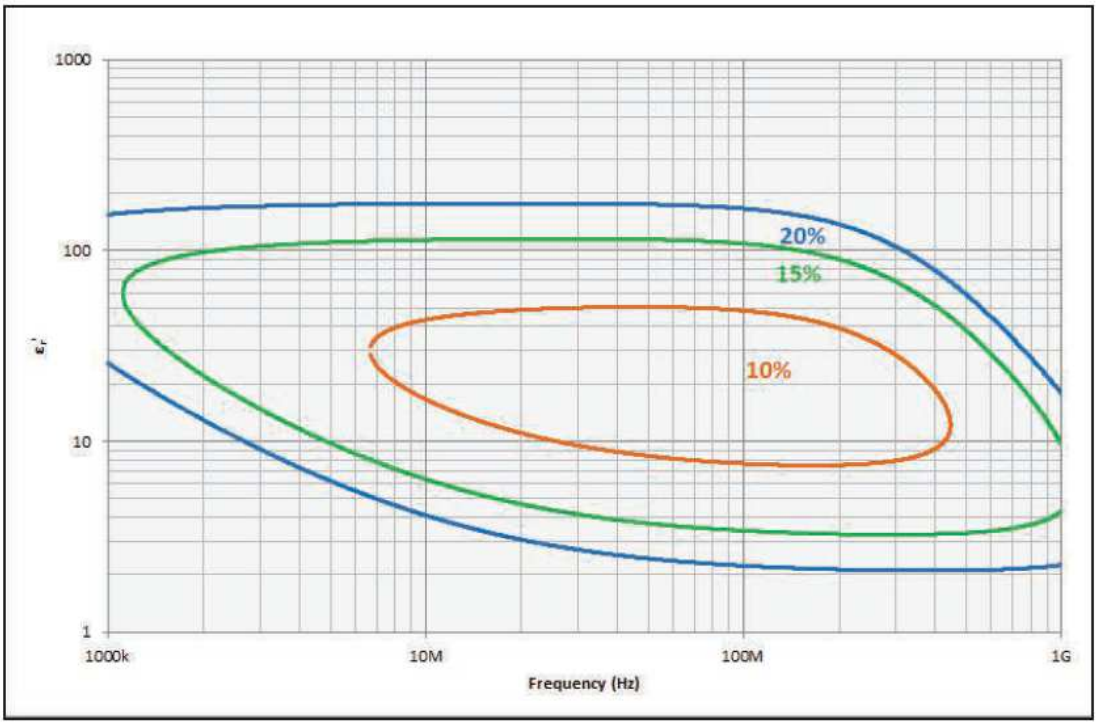

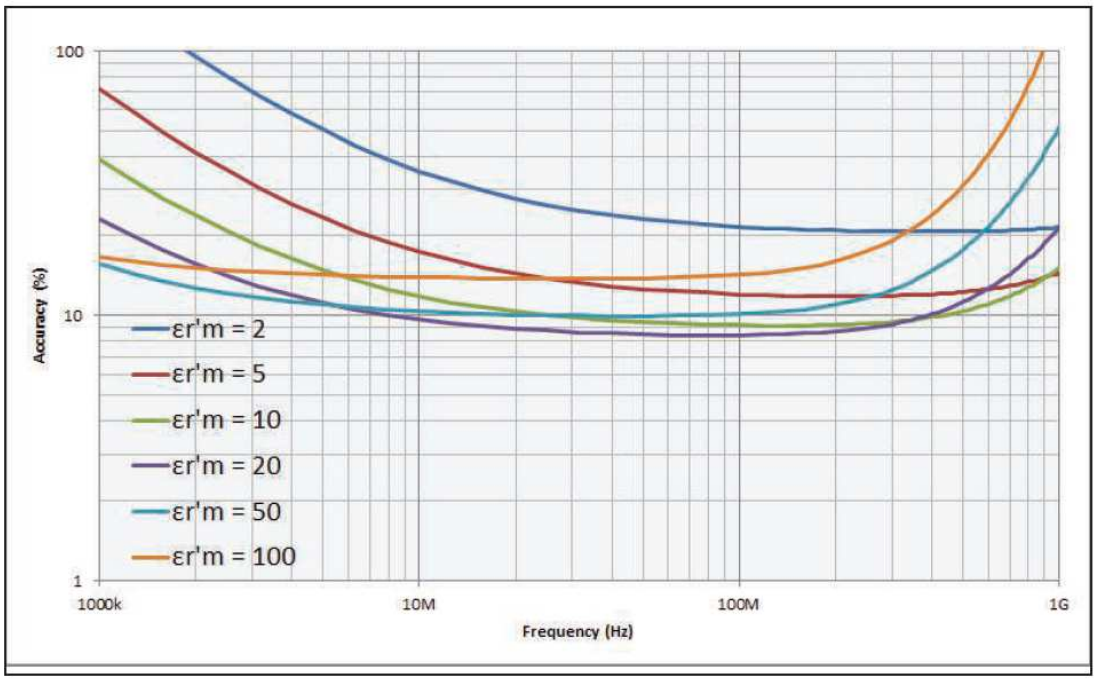

Figure A1.3: Permittivity accuracy ($\frac{\Delta\varepsilon' r}{\varepsilon' r}$) vs. frequency at t = 3 mm (from Keysight Technologies E4991B Impedance Analyzer Data Sheet).

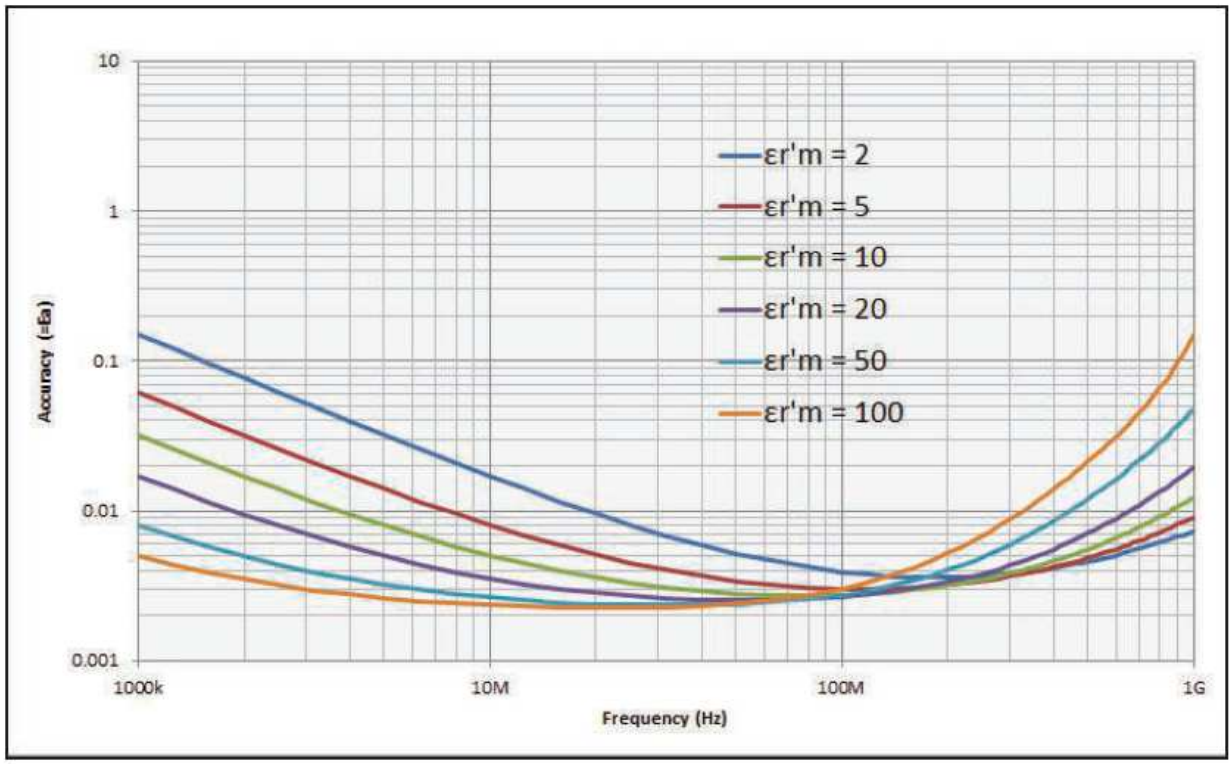

Figure A1.4: Dielectric loss tangent (tanδ) at t = 0.3 mm (from Keysight Technologies E4991B Impedance Analyzer Data Sheet).

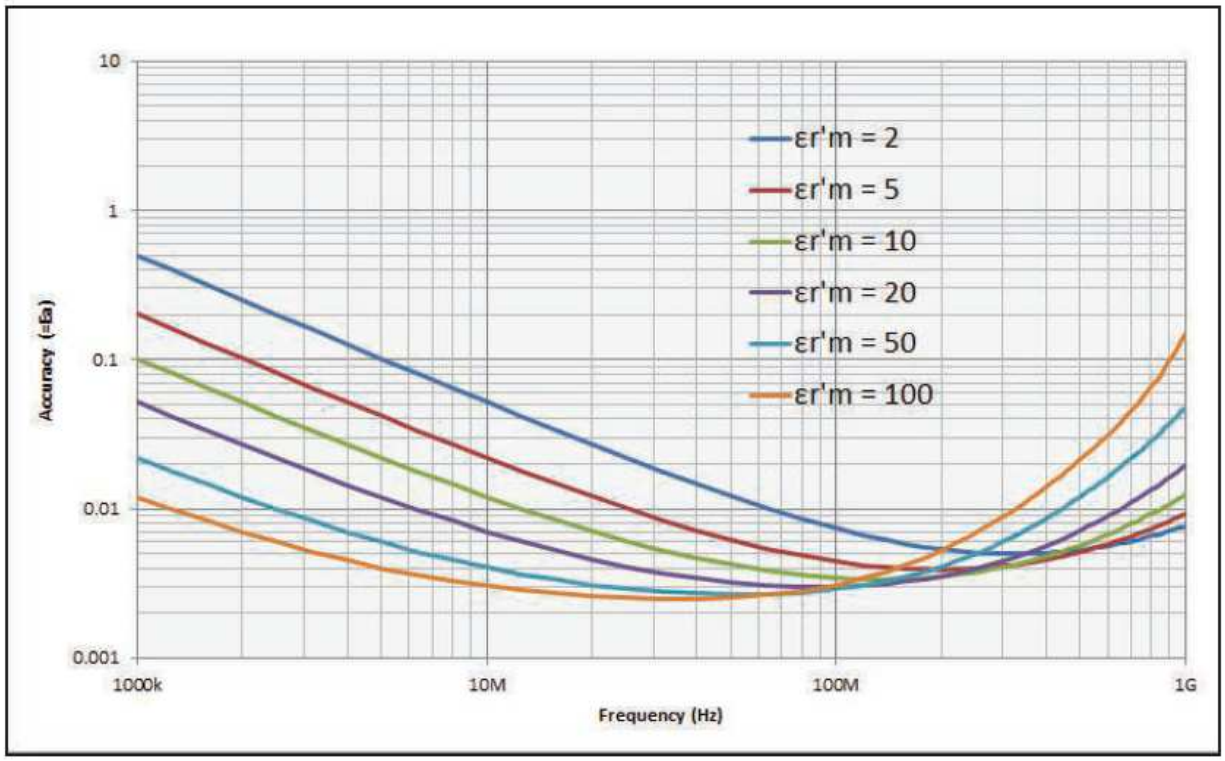

Figure A1.5: Dielectric loss tangent (tanδ) at t = 1 mm (from Keysight Technologies E4991B Impedance Analyzer Data Sheet).

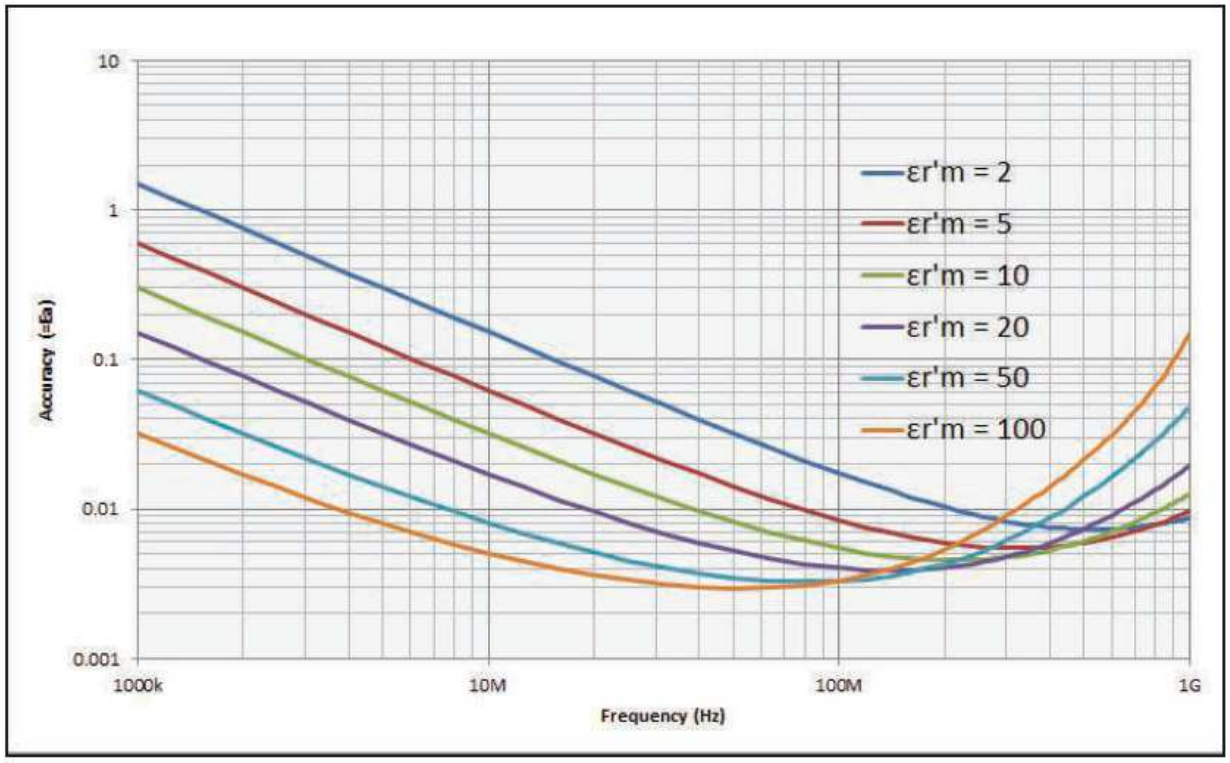

Figure A1.6: Dielectric loss tangent (tanδ) at t = 3 mm (from Keysight Technologies E4991B Impedance Analyzer Data Sheet).

APPENDIX 2: BONE THIN SECTION THICKNESS AND DIAMETER VALUES

Deer			
Bone Type	**Sample Name**	**Diameter (mm)**	**Thickness (mm)**
Left Humerus	D1	16.429 (half), 23.028 (full)	1.008
Left Humerus	D2	20.982	1.039
Right Humerus	D3	21.145 (full), 20.274 (half)	0.965
Tibia	D4	21.149	1.003
Tibia	D5	21.034 (full), 13.415 (half)	1.01
Tibia	D6	20.997	1.002
Femur	D7	21.350 (full), 18.198 (half)	1.016
Femur	D9	17.980 (half), 21.396 (full)	0.985
Metatarsal	D10	21.249	0.989
Femur	D11	21.275 (full), 16.151 (half)	0.982
Inominate?	D12	21.095	0.885
Pelvis?	D13	14.772 (half), 21.398 (full)	0.987
Scrap	D14	21.478 (full), 18.310 (half)	1.015
Scrap	D15	21.149 (full), 14.987 (half)	1.027
Scrap	D16	21.434 (full), 16.640 (half)	0.984
Metatarsal	D17	21.481 (full), 18.143 (half)	1.006
Metatarsal	D18	18.894 (half), 21.006 (full)	1
Metatarsal	D19	21.443 (full), 12.965 (half)	0.963
Metatarsal	D20	21.438 (full), 17.918 (half)	0.826
Mandible	D21	21.050 (full), 15.576 (half)	1.008

Cow			
Bone Type	**Sample Name**	**Diameter (mm)**	**Thickness (mm)**
Long Bone Shaft	C1	18.193 (half), 20.708 (full)	1.072
Distal Tibia Cranial	C2	21.257	0.989
Distal Tibia Cranial	C3	21.154	0.98
Distal Tibia Cranial	C4	21.343	0.983
Distal Tibia Cranial	C5	20.997	0.977
Long Bone	C6	21.497	0.958
Long Bone	C7	21.188	0.969
Tibia	C8	21.175	0.999
Tibia	C9	21.192	0.978
Long Bone	C10	21.304	0.985
Radius Shaft	C11	21.100	0.959
Tibia	C12	20.956	0.962
Tibia	C13	21.379 (full), 20.448 (half)	0.988
Long Bone	C14	19.84 (full), 15.333 (half)	0.997
Long Bone	C15	21.500	0.967
Long Bone	C16	21.258	0.979
Long Bone	C17	21.147	0.971
Long Bone	C18	21.256	0.996
Long Bone	C19	21.141	0.966
Long Bone	C20	23.294	0.99
Long Bone	C21	21.134	0.989
Long Bone	C22	21.121	0.985
Radius Shaft	C23	21.175 (full), 20.224 (half)	0.962

Bison			
Bone Type	**Sample Name**	**Diameter (mm)**	**Thickness (mm)**
Rib	B1	21.274	0.983
Rib	B2	21.148	0.984
Rib	B3	21.215 (full), 17.782 (half)	0.989
Rib	B4	17.423 (half), 21.402 (full)	0.991
Rib	B5	21.375	0.98
Rib	B6	21.198	1
Rib	B7	21.161	0.991
Rib	B8	21.230	0.974
Rib	B9	21.130	1
Rib	B10	21.046 (full), 17.171 (half)	1.021
Rib	B12	21.393	1.009
Rib	B13	21.448 (full), 18.246 (half)	0.981
Rib	B14	16.826 (half), 21.385 (full)	1
Rib	B15	21.141 (full), 16.563 (half)	0.988
Femur	B16	21.251	1.002
Femur	B17	21.186	1
Femur	B18	21.154	0.99
Rib	B19	20.537 (full), 19.363 (half)	0.978
Femur	B20	21.006	0.978
Femur	B21	20.922	0.955
Femur	B22	21.079	1.019
Femur	B23	21.166	0.982
Femur	B24	21.146	0.98
Femur	B25	21.201 (full), 16.785 (half)	0.979
Femur	B26	21.241	0.994
Femur	B27	21.233	0.987
Femur	B28	21.058	1.023

Elk			
Bone Type	**Sample Name**	**Diameter (mm)**	**Thickness (mm)**
Humerus	E1	21.2 (full), 20.419 (half)	0.963
Tibia	E2	21.120	1.01
Tibia	E3	20.223	0.968
Tibia	E4	18.590	0.97
Tibia	E5	21.274	1.229
Tibia	E6	21.266 (full), 19.883 (half)	1.019
Tibia	E7	21.187	0.984
Ilium	E8	20.612	0.983
Ilium	E9	241.372	0.956
Ilium	E10	21.133	0.966
Ilium	E11	21.220	0.996
Ilium	E12	21.060	0.982
Right Metarsal	E13	21.305	0.981
Right Metarsal	E14	21.438 (full), 19.948 (half)	0.959
Right Metarsal	E15	21.216	0.989
Long Bone	E16	21.040	1.038
Right Femur	E17	20.783 (full), 19.372 (half)	1.01
Right Radius	E18	15.967 (half), 21.411 (full)	0.985
Right Femur	E19	21.382 (full), 19.558 (half)	0.992
Left Distal Femur	E20	20.033 (half), 21.15 (full)	0.95
Right Radius	E21	21.251	0.973
Right Humerus	E22	20.980	1.005

<u>APPENDIX 3:</u> STEPS FOR DIELECTRIC MEASUREMENT USING KEYSIGHT E4991B IMPEDANCE ANALYZER WITH OPTION 002 DIELECTRICAL MATERIAL MEASUREMENT FIXTURE

Step I: Sample preparation for measurement

1. Applicable dielectric materials selected for measurement with the 16453A test fixture are solid with a smooth surface.
2. Materials must have a diameter that is ≥ 15 mm and a thickness that is at least 0.3 mm thick but no more than 3 mm thick.

Step II: Setting up Equipment

1. Connect the mouse, keyboard and test head to the E4991A. Do not remove the four feet on the bottom of the E4991A when connecting the test head.
2. Plug in the E4991A.
3. Press the standby switch in the lower-left part of the front panel from the popped up position to a depressed position to turn the power ON.
4. The E4991A starts a self-test automatically when the power is turned ON.

Step III: Selecting Measurement Mode

1. Click **Preset** on the **System** menu to set the initial state.
2. Click **Utility** on the **Utility** menu.
3. Click the **Material Option Menu** button.
4. Select **Permittivity** in the **Material Type** Box. The 16453A is automatically selected as the texture fixture to be used.

Step IV: Setting Measurement Conditions

1. Before starting the measurement, you must set the measurement parameters and sweep conditions. A summarized version of the parameter settings is in Table A2.1 below. To set the Measurement Parameters and Display Formats, click **Display** on the **Display** menu.
2. Click **3 Scalar** in the **Num of Trac**es box.
3. Click **Meas/Format** on the **Meas/Format** menu.
4. Specify Trace 1 as the active trace (* mark) and select **εr'** in the **Meas Parameter** box.
5. Select **Lin Y-Axis** in the **Format** box.
6. Specify Trace 2 as the active trace (* mark) and select **εr"** in the **Meas Parameter** box.
7. Select **Lin Y-Axis** in the **Format** box.
8. Specify Trace 3 as the active trace (* mark) and select **tanδ(ε)** from the **Meas Parameter** box.
9. Select **Lin Y-Axis** in the **Format** box.
10. To set the Measurement Points, Sweep Parameter, and Sweet Type, click **Sweet Setup** on the **Stimulus** menu.
11. In the **Number of Points** box, enter the number of measurement points. For example, 701 points were used for this research, so we typed in **[7] [0] [1] [Enter]** with the keyboard.
12. Select **Frequency** in the **Sweep Parameter** box.
13. Select **Log** in the **Sweep Type** box.
14. To set the Source Mode and Oscillator Level, click **Source** on the **Stimulus** menu.
15. Select **Voltage** in the **Osc Unit** box.

16. In the **Osc Level** box, enter the oscillator level. For this research, 100 mV was used so we typed in **[1] [0] [0] [m] [Enter]** with the keyboard.
17. To set the Sweep Range (Frequency), click **Start/Stop** on the **Stimulus** menu.
18. In the **Start** box, enter the start frequency. For example, we used 10 MHz so we typed in **[1] [0] [M] [Enter]** with the keyboard.
19. In the **Stop** box, enter the stop frequency. We used 1 GHz, so we typed in **[1] [G] [Enter]** with the keyboard.

Parameter setting		Settings used
Measurement parameters	Trace 1	εr'
	Trace 2	εr''
	Trace 3	tanδ
Display formats	Trace 1	Linear
	Trace 2	Linear
	Trace 3	Linear
Sweep parameter		Frequency
Sweep type		Log
Source mode		Voltage
Oscillator level		100 mV
Sweep range (Frequency)		10 MHz to 1 GHz

Table A2.1: Settings used for the instrument setup.

Step V: Connecting 16453A

1. Turn the 7-mm connector nut of the test head counterclockwise until the connector sleeve is fully retracted.
2. Tighten the two small screws of the fixture holder to secure the fixture holder to the test fixture body.
3. Connect the 7-mm connector of the test fixture to the 7-mm terminal of the test head.
4. Tighten the two large screws of the fixture holder to secure the test fixture to the test head.

Step VI: Entering Thickness of Load Standard

The load standard supplied with the 16453A test fixture is made of Teflon with a relative permittivity of 2.1. Enter the thickness of the Teflon load standard supplied with the 16453A test fixture. The thickness is printed on the surface of the case.

1. Click **Cal/Comp** on the **Stimulus** menu.
2. Click the **Cal Kit Menu** button.
3. In the **Thickness** box, enter the thickness of the load standard. For example, if the load standard is 0.75 mm in thickness, type **[0] [.] [7] [5] [m] [Enter]** with the keyboard.

Step VII: Calibration

Calibration is performed by using the material under testing connection plane of the 16453A test fixture as the calibration reference plane. By performing calibration on the material under testing connection plane, you can eliminate errors due to the test fixture's residuals and electric length. Therefore, unlike impedance measurement, electric

length or fixture compensation is not required.

1. Click **Cal/Comp** on the **Stimulus** menu.
2. In the **Fixture Type** box, confirm that the test fixture is set to 16453. Otherwise, set the measurement mode to dielectric measurement mode.
3. Click the **Cal Menu** button.
4. In the **Cal Type** box, select the desired type of measurement points for the calibration data. For example, for this research we used 701 points.
5. Set the material under testing connection plane of the test fixture to the SHORT state by releasing the latch button so that the upper electrode makes contact with the lower electrode of the 16453A test fixture (see figure A2.1 for reference).
6. Click the **Meas Short** button to start measuring SHORT calibration data. During calibration data measurement, the message "Wait-Measuring Cal Standard" appears at the left end of the status bar at the bottom of the screen. Upon completion of the SHORT calibration measurement, a check mark appears on the left side of the **Meas Short** button.

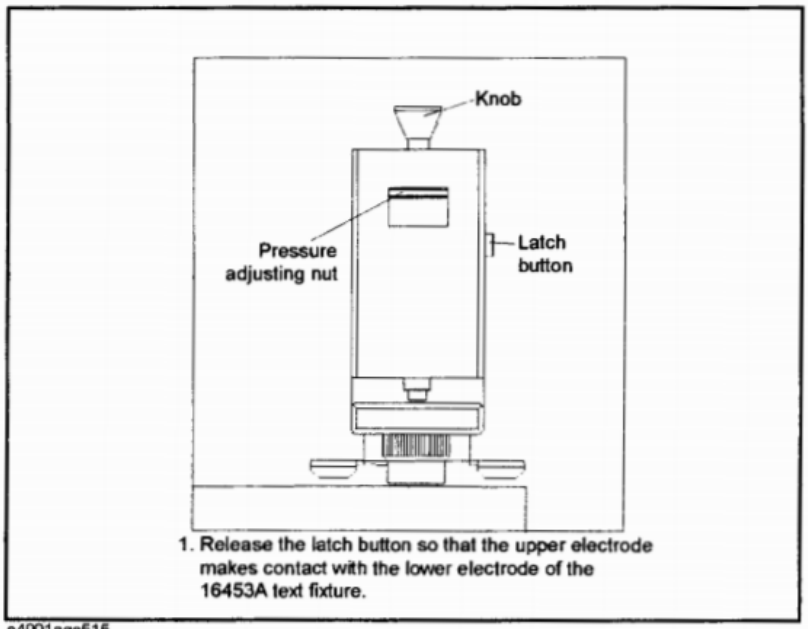

Figure A2.2: Calibration steps in the SHORT state.

7. Set the material under testing connection plane of the test fixture to the OPEN state by pulling up the knob and pressing the latch button while holding up the knob (see Figure A2.3 for reference). When the knob is released remains in the up position.
8. Click the **Meas Open** button to start measuring OPEN calibration data. During calibration data measurement, the message "Wait-Measuring Cal Standard" appears at the left end of the status bar at the bottom of the screen. Upon completion of the OPEN calibration data measurement, a check mark appears on the left side of the **Meas Open** button.

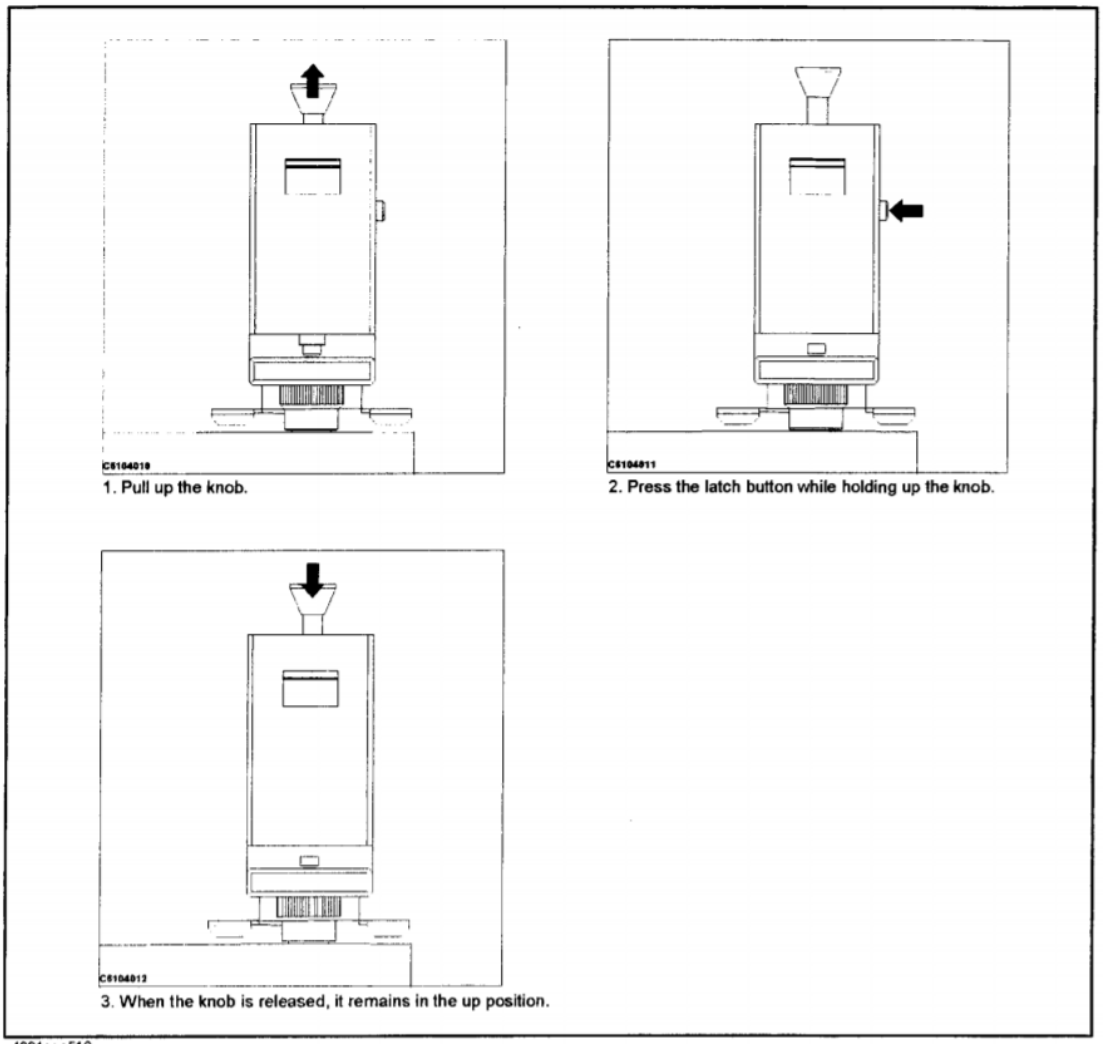

Figure A2.3: Calibration steps in the OPEN state.

9. Connect the load standard supplied with the 16453A test fixture to the test fixture by inserting it (using the provided tweezers to avoid contamination from your hands) between the electrodes of the test fixture (see Figure A2.4 for reference). When connecting a load standard or a material under test to the test fixture, make sure that it only comes into contact with the test fixture's electrodes. Also, be careful not to give the upper electrode horizontal pressure by moving the load standard or the material under test while it is in position between the electrodes.

10. Click the **Meas Load** button to start measuring LOAD calibration data. During calibration data measurement, the message “Wait-Measuring Cal Standard” appears at the left end of the status bar at the bottom of the screen. Upon completion of the LOAD calibration data measurement, a check mark appears on the left side of the **Meas Load** button.

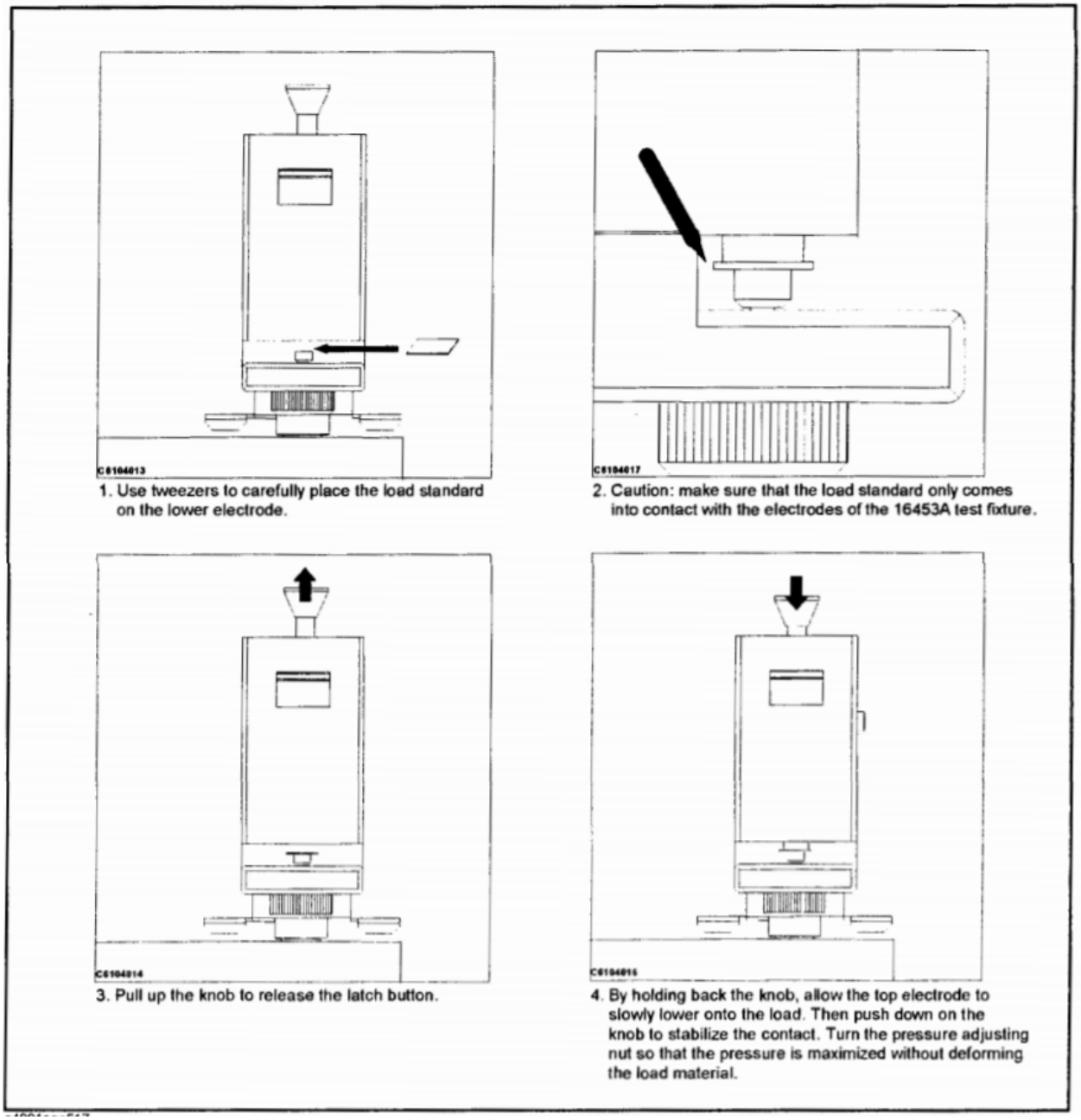

Figure A2.4: Calibration steps in the LOAD state.

11. Click the **Done** button to instruct the E4991A to calculate the calibration coefficient from the measured calibration data and save it to the internal memory.
12. Depending on the measurement points of the calibration data specified in the **Cal Type** box, the display below the **Cal Menu** button and on the status bar at the bottom of the screen will change as shown in the following Table A2.2.

Cal Type box	Display below the **Cal Menu** button		Status bar on the bottom of the screen	
	Before Calibration	After calibration	Before calibration	After calibration
User Freq&Pwr	[Uncal]	[User]	Uncal	Cal User
Fixed Freq&Pwr	[Uncal]	[Fix]	Uncal	Cal Fix
FixedFreq,UserPwr	[Uncal]	[FixR]	Uncal	Cal FixR

Table A2.2: Status display when calibration is completed.

Step VIII: Entering Thickness of Material Under Testing

You must enter the thickness of the material being tested before you can perform the measurement. For this research, digital calipers were used to measure the thickness.

1. Click **Utility** on the **Utility** menu.
2. Click the **Material Option Menu** button.

3. In the **Thickness** box, enter the thickness of the material under test. For example, if the material is 1 mm in thickness, type **[1] [m] [Enter]** with the keyboard.

Step IX: Connecting the Material Under Testing

1. As with the load standard, connect the material being tested to the 16453A test fixture by inserting it between the test fixture's upper and lower electrodes using the tweezers provided. Do not touch the sample with your hands to avoid contamination. When connecting a material under test to the test fixture, make sure that it only comes into contact with the test fixture's electrodes. Also, be careful not to give the upper electrode horizontal pressure by moving the load standard or the material under test while it is in position between the electrodes.
2. If the pressure from the upper and lower electrodes is too weak, this may create a gap between the material under testing and the electrodes and thus cause measurement errors. It is recommended that the pressure be maximized to the extent that it does not deform the material under testing. For best repeatability when measuring both a load standard and a material under testing, connect them to them to the test fixture with the same pressure.

APPENDIX 4: RELATIVE PERMITTIVITY, LOSS FACTOR, AND LOSS TANGENT MEASUREMENTS

The following excel spreadsheets contain the results of the relative permittivity, loss factor, and loss tangent over the frequency sweep of 10 MHz-1000 MHz. The bottom tabs list the sample name, and the three individual measurements are listed.

The results for the bison bone samples can be downloaded here.

The results for the cow bone samples can be downloaded here.

The results for the deer bone samples can be downloaded here.

The results for the elk bone samples can be downloaded here.

The results for the mammoth bone sample can be downloaded here.

APPENDIX 5: POROSITY, BULK DENSITY, VOLUMETRIC WATER CONTENT, AND WATER SATURATION MEASUREMENTS

Sample ID	Porosity	Bulk Density (g/cc)	Water Saturation	Volumetric Water Content
D1	21.7%	1.94	76.4%	16.6%
D2	27.6%	1.92	59.1%	16.3%
D3	30.5%	2.03	56.8%	17.3%
D4	20.1%	1.62	74.5%	15.0%
D5	14.6%	1.73	94.6%	13.9%
D6	16.1%	1.75	87.0%	14.0%
D7	17.8%	2.00	87.9%	15.6%
D9	25.1%	2.01	72.7%	18.2%
D10	20.3%	1.72	75.0%	15.2%
D11	25.9%	2.04	67.2%	17.4%
D12	43.2%	1.62	28.3%	12.2%
D13	29.7%	2.31	64.1%	19.0%
D14	28.9%	2.04	54.9%	15.9%
D15	23.6%	1.79	63.9%	15.1%
D16	21.4%	2.01	77.9%	16.7%
D17	27.2%	2.19	64.9%	17.6%
D18	21.0%	2.12	81.1%	17.1%
D19	27.1%	1.97	60.2%	16.3%
D20	25.9%	2.27	72.6%	18.8%
D21	27.1%	1.97	67.2%	18.2%

Table A5.1: Porosity, Bulk Density, Saturation, and Volumetric Water Content for the deer samples.

Sample ID	Porosity	Bulk Density (g/cc)	Water Saturation	Volumetric Water Content
C1	25.4%	2.21	66.1%	16.8%
C2	19.5%	2.01	75.5%	14.7%
C3	21.0%	1.98	76.5%	16.0%
C4	16.6%	1.85	90.5%	15.0%
C5	21.5%	2.07	72.3%	15.6%
C6	24.7%	1.97	55.5%	13.7%
C7	26.7%	1.95	53.6%	14.3%
C8	21.2%	2.11	74.7%	15.8%
C9	23.3%	2.05	70.6%	16.4%
C10	22.8%	2.39	75.6%	17.3%
C11	22.2%	2.08	64.4%	14.3%
C12	21.5%	2.13	71.1%	15.3%
C13	20.8%	2.02	69.5%	14.5%
C14	20.7%	2.04	77.4%	16.0%
C15	24.0%	2.00	67.2%	16.1%
C16	23.0%	2.06	73.2%	16.8%
C17	23.7%	2.08	69.9%	16.6%
C18	22.0%	2.07	72.2%	15.9%
C19	25.1%	2.03	63.0%	15.8%
C20	21.6%	2.08	70.1%	15.1%
C21	20.3%	2.12	73.9%	15.0%
C22	21.0%	2.13	72.7%	15.3%
C23	21.8%	2.07	69.4%	15.1%

Table A5.2: Porosity, Bulk Density, Saturation, and Volumetric Water Content for the cow samples.

Sample ID	Porosity	Bulk Density (g/cc)	Water Saturation	Volumetric Water Content
B1	26.7%	1.83	59.1%	15.8%
B2	26.9%	1.77	54.9%	14.8%
B3	17.2%	1.45	70.9%	12.2%
B4	19.9%	1.66	68.4%	13.6%
B5	26.2%	1.68	53.0%	13.9%
B6	24.1%	1.66	56.4%	13.6%
B7	22.3%	1.66	61.5%	13.7%
B8	18.3%	1.26	57.3%	10.5%
B9	20.1%	1.60	60.1%	12.1%
B10	19.1%	1.86	75.5%	14.5%
B12	24.3%	2.23	70.3%	17.1%
B13	22.4%	2.29	85.5%	19.2%
B14	21.0%	2.34	92.2%	19.4%
B15	22.9%	2.30	87.8%	20.1%
B16	18.6%	2.43	93.6%	17.4%
B17	30.8%	2.10	47.4%	14.6%
B18	22.8%	2.38	73.2%	16.7%
B19	25.7%	2.21	73.5%	18.9%
B20	23.5%	2.40	70.8%	16.6%
B21	24.9%	2.41	76.8%	19.2%
B22	41.4%	2.38	96.0%	39.8%
B23	19.1%	2.51	92.7%	17.7%
B24	21.9%	2.27	79.3%	17.3%
B25	21.1%	2.35	86.2%	18.1%
B26	21.5%	2.39	89.0%	19.1%
B27	21.7%	2.40	81.4%	17.7%
B28	21.4%	2.38	85.3%	18.3%

Table A5.3: Porosity, Bulk Density, Saturation, and Volumetric Water Content for the bison samples.

Sample ID	Porosity	Bulk Density (g/cc)	Water Saturation	Volumetric Water Content
E1	20.0%	1.97	72.8%	14.6%
E2	20.2%	2.18	77.3%	15.7%
E3	18.2%	1.89	76.7%	14.0%
E4	23.7%	2.55	77.1%	18.3%
E5	25.8%	2.12	65.7%	16.9%
E6	28.3%	2.35	66.1%	18.7%
E7	28.8%	2.13	62.1%	17.9%
E8	23.8%	1.95	61.6%	14.7%
E9	22.1%	1.93	66.6%	14.7%
E10	27.3%	2.30	65.4%	17.9%
E11	28.4%	2.33	61.8%	17.5%
E12	27.5%	2.38	64.0%	17.6%
E13	23.1%	2.44	75.5%	17.5%
E14	28.6%	2.37	61.3%	17.5%
E15	27.5%	2.33	65.4%	18.0%
E16	24.9%	2.42	85.2%	21.2%
E17	30.6%	2.48	66.3%	20.3%
E18	27.8%	2.63	79.1%	22.0%
E19	23.6%	2.22	82.5%	19.5%
E20	27.9%	1.96	61.5%	17.2%
E21	21.0%	2.07	74.4%	15.6%
E22	21.9%	2.01	79.3%	17.3%

Table A5.4: Porosity, Bulk Density, Saturation, and Volumetric Water Content for the elk samples.

APPENDIX 6: SAMPLE MATLAB CODE FOR SOLVING HANAI-BRUGGEMAN EQUATION

```
close all; clear all; clc;   %empty out workspace

load cowporosity;
load cowsaturation;

Ea = 1;     %permittivity of air
Ew = 79;        %permittivity of water
syms Epore; %create symbolic variable for Epore
m = 2;      %cementation index, set to either 1.5 or 2
sw=saturation;
g = 9.43;          %estimated permittivity of the bone mineral grain at certain frequency
phi=porosity;
syms Es;        %create symbolic variable for permittivity of overall sample
z=zeros(2,length(sw));  %preallocate matrix
z2=zeros(2,length(phi));     %preallocate a second matrix

for kk=1:length(sw)
tmp=solve((Epore-Ew*(sw(kk).^(m))*(((1-(Ea/Ew))/(1-(Ea/Epore))).^(m))),Epore);  %solve for
Epore
z(:,kk)=double(tmp);    %convert symbolic variable to numbers
end

return

Epreal = z(2,:);%permittivity of pore space calculated in step 1

for kk=1:length(phi)%loop in the porosity values in the equation
tmp2 = solve(Es-(Epreal(kk)*(phi(kk).^m)*(((1-(g/Epreal(kk)))/(1-(g/Es))).^m)),Es);        %solve
for Es
z2(:,kk) = real(double(tmp2)); %convert symbolic variable to numbers
end
FinalEs=real(z2(2,:));
FinalEs=transpose(FinalEs);
```